EVALUATION AND IMPROVEMENT OF OPTICAL REMOTE SENSING METHODS IN MONITORING PARTICULATE MATTER EMISSIONS AND PLUME OPACITY

BY

WANGKI YUEN

DISSERTATION

Submitted in partial fulfillment of the requirements
for the degree of Doctor of Philosophy in Environmental Engineering in Civil Engineering
in the Graduate College of the
University of Illinois at Urbana-Champaign, 2018

Urbana, Illinois

Doctoral Committee:

Professor Mark J. Rood, Chair and Director of Dissertation Research
Doctor Sotiria Koloutsou-Vakakis, Co-Director of Dissertation Research
Professor Tami C. Bond
Professor Yuanhui Zhang
Assistant Professor Ke Du, University of Calgary

ABSTRACT

Atmospheric particulate matter (PM) affects human health, reduces visibility, and impacts climate. PM also causes plume opacity, which is defined as percentage of light that is attenuated by a plume. This research focuses on two optical methods that have been developed and implemented previously to measure PM mass emission factor (EF) and plume opacity. My contributions to this research are: 1) evaluating and improving the previous approaches used in these two methods, and 2) estimating their associated uncertainties to quantify PM EF and plume opacity values.

In the first part of the research, fugitive PM EFs that come from unconfined flow streams are measured by the *hybrid-optical remote sensing (hybrid-ORS) method*. Fugitive PM EFs pose a challenge for measurements because they are aloft, heterogeneous, have short lifetimes, and can exist within large spatial scales. These challenges can be addressed by the developed hybrid-ORS method. The hybrid-ORS method that I used involves the use of micro-pulse light detection and ranging (lidar; MPL) that measures range-resolved extinction coefficients. Co-located point PM mass concentrations and extinction coefficients are measured to determine PM mass concentration from light extinction measurements provided by the MPL. Fugitive PM EFs are then obtained by integrating PM mass concentrations across the plume's cross-section with wind data and duration of events. Two field campaigns were completed to measure fugitive PM emissions from mobile vehicles on unpaved roads, as well as open burning or detonation of energetic materials. The fugitive PM EFs from these two sources were also measured by at least one independent and concurrent method for comparison. The results show that PM EFs measured by hybrid-ORS method and other concurrent methods are not significantly different, while hybrid-ORS method offers the advantage of knowing the spatial and temporal distributions of PM mass concentration in a fugitive PM plume. In addition, two lidar equation inversion

methods, namely near-end and far-end methods, were compared with respect to its PM EF and its uncertainty. The results show that the far-end method is preferable because it introduces less uncertainty, and the method is mathematically stable.

In the second part of the research, plume opacity is measured using digital optical method (DOM) that was previously developed by Du (2007). This method is an improvement over the traditional human observer method in determining plume opacity. DOM was initially developed using compact digital cameras, but the method was extended with this research to smartphone cameras and a camcorder. In DOM, the response curves, which relate exposure to pixel value (PV), are determined for compact cameras, smartphone cameras, and a camcorder. Then, relative exposures of select regions within a plume picture are used to calculate plume opacity using DOM software. There are two DOM models that were previously developed by Du (2007), namely: 1) the contrast model that requires a plume passing in front of and near one of two co-located contrasting backgrounds; and 2) the transmission model that requires a plume passing in front of and near one background, and a diffusive scattering parameter (K) that characterizes the optical property of the plume relative to its background. A field campaign was performed to use compact cameras, smartphone cameras, and a camcorder to measure the opacity of plumes emitted from a smokestack using DOM. The smokestack included a transmissometer inside, which provided independent opacity measurements used as a standard for comparison with the devices using DOM. In this research, a new method was developed for calibration of cameras and a camcorder that uses exposure value (EV) compensation. The results for the compact and smartphone cameras show that: 1) the resulting opacity values are not significantly different from those determined by two previous calibration methods; 2) the color contrast between two backgrounds is the most important variable affecting the uncertainties of opacity measured by

the two DOM models; and 3) empirically determined K values for select background and plume color combinations show that K value depends on wavelength of background color. The results for the camcorder show that: 1) the camcorder can accurately measure opacity values in real-time (1 Hz); 2) increasing color contrast between two backgrounds using, DOM contrast model, decreases opacity measurement errors and uncertainties; and 3) background choice is more important than camcorder calibration and number of sampled pixels in determining the opacity measurement uncertainty.

This research is novel and significant by providing for improvements and uncertainty analyses of two remote sensing methods for PM. Evaluations of the hybrid-ORS method and DOM are done for method improvements (e.g., increase flexibility and understanding of the applicability of the hybrid-ORS method and the transmission model; demonstrate that DOM can be applied to smartphone cameras and a camcorder aside from compact cameras). The uncertainty analyses identify the major sources of measurement uncertainties and quantify the overall uncertainty for future applications of these methods.

ACKNOWLEDGEMENTS

First, I would like to thank my two thesis advisors: Mark J. Rood and Sotiria Koloutsou-Vakakis. They not only provide comments on my research and my written and oral communication skills, but also show me various opportunities and personal network for the professional and academic world in air quality engineering.

Next, I would like to thank other members of my dissertation committee: Ke Du, Tami C. Bond, and Yuanhui Zhang. They all provide valuable technical comments of my preliminary research proposal and demonstrate me various scientific aspects in air quality topics. Specifically, Ke Du, who previously worked on this ORS project, assists me a lot in technical instrument troubleshooting. His previous dissertation also inspires me some topics that I explore in this research.

This research requires days to week-long field campaigns to collect data for analysis. I would like to thank a group of people that make these field campaigns successful. In the field campaigns concerning with fugitive PM emissions, Ram A. Hashmonay provided me professional and technical knowledge in optical remote sensing in general. He also provided me data for my further analysis. Byung J. Kim and Michael R. Kemme coordinated such field campaigns. Without them, we would not be able to collect fugitive PM plume data from various sources. In the field campaigns concerning with opacity measurements by cameras, Hyun-Keun Son cooperate with me extensively in the preparation and measurement for the field campaign. He also encouraged me during my Ph.D. Program. Kevin Mattison and Bill Franek allowed us to take pictures and videos in their visible emission evaluation courses, so that I could collect data for the analysis of this research.

I would also like to thank Ravi Varma, who built and troubleshot a laser transmissometer that was used in one field campaign that measures fugitive PM emission. My communication with him gave me hand-on experience in laboratory work.

Several undergraduate students had helped me to perform data analysis, and I would like to thank their efforts in learning something that they have not done before. They include Yichao Gu, Yalin Mao, Peter Kozak for the opacity work, and Qi Ma for the fugitive PM emission work.

I would also like to thank several groups. The first is Air and Waste Management Association (A&WMA). Their annual conferences opened up my view in air quality engineering in the professional world and provide me social network. They also provide us funding for attending these conferences, and give awards for outstanding conference proceedings and scholarships, which I had benefited from. Similarly, annual Fall Meetings by American Geophysical Union provide me network in the scientific community. Funding from the Department of Defense (DoD) allowed us to perform field campaigns that measure fugitive PM emission from various sources. Last, but not least, my Department of Civil and Environmental Engineering in the University of Illinois provides human and financial resources that make my Ph.D. program successful.

Finally, I would like to thank of my research group for the friendship. I would especially thank David Johnsen in my group, who helped me with the preparation of a field campaign. I would also like to thank my roommates and friends outside of my research group that keep me physically, mentally, and emotionally healthy. I should not forget to mention my family who supports me my path to this engineering degree completion. Although they are unfamiliar with graduate school and engineering, their consistent support encourages me to move forward to complete this Ph.D. degree.

TABLE OF CONTENTS

LIST OF IMPORTANT ACRONYMS

AOE = average opacity error
APS = aerodynamic particle sizer
BAM = beta attenuation monitor
DOCS = digital opacity compliance system
DOM = digital optical method
EF = emission factor
EV = exposure value
FEM = federal equivalent method
FRM = federal reference method
GPS = global positioning system
IEPA = Illinois Environmental Protection Agency
IOE = individual opacity error
LCD = liquid-crystal display
lidar = light detection and ranging
LPM = liters per minute
MEE = mass extinction efficiency
MOUDI = micro-orifice uniform deposit impactor
MPD = mean percentage difference
MPL = micropulse lidar
MSE = mass scattering efficiency
NEI = national emission inventory
NOAA = National Oceanic and Atmospheric Administration
NRB = normalized relative backscatter (corrected MPL signal)
OB = open burning
OD = open detonation
τ = optical depth
OP-FTIR = open-path Fourier transform infrared spectroscopy
OP-LT = open-path laser transmissometer
OPS = optical particle sizer
ORS = optical remote sensing
PAX = photoacoustic extinctiometer
PM = particulate matter
PM_{10} = PM with diameter less than or equal to 10 µm
$PM_{2.5}$ = PM with diameter less than or equal to 2.5 µm
PSAP = particle soot absorption photometer
PSD = particle size distribution
PV = pixel value
RGB = red, green, blue
SEM-EDX = scanning electron microscope, coupled with energy dispersive X-ray
SMPS = scanning mobility particle sizer
TEOM = tapered element oscillating microbalance
TNT = trinitrotoluene
TRAKER = testing re-entrained aerosol kinetic emissions from roads
TSP = total suspended particles
USEPA = United States Environmental Protection Agency

PART I: INTRODUCTION

CHAPTER 1: INTRODUCTION

1.1. Particulate Matter (PM) in the Atmosphere

Motivation for Studying PM

There has been extensive literature about the health effects of PM. PM has been linked to cardiovascular and pulmonary diseases (Dockery and Pope, 1994; Pope and Dockery, 2006). The ability for PM to scatter and absorb light reduces visibility (Malm, 1999). The same phenomena also affect the Earth's climate. The effect of scattering reduces the amount of solar radiation to the Earth's surface, while the effect of absorption retains the solar energy in the atmosphere. PM can also act as cloud condensation nuclei, which increases the likelihood of forming clouds or changing the properties of clouds that may cause net decrease in terrestrial solar radiation and modify precipitation patterns (Anenberg et al., 2012; Khalizov et al., 2009; Storelvmo et al., 2011). Thus, it is important to estimate the PM emissions so that plans can be made to reduce the harmful effects of PM.

Classifications of PM

PM can either be emitted directly as primary pollutant to the atmosphere (e.g., black carbon and mineral dust), or form as secondary pollutant through chemical reaction (e.g., reaction of ammonia with sulfuric and nitric acid, resulting in ammonium sulfate and ammonium nitrate, respectively). The sources can be natural (e.g., forest fire and wind-blown dust) or anthropogenic (e.g., industry and vehicles). PM is also often classified by: 1) chemical composition, and 2) size. Chemical components of PM is a complex mixture of materials including water, acids (e.g., sulfuric and nitric), bases (e.g., NH_3), salts (e.g., NaCl), organic carbon, elemental carbon, metals, and mineral dust. Depending on source and chemical composition, particles have different properties such as size, shape and refractive index (Seinfeld

and Pandis, 2016). The USEPA includes two size ranges in the criteria air pollutants, namely PM with diameter less than or equal to 10 μm (PM_{10}) and 2.5 μm ($PM_{2.5}$), for both of which there are National Ambient Air Quality Standards (NAAQS), according to Clean Air Act requirements. Such size differentiation is due to their difference in sources, formation and removal mechanisms, atmospheric residence time, chemical composition, and health effects (USEPA, 2004, 2016a).

Fugitive PM

Fugitive PM is defined as PM emitted from an unconfined flow stream (USEPA, 2016b; Watson and Chow, 2000). It comes from activities that disturb soil including wind erosion, agricultural activities, mining activities, vehicle transportation, and open burning (OB) and open detonation (OD) of energetic materials such as propellants and explosives. My research dealt with the last two types of fugitive PM emissions. Fugitive PM emissions from vehicle transportation are measured because from the national emission inventory (NEI) in 2011, such emissions from all paved and unpaved roads accounted for 45% of the PM_{10} and 18% of the $PM_{2.5}$ total primary emissions (USEPA, 2015). Fugitive PM emissions from OB and OD of energetic materials are measured because amount of energetic materials disposed by OB/OD activities is limited by the Resource Conservation and Recovery Act (RCRA) permits, partly based on the PM emissions of such activities (Mitchell and Suggs, 1998).

Yet, these estimates are based on PM mass emission factors (EFs) that are highly uncertain, such as EF generated from vehicle travel described in the AP-42 database (USEPA, 2016b). The uncertainty is large because fugitive PM plumes are aloft, heterogeneous, have short lifetimes (in the order of minutes), and can exist within large spatial scales (in the order of tens to hundreds of meters in vertical and horizontal directions). Thus, fugitive PM emissions are difficult to quantify. There remains a need for improving the accuracy of fugitive PM EFs (Du et al., 2011a).

Physical and Optical Properties of Dust

Dust is a sub-category of PM that comes from suspension of soil particles (Nousiainen, 2009). It comes from soil that is a mixture of minerals. The major mineral species for the clay fraction of soil (diameter < 2 μm) are illite, kaolinite, smectite, calcite, and quartz, and the major mineral species for the silt fraction of soil (diameter between 2 to 63 μm) are quartz, feldspar, calcite, hematite, and gypsum (Claquin et al., 1999). The difference of major mineral species for the silt- and clay-sized particles indicates differences in refractive indices for the two size fractions.

Dust physical properties include particle density, size distribution, and shape. Densities of each mineral are shown in Table 1.1 (Ralph and Chau, 1993). Most minerals have densities between 2 and 3 g/cm^3, with the exception of hematite (5.26 g/cm^3).

Table 1.1. Densities of minerals.

Mineral	**Density (g/cm^3)**
Illite	2.61
Kaolinite	2.63
Quartz	2.66
Calcite	2.71
Gypsum	2.31
Hematite	5.26

Particle size distribution (PSD) of mineral dust follows a log-normal distribution. The geometric mean diameter of the PSD by mass is typically between 1 and 4 μm (Tegen and Lacis, 1996). From previous field campaigns in Yuma, AZ (2007) (Du et al., 2011a), the geometric mean diameter by number ranged from 0.4 to 0.7 μm, with geometric standard deviation from 1.8 to 1.9 (unpublished data). Assuming a lognormal PSD, the geometric mean diameter by mass is calculated to be between 1.1 and 2.4 μm, using a method described in Seinfeld and Pandis (2016). This calculated range is within the typical range stated above.

Dust particles are usually not spherical. They occur in various shapes, such as thin flakes, angular crystals, and can form aggregates (Nousiainen, 2009). The non-spherical nature of dust particles poses difficulties in modeling light extinction because optical properties are sensitive to particle shapes (Mishchenko, 2009).

Dust refractive index affects the optical properties, which, as described later, include opacity, transmittance, extinction, scattering, and absorption coefficients, scattering phase function, and mass extinction efficiency. Although dust consists of a mixture of minerals, most minerals have similar refractive indices. At visible wavelengths (λ = 380–760 nm), illite, kaolinite, quartz, calcite, and gypsum have real part of refractive indices (n) between 1.4 and 1.6. Illite and kaolinite have imaginary part of refractive indices (k) less than 0.001. Hematite is an exception, where n is between 2.6 and 3.1 at visible wavelengths, and k is 0.05 to 0.1 and -0.3 at wavelengths of 527 and 590 nm, respectively (Table 1.2) (Kandler et al., 2007; Sokolik and Toon, 1999).

Table 1.2. Refractive indices of major minerals in dust at wavelength (λ) of 527 nm, unless stated otherwise.

Mineral	**Real part of refractive index (n)**		**Imaginary part of refractive index (k)**	
	(Sokolik and Toon, 1999)	**(Kandler et al., 2007)**	**(Sokolik and Toon, 1999)**	**(Kandler et al., 2007)**
Illite	1.4	1.57	0.001	N/A
Kaolinite	1.5	N/A	$3x10^{-5}$	N/A
Quartz	1.5	1.55	N/A	N/A
Calcite	1.5	1.60	N/A	N/A
Gypsum	1.5	N/A	N/A	N/A
Hematite	2.6 to 3.0	3.05	0.05 to 0.1	-0.3 (λ = 590 nm)

N/A= not available

1.2. Overview of Radiative Transfer

Radiative Transfer Equation

When visible light is intercepted by PM or gas molecules, the radiance of light can be: 1) reduced by scattering, where light in the direction of interest is scattered to a new direction, 2) reduced by absorption, 3) increased by emission, and 4) increased by diffuse scattering, where light from any directions is scattered to the direction of interest. The energy balance on PM or gas molecules intercepted by visible light is described by the radiative transfer equation (Eq. (1.1)) (Petty, 2006):

$$\frac{dI}{dx} = -\frac{dI_{absorption}}{dx} - \frac{dI_{scattering}}{dx} + \frac{dI_{emission}}{dx} + \frac{dI_{diffuse\ scattering}}{dx} \tag{1.1}$$

or in its extended form, for a specific wavelength in a direction of interest:

$$\frac{dI(\mathbf{\Omega})}{dx} = -\beta_a I(\mathbf{\Omega}) - \beta_s I(\mathbf{\Omega}) + \beta_a B(T) + \frac{\beta_s}{4\pi}\int_{4\pi} I(\mathbf{\Omega'}) p(\mathbf{\Omega'}, \mathbf{\Omega})\, d\omega \tag{1.2}$$

where:

I = radiance (W m^{-2} sr^{-1}).

x = distance (m).

β_a = absorption coefficient (m^{-1}).

β_s = scattering coefficient (m^{-1}).

B(T) = Planck's function at blackbody temperature T.

Ω = direction of interest.

Ω' = other directions.

ω = solid angle (sr).

p (**Ω'**, **Ω**) = scattering phase function between direction of interest and another direction.

Emission can be spontaneous, where temperature of the PM or gas molecules determine the total and spectral distribution of emitted radiance. Emission can also be stimulated, where PM or gas molecules are excited through chemical reactions, light, or other energy sources to emit radiation. However, spontaneous visible light emission of PM and gas molecules is negligible at room temperature according to the Planck's function, B(T). Assuming negligible stimulated light emission, the emission term can be ignored for visible light in the radiative transfer equation.

Although diffuse scattering is part of the scattering, the diffuse scattering term is discussed separately because it comes from PM scattering of background light source, which occurs from sunlight during daytime. The diffuse scattering term can be ignored if there is no background light (e.g., in nighttime), or if background light is measured and subtracted from the raw measurements.

Opacity and Transmittance

When the diffuse scattering and emission terms of the radiative transfer equation are ignored, the equation becomes the Beer-Lambert Law (Petty, 2006):

$$\frac{dI(\mathbf{\Omega})}{dx} = -\beta_e I(\mathbf{\Omega}) \tag{1.3}$$

where:

β_e = extinction coefficient.

Solving this differential equation, we have:

$$T = \frac{I}{I_0} = \exp(-\beta_e x) \tag{1.4}$$

where:

I_0 = radiance of light before extinction by PM or gases.

I = radiance of light after extinction by PM or gases.

If the extinction is not uniform over the distance, x, the Beer-Lambert Law can be written as the following:

$$T = \frac{I}{I_0} = \exp(-\int_0^x \beta_e(x')dx') \quad (1.5)$$

On the left side of Eq. (1.5), the term I/I_0 is called transmittance (T), which is defined as fraction of light that passes through a medium for a distance, x. Opacity (O) is defined as fraction of light that is attenuated by a medium, i.e.:

$$O = 1 - T = 1 - \exp(-\beta_e x) \quad (1.6)$$

Extinction Coefficients

On the right side of Eq. (1.5), β_e represents the volume extinction coefficient (unit: m^{-1}), which is the sum of volume scattering and absorption coefficients (β_s and β_a, unit: m^{-1}). For simplicity, "extinction/ scattering/ absorption coefficients" will mean "volume extinction/ scattering/ absorption coefficients" for the rest of this dissertation. The magnitudes of β_s and β_a depend on particle physical properties, refractive index, and number concentration. They can be calculated by the following equation:

$$\beta_x = \int Q_x(D_p, \lambda, m) A(D_p) N'(D_p) dD_p \quad (1.7)$$

where:

x can mean extinction (e), scattering (s), or absorption (a).

$Q_x(D_p, \lambda, m)$ = unitless extinction/ scattering/ absorption efficiency, which depends on particle diameter (D_p), wavelength of light (λ), and particle refractive index (m).

$A(D_p)$ = particle cross-sectional area at the direction of the beam.

$N'(D_p)$ = number PSD per unit particle diameter range (dD_p).

If sphericity of all the particles is assumed, there exists an analytical solution from Mie-Lorentz Theory (Bohren and Huffman, 1983; Petty, 2006) that predicts Q for extinction, scattering, and absorption as a function of particle refractive index, particle size, and wavelength of light. However, the shape of dust is not spherical and therefore uncertainties arise when using Mie-Lorentz Theory to predict Q and then extinction/ scattering/ absorption coefficients.

Extinction coefficient for air is in the order of 10^{-5} m^{-1}. When PM concentration is ambient (i.e., in the order of 10 $\mu g/m^3$), extinction coefficient for PM is comparable to that for air. However, when considering PM concentration of a plume from a fugitive or point source, extinction coefficient of PM is much larger than air. For example, extinction coefficient of a fugitive PM plume generated by open detonation can reach 0.03 m^{-1} when the PM mass concentration reaches 68 mg/m^3 (Section 3.4). Therefore, the effect of light extinction by air will be ignored in this research.

Scattering Phase Function and Backscatter Coefficients

When the electromagnetic wave is scattered by PM or gas molecules, there is a distribution of the relative amount of radiances scattered to each angle. Such distribution is described by the scattering phase function ($p(\mathbf{\Omega'}, \mathbf{\Omega})$). For spherical particles, the scattering phase function can be derived from Mie-Lorentz Theory (Bohren and Huffman, 1983; Petty, 2006).

Backscatter coefficient ($\beta_{s,\pi}$) quantifies the strength of backscattering, which is the light scattering at 180°. $\beta_{s,\pi}$ can be calculated with Eq. (1.8):

$$\beta_{s\pi} = \int Q_s(D_p, \lambda, m)p(\Theta = \pi, D_p, \lambda, m)A(D_p)N'(D_p)dD_p \qquad (1.8)$$

Mass Extinction Efficiency (MEE)

MEE (unit: m^2/g) is defined as the ratio of extinction coefficient (m^{-1}) to PM mass concentration (g/m^3). This quantity is also described as mass extinction cross-section (Fuller et al., 1999; Khalizov et al., 2009) or extinction-to-mass ratio (Upadhyay et al., 2008). MEE for particles with diameters ranging from D_{p1} to D_{p2} is described by Eq. (1.9):

$$MEE_{D_{p1}-D_{p2}} = \frac{\beta_e}{C_m} \tag{1.9}$$

where:

C_m = total mass concentration of particles with diameters ranging from D_{p1} to D_{p2}, and particle density ρ_p (Eq. (1.10)).

$$C_m = \rho_p \int_{D_{p1}}^{D_{p2}} \frac{\pi}{6} D_p{}^3 N'(D_p) dD_p \tag{1.10}$$

MEE values depend on the particle properties, and may vary due to location and even seasons. At measurement wavelengths between 530 and 565 nm, PM_{10} MEE values range from 0.5 m^2/g in Texas (Upadhyay et al., 2008) to 5.9 m^2/g in California, assuming no particle absorption (Chow et al., 2006). The study by Upadhyay et al., 2008 also identified that PM_{10} MEE values are > 2.0 m^2/g from October to December 2005, while PM_{10} MEE values are close to 0.5 m^2/g from February to July 2006. MEE values for fugitive dust generated from events in this research are provided in Table 2.6 in Chapter 2 and Table 3.3 in Chapter 3.

1.3. Particle Property Measurement Methods

Scattering, Absorption, and Extinction Coefficients Measurement Methods

Scattering coefficients can be measured by nephelometers. Nephelometers measure light scattering by integrating photon signals scattered by aerosol from near forward to near backward angles (McMurry, 2000). Absorption coefficients can be measured by filter-based techniques, such as a particle soot absorption photometer (PSAP) (Bond et al., 1999) or an aethalometer

(Hansen et al., 1984). In filter-based techniques, absorption coefficients are measured by comparing transmittance through a particle-free and a particle-laden filter. Measured transmittance is corrected to absorption coefficient through empirical equations that account for the effects of particle scattering of light and accumulation on the filter. Absorption coefficients can also be measured by photoacoustic spectroscopy (Adams, 1988), which uses sensitive microphones to measure pressure change due to heat release of PM after light absorption.

Extinction coefficients can be measured in real-time by photoacoustic extinctiometer (PAX), extinction cell, open-path laser transmissometer (OP-LT), open-path Fourier transform infrared spectroscopy (OP-FTIR), and micropulse light detection and ranging (lidar; MPL). PAX is a combination of scattering measurement by nephelometer and absorption measurement by photoacoustic cell (Droplet Measurement Technologies, 2013). Extinction coefficients are obtained by summing the scattering and absorption coefficients. Extinction cells measure path-integrated extinction by measuring transmittance of light within an enclosed tube filled with PM. Laser light is emitted through the tube to a mirror and reflected back to the laser source. Laser signals before and after traveling the PM-laden tube are measured so that transmittance can be calculated. Path integrated extinction coefficients are calculated using Beer-Lambert Law (Brem, 2013; Virkkula et al., 2005). OP-LT measures path-integrated extinction coefficient in a similar way, but in open environment. It contains a modulated laser of one wavelength that transmits light over an open path of 60 m, and is then reflected by a retro-reflector back to the OP-LT. The method to obtain open path extinction coefficients are the same as for the extinction cell. OP-FTIR measures path-integrated extinction coefficient similar to OP-LT, but it can measure extinction coefficients at a spectrum of wavelengths. MPL measures range-resolved backscattered light signals that can be converted to range-resolved extinction coefficients. It

contains a modulated laser transmitter and a detector that measures backscattered light as a function of distance. The distance is measured based on the travel time of light. The range-resolved backscattered light as photon counts are corrected and processed by the lidar equation to obtain the range-resolved extinction coefficients. Several methods are available to convert backscattered light signals into extinction coefficients, including near-end and far-end lidar equation inversion methods. These two methods are compared in this research, and are described in detail in Section 4.3.

Optical Remote Sensing (ORS) Devices

OP-LT, OP-FTIR, and MPL are considered as optical remote sensing (ORS) devices, which are defined as devices that use electromagnetic wave (e.g., visible light) to measure pollutant concentrations at a distance away from a source. These three devices are further classified as active ORS devices because they use transmitted laser to obtain measurements. These devices are in contrast to passive ORS devices that use background light to obtain measurements. Examples of passive ORS devices are digital cameras, which are portable and self-contained devices that primarily capture and record still pictures, and digital video camera recorders (camcorders), which primarily capture and record videos. Both of them are introduced in Section 1.5.

PM Mass Concentration Measurement Methods

The USEPA Federal Reference Method (FRM) for measuring PM mass concentration is an integrated gravimetric filter measurement method (Noble and Vanderpool, 2001; USEPA, 2013). The method requires a sampler that draws air at a known flow rate through a filter to collect PM. PM mass concentration is calculated from the flow rate, sampling time, and mass of PM collected on the filter. The limitation of this method is that the time resolution of the measurements cannot be below the order of hours. Several Federal Equivalent Methods (FEMs)

exist for measuring PM mass concentration in real-time (less than order of minutes). An example is the tapered element oscillating microbalance (TEOM) (USEPA, 2013), which measures PM mass accumulating on a filter that is placed on a vibrating tapered element. As mass of PM on the filter increases, there is a commensurate reduction in the tapered element's vibrating frequency, so PM mass is inferred from vibration frequency measurements. Another FEM makes use of a beta attenuation monitor (BAM) (USEPA, 2013), which measures PM mass by measuring the transmission of beta radiation across PM-laden filter tapes. Other non-FEM methods include the use of DustTrak, an instrument which utilizes PM scattering properties to infer PM mass concentration. To measure PM mass concentration in certain size range, such as PM_{10} and $PM_{2.5}$, devices such as cyclones (e.g., Very Sharp Cut Cyclone, VSCC (Kenny et al., 2004)) or impactors (e.g., Well-type Impactor Ninety-Six, WINS (Peters, 2001)) are used upstream of the PM monitoring instruments to enable measurements for the desired size fraction.

Particle Size Distribution Measurement Methods

The choice of instrument to measure PSD depends on the size range of interest, PM concentration, size resolution, and sampling time. The micro-orifice uniform deposit impactor (MOUDI) measures PSD from 0.056 to 18 μm in eight size bins based on cascade impactor principle (Marple et al., 1991). The optical particle sizer (OPS) measures PSD based on measurements of particle scattering phase functions, which relate to particle size according to Mie-Lorentz Theory. OPSs are reported to measure particle diameters ranging from 0.01 to 3000 μm (e.g., Horiba LA-950). The aerodynamic particle sizer (APS) measures PSD between 0.5 and 20 μm in real time (1 s resolution) by measuring the speed of each particle using two laser beams after acceleration of particle by a nozzle (e.g., TSI Model 3321). Larger particles will be accelerated to a lower speed because of larger inertia. The scanning mobility particle sizer (SMPS) measures PSD between 0.0025 and 1 μm in near real-time (16-s resolution) by

measuring the electrical mobility of particles (Wang and Flagan, 1990). Open path ORS methods have also been used to measure PSD, where path-integrated extinction coefficients were measured at eight wavelengths, using OP-FTIR and OP-LT. Assuming particle sphericity, PSD was back-calculated from the extinction coefficients in eight wavelengths (0.67, 2.4, 3.5, 3.8, 4.1, 4.4, 4.9, and 13.2 μm) using Mie-Lorentz Theory and an assumed particle refractive index (Varma et al., 2006). Scanning electron microscope (SEM) coupled with energy dispersive X-ray (EDX) spectroscopy is used to obtain PSDs coupled with mineral composition by analyzing these two properties for number of particles in the order of 1,000 to 10,000, so that a particle distribution of sizes and minerals can be obtained (Ebert et al., 2002; Gillies et al., 2010; Kandler et al., 2007; Pachauri et al., 2013).

1.4. Fugitive PM Mass Emission Measurement Methods

Fugitive PM emissions have been previously measured and modelled by various methods. These methods include BangBox, carbon mass balance, testing re-entrained aerosol kinetic emissions from roads (TRAKER), AP-42 model, flux tower, and optical remote sensing (ORS). In this section, these methods will be briefly discussed.

BangBox Method

The BangBox method is a stationary single-point fugitive dust EF measurement method to measure fugitive PM emissions specifically from OB or OD of energetic materials, which include propellants and explosives. The method involves a chamber (930 m^3) known as a BangBox (Mitchell and Suggs, 1998), where small quantities (0.1 – 3 kg) of energetic materials are burned or detonated (Mitchell and Suggs, 1998). Air within the BangBox is mixed and concentration of PM is determined by filter measurement. PM EFs are determined from the measured PM concentrations, the enclosure volume, and the mass of energetic materials burned or detonated.

Carbon Mass Balance Method

The carbon mass balance method is a mobile single-point fugitive dust EF measurement method that is used to determine fugitive PM EFs from burning or detonation of energetic materials. In this method, a sampling device, which contains a filter to measure PM mass concentration and a non-dispersive infrared sensor to measure carbon dioxide concentration, is brought into a plume by an aircraft (Johnson, 1992) or a balloon (Aurell et al., 2011, 2012). Fugitive PM EF is determined by dividing the measured PM mass concentration by the measured carbon dioxide concentration, multiplied by the mass fraction of carbon in the energetic material. The method assumes that all carbon in the energetic material is converted to carbon dioxide after burning or detonation, and the ratio of PM to carbon dioxide is constant within the entire plume.

Testing Re-entrained Aerosol Kinetic Emissions from Roads (TRAKER)

TRAKER is a van that is used to determine fugitive EFs from roads due to its travel, so that the effect of road condition on PM EF can be determined (Etyemezian et al., 2006). TRAKER method is a mobile single-point fugitive PM EF measurement method. The van contains two DustTraks that are installed behind two front wheels and a DustTrak that is installed at the front of the van. As the van travels, real-time PM concentration generated from wheel movement is measured through the two DustTraks and the background PM concentration is measured at the front of the van. Fugitive PM EF of TRAKER travelling on roads is calculated from the background-corrected PM concentration.

USEPA AP-42 Model

In Chapter 13.2.2 of the AP-42 model (USEPA, 2016b), fugitive PM EF generated from vehicles travelling on an unpaved road is related to the road silt and moisture content, and vehicle weight and speed. The models for industrial roads and publicly accessible roads are shown in Equations (1.11) and (1.12), respectively (USEPA, 2016b):

$$EF\ (g/km) = 281.9k(S/12)^{0.9}(W/3)^{0.45} \quad (1.11)$$

$$EF\ (g/km) = 281.9(k'(S/12)(V/30)^{0.5}(m/0.5)^{-0.2}-C) \quad (1.12)$$

In Equation (1.11), k = 0.15 for $PM_{2.5}$ and k = 1.5 for PM_{10}, S is silt content, and W is mean vehicle weight (US short ton). In Equation (1.12), k' = 0.18 for $PM_{2.5}$ and k' = 1.8 for PM_{10}, S is silt content, V is mean vehicle speed (mph), m is surface soil moisture content (% by mass), C is PM mass EF due to vehicle exhaust, brake wear, and tire wear (lb/mile). C is negligible compared to the fugitive PM emissions (< 1% of fugitive PM emissions, (USEPA, 2016b)). The model for industrial roads (Equation (1.11)) applies to vehicles with mean vehicle weight between 1.8 and 260 tonnes (2 and 290 US short tons), while the model for publicly accessible roads (Equation (1.12)) applies to vehicles with mean vehicle weight between 1.4 and 2.7 tonnes (1.5 and 3 US short tons).

Flux Tower Method

The flux tower method is a stationary and multiple point-measurement method to measure fugitive PM EF from mobile sources (Gillies et al., 2005; Kuhns et al., 2010). Fugitive dust EFs are estimated from measurements of PM mass concentrations with calibrated DustTraks, and wind speed and direction with anemometers. These instruments are all mounted on one or more towers in vertical arrays.

Optical Remote Sensing (ORS) Method

Optical remote sensing (ORS) methods are the focus of this research. These methods have been used to measure fugitive PM emissions from agricultural activities (Holmén et al., 1998; Wojcik et al., 2008) and military operations (Du et al., 2011a, 2011b). As discussed in Section 1.1, fugitive PM emission contributes to considerable amount of total primary PM emission, but the fugitive PM mass EFs are highly uncertain because they are aloft, heterogeneous, have short lifetimes, and can exist within large spatial scales. The advantages of

ORS methods in measuring fugitive PM are: 1) measurements can be done at a distance from the fugitive PM source, and 2) spatial distribution of fugitive PM concentrations can be determined with a few devices in near real-time. The ORS methods that are considered in this research involve the use of MPL that measures range-resolved extinction coefficients. To infer PM mass concentration from extinction coefficient measurements by MPL, MEE of PM is measured by additional devices that will be described below. Fugitive PM EFs are then obtained by integrating PM mass concentrations with wind data, plume cross-sectional areas, and duration of events.

In previous research (Du et al., 2011a; Varma et al., 2006), MPL measurement was combined with OP-FTIR and OP-LT measurements to obtain PM mass EF, which is referred as the *original-ORS* method hereafter. MEE was determined by measuring PSD using OP-FTIR and OP-LT, and assuming all particles are spherical, and values of particle density and refractive index are known and constant. Such assumptions should be avoided because, as described in Section 1.1, dust particles are not spherical and compose of various minerals. In this research, MEE measurement using OP-FTIR and OP-LT is replaced by point-measurements of PM mass concentration and extinction coefficient at the same location (Hashmonay et al., 2009). Since the PM mass concentration measurement device is not ORS, the method is called *hybrid-ORS* method hereafter. The hybrid-ORS method will be described in detail in Section 2.3, but it is worth mentioning here that the method avoids the assumptions of particle sphericity and single particle density and refractive index.

1.5. Opacity Measurement Methods

As described in Section 1.2, opacity is defined as the percentage of light that is attenuated by a medium. Plume opacity from stationary sources is measured for regulatory purposes (USEPA, 1993). In this section, the history of opacity measurement will be briefly discussed.

Ringelmann Method

Opacity measurement can be traced back in the late 19th century, when plume opacity was determined by the Ringelmann method. In this method, black plume emission is matched with four reference charts with different shadings. A code that represents a specific reference chart is reported (USEPA, 1993). While opacity was not formally measured in this method, the rules of using human observers to observe plume emission were established here.

USEPA Method 9

The use of opacity as a unit of visible emission measurement was first introduced in the 1960s, and the measurement was extended to white plumes. In 1974, the USEPA Method 9 was promulgated, replacing the Ringelmann method (USEPA, 1993). In this method, certified human observers read the opacity of a smokestack, to the nearest 5%, at 15 s intervals for at least 24 consecutive observations. The average opacity for these observations is reported (USEPA, 1993). Observers need to be certified by taking the visible emission evaluation training course (smoke school), which requires the observers to read 25 black and 25 white plumes with varying opacity values generated by a calibrated smoke generator. The observers pass the course if, for each plume color, the average absolute error does not exceed 7.5% opacity and none of the individual absoluter error exceed 15% opacity (USEPA, 1993).

Use of Digital Cameras and Camcorders

As mentioned in Section 1.3, digital cameras and camcorders are passive ORS devices because they use background light to obtain measurements as images. Digital cameras save

images as a two-dimensional matrix of pixel values (PVs), which relate to light exposure of each pixel, using semiconductor sensors such as charge-coupled device (CCD) or complementary metal-oxide semiconductor (CMOS). Digital camcorders record videos by saving the images as frames similar to digital cameras, at a frame rate of 24 or 30 Hz. The relationship between light exposure of a pixel to a PV of a digital camera or a digital camcorder is called a response curve, which is non-linear (Du, 2007). An example of a response curve is shown in Figure 1.1. Details in determining the response curve are discussed in Section 5.3. To obtain color pictures, a Bayer filter is laid on the sensor such that each pixel can be exposed to red, green, or blue light (RGB, Figure 1.2), resulting a pixel registering a PV for one of the three colors (Bayer, 1976). The PVs of a pixel for the other two colors are obtained by interpolating the neighboring PVs that have the color measured. The grayscale PV is a weighted average of RGB PVs in accordance with Recommendation BT.601 (International Telecommunication Union, 2011).

Figure 1.1. An example of camera response curve.

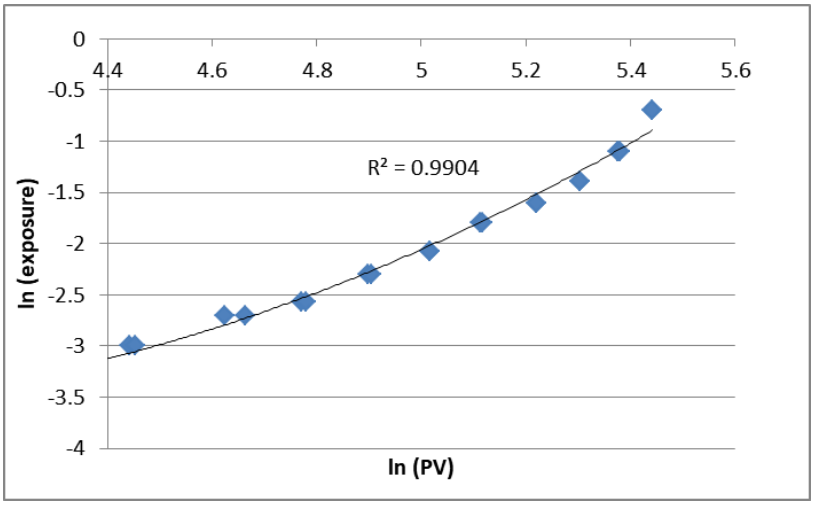

Figure 1.2. An example of a Bayer filter (Bayer, 1976). Each square represents a pixel. R = red, G = green, and B = blue.

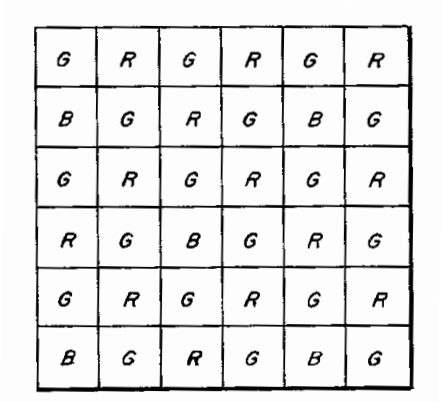

In 2012, the USEPA approved the use of digital cameras to measure opacity as an alternative method (ALT 082), (USEPA, 2012), which is based on ASTM D7520 (ASTM Standard D7520, 2016). Several methods that use digital cameras to measure plume opacity were developed to reduce measurement subjectivity from human observers. One method is digital opacity compliance system (DOCS), where opacity is determined by performing statistical analysis of pixels on select region of digital pictures (McFarland et al., 2003). Another method, which is part of this research, is the digital optical method (DOM). Opacity is calculated from exposure through the contrast or transmission models (Du, 2007; Du et al., 2007). In the contrast model, two contrasting backgrounds are used to determine plume opacity. In the transmission model, one background that has color contrast against the plume is used to determine plume opacity, which is an advantage over the contrast model because there is less limitation in finding backgrounds for capturing digital pictures. However, the transmission model needs a diffusive scattering parameter (K), which describes the plume color relative to the background color, for the opacity calculation. Before this research, K values were calculated only for white plume against blue sky background, and black plume against blue or white sky backgrounds (Du, 2007). This limits the applicability of the transmission model in measuring plume opacity. It is important to provide K values for a wider range of backgrounds for white and black plumes to

improve the applicability of the transmission model. In both methods, exposures of select regions are required and calculated from the mean PV with the camera response curve. Details of DOM are described in Section 5.3, and the mathematical derivation of DOM can be found in Du (2007). Before this research, DOM had been fully tested only with digital cameras, but not with camcorders or smartphones. Part of this research implements DOM for smartphones and camcorders.

1.6. Objectives and Significance of Dissertation Research

The overall goal of this research is to improve our understandings in using active and passive ORS in measuring PM in non-ambient concentrations. The research is important because ORS method can measure PM without traditional sampling, in real-time, and (in the case of MPL) range-resolved, allowing PM measurement through plume cross-sections. Although these two methods have been described by Du (2007), the methods are further developed in this research to improve their applications in field. The results from this research may serve the purposes to: 1) improve the versatility of the two ORS methods that are used in actual environment; 2) inform the technology users on the strengths and weaknesses of using ORS for PM monitoring; and 3) serve the ORS results as benchmarks for comparing with technologies other than ORS in measuring PM. The flow chart of my dissertation research is shown in Figure 1.3. It displays the objectives and shows how the objectives connect to each other toward the overall goal of this research.

Figure 1.3. Outline diagram of the dissertation research.

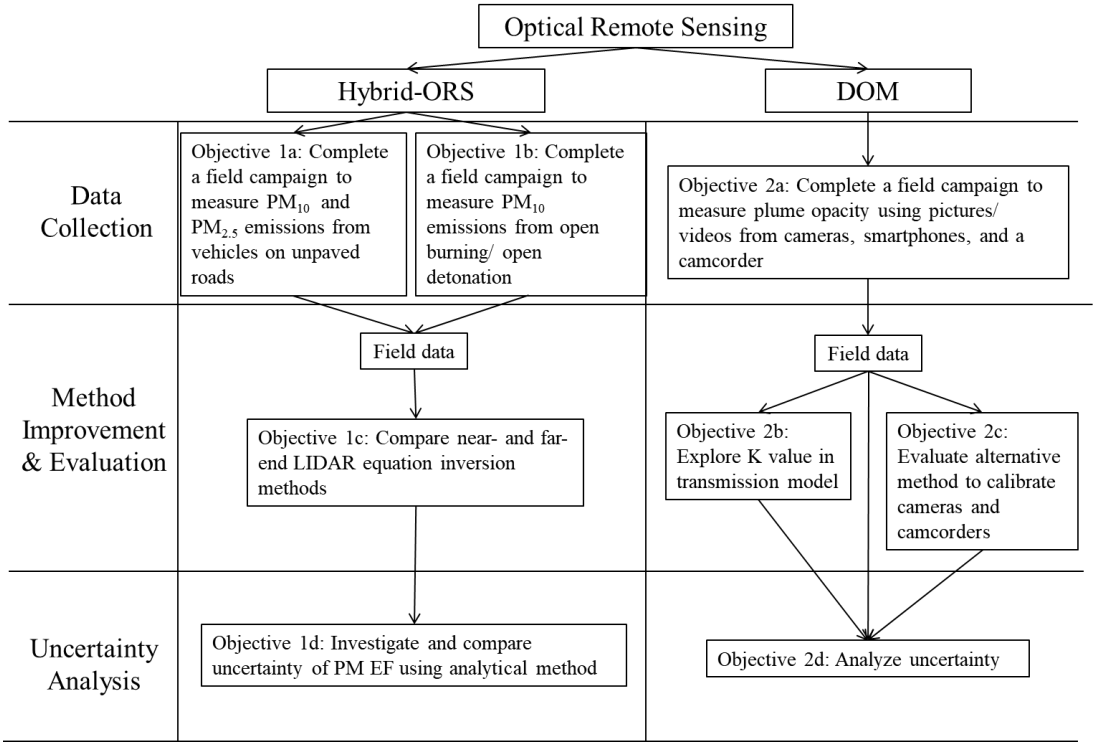

The objectives are described as follows:

Objective 1: Improve and Implement Hybrid ORS Method to Measure Fugitive PM Emission for Mobile and Stationary Sources

The hybrid-ORS method was developed from the original-ORS method by Du et al. (2011a) and Hashmonay et al. (2009), and then implemented in two field campaigns. In the first field campaign *(Objective 1a)*, PM fugitive emissions from select military vehicles travelling on unpaved roads were measured by the hybrid-ORS method. In determining MEE, extinction coefficients were measured by OP-LT and mass concentrations of $PM_{2.5}$ and PM_{10} were measured by DustTrak. In the second field campaign *(Objective 1b)*, PM fugitive emissions from open burning and open detonation (OB/OD) of energetic materials were measured by hybrid-ORS method. In determining MEE values, extinction coefficients were measured concomitantly by MPL light back scattering and PM_{10} mass concentrations were measured by TEOM. Mobile

vehicle PM source on unpaved roads was studied because of its large contribution of PM emission, while OB/OD PM source was studied because amount of PM emissions need to be known for regulation. The results from these field campaigns are presented in Chapter 2 and 3.

In *Objective 1c*, two methods of converting MPL backscattered light signals into extinction coefficients, which are the near-end (Du et al., 2011a) and the far-end (Klett, 1981) lidar equation inversion methods, are compared. Details of these two methods and their results can be found in Chapter 4.

In *Objective 1d*, the EF measurement uncertainties for hybrid-ORS method are investigated in error propagation approach. This includes: 1) calculation of normalized relative backscatter (NRB) signals from MPL raw photon count data (Welton and Campbell, 2002), 2) calculation of extinction coefficients from NRB signals (using either near- or far-end inversion method), 3) calculation of mass concentrations from extinction coefficients, and 4) calculation of EF from PM mass concentrations, wind data, cross-sectional area of the plumes, and duration of event, and normalizing source strength (e.g., vehicle distance travelled and mass of energetic material burned/detonated). The calculations are based on the MPL data collected in the field campaigns. The new contribution in this objective is to obtain overall uncertainty of hybrid-ORS method in determining EF. Details of the methods and results for this objective can be found in Chapter 4.

Significance of Objective 1

The hybrid-ORS method improves the method to measure MEE values compared to the original-ORS method because the hybrid-ORS method does not require information about particle properties and does not assume spherical particles. This is the first time to apply the hybrid-ORS method to determine fugitive PM emissions from OB/OD. Such method is appropriate for this fugitive source because the method allows safe PM measurement by placing

the instruments far away from the burning or detonation sites. Comparing that far-end lidar equation inversion method with the near-end method is important because, as described later in Chapter 4, there is a concern of the stability of the near-end method that was previously used for calculating extinction coefficients from MPL data. The inversion instability may cause erroneous EF results for more opaque plumes. Determining uncertainty allows assessment of EF data quality. It also allows the evaluation of parameters that contribute to the largest uncertainty on EF, so that future research can be suggested to reduce the uncertainty of the most influential parameters.

Objective 2: Improve and Implement Digital Cameras, Smartphone Cameras, and Camcorders (DOM) to Measure Plume Opacity

In *Objective 2a*, the use of DOM is extended to smartphone cameras and camcorders that have yet to be evaluated and are my new contribution. They were calibrated and deployed in a field campaign to test the plume opacity measurements and compare to reference measurements provided by Illinois Environmental Protection Agency (IEPA). The results for smartphone cameras can be found in Chapter 5, while the results for camcorders can be found in Chapter 6.

In *Objective 2b*, the diffusive scattering parameters (K) in the transmission model, for select backgrounds (white sky, dark gray roof, and red background) and smoke colors (black and white), are calculated using field picture data. The calculated K values are then verified by the modelled K values that were derived by Du (2007) from radiative transfer equation. Such results are shown in Chapter 5.

In *Objective 2c*, a new method that calibrates PV to exposure, using exposure value (EV) compensation, is tested and evaluated. Experiments are done with automatic exposure controlled cameras and a camcorder to test determining camera response curves using EV compensation, and evaluate the resulting plume opacity. The description of the previous and the new calibration

methods, and the opacity value comparison due to the calibration methods, are found in Chapter 5.

In *Objective 2d*, uncertainty of opacity measurements due to camera calibration and background choice are determined through experiments and error propagation of the two DOM models developed by Du et al. (2007). These uncertainty results are shown in both Chapter 5 and 6. All analyses above will be performed as a function of red, green, and blue wavelengths (RGB) in addition to grayscale.

Significance of Objective 2

Showing that smartphone cameras can be used to measure opacity is important because smartphones have the potential to integrate geo-positioning and internet communication into mobile application software that facilitates plume opacity data collection and distribution. Showing that camcorders can remotely measure opacity allows real-time opacity measurements that help to assess the measurement of variability due to process and environment changes. Calculating K values for a larger selection of backgrounds will extend the applicability of DOM's transmission model, which by requiring only one background is more flexible than contrast model that requires two contrasting and co-located backgrounds. Introducing a new method in calibrating response curves of automatic exposure controlled cameras and camcorders eliminates the use of a calibrated manual exposure controlled camera to perform calibration. This elimination adds convenience in the response curve calibration process, so that users can feasibly perform their own calibrations of the cameras and camcorders. Knowledge of the opacity measurement uncertainty by DOM allows a better understanding of the important sources of errors in calculating opacity from digital images. Studying all of the above measurements in RGB allows a better understanding of the dependence of plume opacity and K values on

wavelength of light. From such results, recommendations can be made on the choice of background colors in optimizing opacity measurements.

1.7. References

Adams, K.M. (1988). Real-time In Situ Measurements of Atmospheric Optical Absorption in the Visible Via Photoacoustic Spectroscopy. 1: Evaluation of Photoacoustic Cells. *Appl. Opt.* 27: 4052–4056.

Anenberg, S.C., Schwartz, J., Shindell, D., Amann, M., Faluvegi, G., Klimont, Z., Janssens-Maenhout, G., Pozzoli, L., Van Dingenen, R., Vignati, E., et al. (2012). Global Air Quality and Health Co-benefits of Mitigating Near-term Climate Change Through Methane and Black Carbon Emission Controls. *Environ. Health Perspect.* 120: 831–839.

ASTM Standard D7520 (2013). Standard Test Method for Determining the Opacity of a Plume in the Outdoor Ambient Atmosphere. ASTM International, West Conshohocken, PA.

Aurell, J., Gullett, B.K., Pressley, C., Tabor, D.G., and Gribble, R.D. (2011). Aerostat-lofted Instrument and Sampling Method for Determination of Emissions from Open Area Sources. *Chemosphere* 85: 806–811.

Aurell, J., Gullett, B.K., and Yamamoto, D. (2012). Emissions from Open Burning of Simulated Military Waste from Forward Operating Bases. *Environ. Sci. Technol.* 46: 11004–11012.

Bayer, B.E. (1976). Color Imaging Array. U.S. Patent No. 3971065.

Bohren, C.F. and Huffman, D.R. (1983). Absorption and Scattering of Light by Small Particles. Wiley, New York.

Bond, T.C., Anderson, T.L., and Campbell, D. (1999). Calibration and Intercomparison of Filter-Based Measurements of Visible Light Absorption by Aerosols. *Aerosol Sci. Technol.* 30: 582–600.

Brem, B.T. (2013). Optical Properties of Light Absorbing Organic Carbon Aerosol and its Mixtures at High Sub-saturated Humidities. Ph.D. Dissertation, University of Illinois at Urbana-Champaign, Illinois, USA.

Chow, J.C., Watson, J.G., Park, K., Lowenthal, D.H., Robinson, N.F., and Magliano, K.A. (2006). Comparison of Particle Light Scattering and Fine Particulate Matter Mass in Central California. *J. Air Waste Manage. Assoc.*, 56: 398–410.

Claquin, T., Schulz, M., and Balkanski, Y.J. (1999). Modeling the Mineralogy of Atmospheric Dust Sources. *J. Geophys. Res.* 104: 22243.

Dockery, D.W. and Pope, C.A. (1994). Acute Respiratory Effects of Particulate Air Pollution. *Annu. Rev. Public Health* 15: 107–132.

Droplet Measurement Technologies (2013). Photoacoustic Extinctiometer (PAX). http://www.dropletmeasurement.com/products/airborne/PAX.

Du, K. (2007). Optical Remote Sensing of Airborne Particulate Matter to Quantify Opacity and Mass Emissions. Ph.D. Dissertation, University of Illinois at Urbana-Champaign, Illinois, USA.

Du, K., Rood, M.J., Kim, B.J., Kemme, M.R., Franek, B., and Mattison, K. (2007). Quantification of Plume Opacity by Digital Photography. *Environ. Sci. Technol.* 41: 928–935.

Du, K., Rood, M.J., Welton, E.J., Varma, R.M., Hashmonay, R.A., Kim, B.J., and Kemme, M.R. (2011a). Optical Remote Sensing to Quantify Fugitive Particulate Mass Emissions from Stationary Short-term and Mobile Continuous Sources: Part I. Method and Examples. *Environ. Sci. Technol.* 45: 658–665.

Du, K., Yuen, W., Wang, W., Rood, M.J., Varma, R.M., Hashmonay, R.A., Kim, B.J., and Kemme, M.R. (2011b). Optical Remote Sensing to Quantify Fugitive Particulate Mass Emissions from Stationary Short-Term and Mobile Continuous Sources : Part II. Field Applications. *Environ. Sci. Technol.* 45: 666–672.

Ebert, M., Weinbruch, S., Rausch, A., Gorzawski, G., Hoffmann, P., Wex, H., and Helas, G. (2002). Complex Refractive Index of Aerosols During LACE 98 as Derived from the Analysis of Individual Particles. *J. Geophys. Res.* 107: 8121.

Etyemezian, V., Kuhns, H., and Nikolich, G. (2006). Precision and Repeatability of the TRAKER Vehicle-based Paved Road Dust Emission Measurement. *Atmos. Environ.* 40: 2953–2958.

Fuller, K.A., Malm, W.C., and Kreidenweis, S.M. (1999). Effects of Mixing on Extinction by Carbonaceous Particles. *J. Geophys. Res.* 104: 15,941–15,954.

Gillies, J.A., Etyemezian, V., Kuhns, H., Moosmüller, H., Engelbrecht, J., King, J., Uppapalli, S., Nikolich, G., McAlpine, J.D., Zhu, D., et al. (2010). Particulate Matter Emissions Factors for Dust from Unique Military Activities.

Gillies, J.A., Etyemezian, V., and Kuhns, H. (2005). Effect of Vehicle Characteristics on Unpaved Road Dust Emissions. *Atmos. Environ.* 39: 2341–2347.

Hansen, A., Rosen, H., and Novakov, T. (1984). The Aethalometer—an Instrument for the Real-time Measurement of Optical Absorption by Aerosol Particles. *Sci. Total Environ.* 36: 191–196.

Hashmonay, R.A., Kagann, R.H., Rood, M.J., Kim, B.J., Kemme, M.R., and Gillies, J. (2009). An Advanced Test Method for Measuring Fugitive Dust Emissions Using a Hybrid System of Optical Remote Sensing and Point Monitor Techniques. In Kim, Y.J., Platt, U., Gu, M.B.,

and Iwahashi, H. (Eds), Atmospheric and Biological Environmental Monitoring. Springer Netherlands, 73–81.

Holmén, B.A., Eichinger, W.E., and Flocchini, R.G. (1998). Application of Elastic Lidar to PM_{10} Emissions from Agricultural Nonpoint Sources. *Environ. Sci. Technol.* 32: 3068–3076.

International Telecommunication Union (2011). Studio Encoding Parameters of Digital Television for Standard 4:3 and Wide-screen 16:9 Aspect Ratios (ITU-R BT.601-7). 19.

Johnson, M. (1992). Development of Methodology and Technology for Identifying and Quantifying Emission Products from Open Burning and Open Detonation Thermal Treatment Methods. Field Test Series A, B, And C, Volume 1 Test Summary - Final Report.

Kandler, K., Benker, N., Bundke, U., Cuevas, E., Ebert, M., Knippertz, P., Rodríguez, S., Schütz, L., and Weinbruch, S. (2007). Chemical Composition and Complex Refractive Index of Saharan Mineral Dust at Izaña, Tenerife (Spain) Derived by Electron Microscopy. *Atmos. Environ.* 41: 8058–8074.

Kenny, L.C., Merrifield, T., Mark, D., Gussman, R., and Thorpe, A. (2004). The Development and Designation Testing of a New USEPA-Approved Fine Particle Inlet: a Study of the USEPA Designation Process. *Aerosol Sci. Technol.* 38: 15–22.

Khalizov, A.F., Xue, H., Wang, L., Zheng, J., and Zhang, R. (2009). Enhanced Light Absorption and Scattering by Carbon Soot Aerosol Internally Mixed with Sulfuric Acid. *J. Phys. Chem. A* 113: 1066–1074.

Klett, J.D. (1981). Stable Analytical Inversion Solution for Processing Lidar Returns. *Appl. Opt.* 20: 211–220.

Kuhns, H., Gillies, J., Etyemezian, V., Nikolich, G., King, J., Zhu, D., Uppapalli, S., Engelbrecht, J., and Kohl, S. (2010). Effect of Soil Type and Momentum on Unpaved Road

Particulate Matter Emissions from Wheeled and Tracked Vehicles. *Aerosol Sci. Technol.* 44: 187–196.

Malm, W.C. (1999). *Introduction to Visibility.* Colorado State University, Fort Collins, CO.

Marple, V.A., Rubow, K.L., and Behm, S.M. (1991). A Microorifice Uniform Deposit Impactor (MOUDI): Description, Calibration, and Use. *Aerosol Sci. Technol.* 14: 434–446.

McFarland, M.J., Terry, S.H., Stone, D.A., Rasmussen, S.L., and Calidonna, M.J. (2003). Evaluation of the Digital Opacity Compliance System in High Mountain Desert Environments. *J. Air Waste Manage. Assoc.* 53: 724–730.

McMurry, P. (2000). A Review of Atmospheric Aerosol Measurements. *Atmos. Environ.* 34: 1959–1999.

Mishchenko, M.I. (2009). Electromagnetic Scattering by Nonspherical Particles: a Tutorial Review. *J. Quant. Spectrosc. Radiat. Transf.* 110: 808–832.

Mitchell, W.J. and Suggs, J.C. (1998). Emission Factors for The Disposal of Energetic Materials by Open Burning and Open Detonation (OB/OD); EPA/600/R-98/103.

Noble, C. and Vanderpool, R. (2001). Federal Reference and Equivalent Methods for Measuring Fine Particulate Matter. *Aerosol Sci. Technol.* 457–464.

Nousiainen, T. (2009). Optical Modeling of Mineral Dust Particles: a Review. *J. Quant. Spectrosc. Radiat. Transf.* 110: 1261–1279.

Pachauri, T., Singla, V., Satsangi, A., Lakhani, A., and Kumari, K.M. (2013). SEM-EDX Characterization of Individual Coarse Particles in Agra, India. *Aerosol Air Qual. Res.* 13: 523–536.

Peters, T. (2001). Design and Calibration of the EPA $PM_{2.5}$ Well Impactor Ninety-six (WINS). *Aerosol Sci.* 34: 389–397.

Petty, G.W. (2006). A First Course in Atmospheric Radiation. 2nd ed. Sundog Publishing, Madison, WI.

Pope, C. and Dockery, D. (2006). Health Effects of Fine Particulate Air Pollution: Lines That Connect. *J. Air Waste Manag. Assoc.* 56: 709 –742.

Ralph, J. and Chau, I. (1993). Mindat.org - the Mineral and Locality Database. http://www.mindat.org.

Seinfeld, J.H. and Pandis, S.N. (2016). Atmospheric Chemistry and Physics. 3rd ed. Wiley, Hoboken, NJ.

Sokolik, I.N. and Toon, O.B. (1999). Incorporation of Mineralogical Composition into Models of the Radiative Properties of Mineral Aerosol from UV to IR Wavelengths. *J. Geophys. Res.* 104: 9423.

Storelvmo, T., Hoose, C., and Eriksson, P. (2011). Global Modeling of Mixed-phase Clouds: the Albedo and Lifetime Effects of Aerosols. *J. Geophys. Res.* 116: D05207.

Tegen, I. and Lacis, A. (1996). Modeling of Particle Size Distribution and its Influence on the Radiative Properties of Mineral Dust Aerosol. *J. Geophys. Res.* 101: 1923719244.

USEPA (1993). *Visible Emissions Field Manual EPA Methods 9 and 22.* Office of Air Quality Planning and Standards, Washington, DC.

USEPA (2004). Air Quality Criteria for Particulate Matter.

USEPA (2012). Approved Alternatives. https://www.epa.gov/emc/broadly-applicable-approved-alternative-test-methods. (Accessed February 2018).

USEPA (2013). List of Designated Reference and Equivalent Methods.

USEPA (2015). Emissions Inventories. http://www.epa.gov/ttn/chief/eiinformation.html. (Accessed February 2015).

USEPA (2016a). Particulate Matter (PM) Pollution. https://www.epa.gov/pm-pollution. (Accessed February 2018).

USEPA (2016b). Emissions Factors & AP 42, Compilation of Air Pollutant Emission Factors. http://www.epa.gov/ttnchie1/ap42. (Accessed July 2016).

Upadhyay, J.K., Auvermann, B.W., Paila, A.N., and Hiranuma, N. (2008). Open-path Transmissometry to Determine Atmospheric Extinction Efficiency Associated with Feedyard Dust. *Trans. ASABE* 51: 1433–1441.

Varma, R.M., Hashmonay, R.A., Du, K., Rood, M.J., Kim, B.J., and Kemme, M.R. (2006). A Novel Method to Quantify Fugitive Dust Emissions Using Optical Remote Sensing. In, Platt,U. and Kim,Y. (Eds), Advanced Environmental Monitoring. Springer-Verlag GmbH, 143–154.

Virkkula, A., Ahlquist, N.C., Covert, D.S., Sheridan, P.J., Arnott, W.P., and Ogren, J. a. (2005). A Three-Wavelength Optical Extinction Cell for Measuring Aerosol Light Extinction and its Application to Determining Light Absorption Coefficient. *Aerosol Sci. Technol.* 39: 52–67.

Wang, S.C. and Flagan, R.C. (1990). Scanning Electrical Mobility Spectrometer. *Aerosol Sci. Technol.* 13: 230–240.

Watson, J.G. and Chow, J.C. (2000). Reconciling Urban Fugitive Dust Emissions Inventory and Ambient Source Contribution Estimates: Summary of Current Knowledge and Needed Research. DRI Document No. 6110.4F.

Welton, E.J. and Campbell, J.R. (2002). Micropulse Lidar Signals: Uncertainty Analysis. *J. Atmos. Ocean. Technol.* 19: 2089–2094.

Wojcik, M.D., Bingham, G.E., Marchant, C.C., Zavyalov, V. V., Ahlstrom, D.J., Moore, K., Wilkerson, T.D., Hipps, L.E., Martin, R.S., Hatfield, J.L., et al. (2008). Lidar Based

Particulate Flux Measurements of Agricultural Field Operations. *IGARSS 2008 - 2008 IEEE Int. Geosci. Remote Sens. Symp.* IV – 263–IV – 266.

PART II: IMPROVEMENTS IN USING OPTICAL REMOTE SENSING TO MEASURE PARTICULATE MATTER EMISSION FACTORS FROM FUGITIVE SOURCES

CHAPTER 2: FUGITIVE PARTICULATE MATTER EMISSIONS TO THE ATMOSPHERE FROM TRACKED AND WHEELED VEHICLES IN A DESERT REGION BY HYBRID-OPTICAL REMOTE SENSING[1]

2.1 Abstract

A hybrid-optical remote sensing (hybrid-ORS) method was developed to quantify mass emission factors (EFs) for fugitive particulate matter with aerodynamic diameters ≤ 10 μm (PM_{10}) and ≤ 2.5 μm ($PM_{2.5}$). In-situ range-resolved extinction coefficient and concurrent point measurements of PM_{10} and $PM_{2.5}$ mass concentrations are used to quantify two-dimensional (2-D) PM_{10} and $PM_{2.5}$ mass concentration profiles. Integration of each 2-D mass concentration profile with wind data, event duration, and source type provides the corresponding fugitive PM_{10} and $PM_{2.5}$ EFs. This method was used to quantify EFs for fugitive PM_{10} and $PM_{2.5}$ emitted from tracked and wheeled vehicles travelling on unpaved roads in a desert region. The EFs for tracked vehicles ranged from 206 g/km to 1,738 g/km for PM_{10} and from 78 g/km to 684 g/km for $PM_{2.5}$, depending on vehicle speed and vehicle type. The EFs for the wheeled vehicle ranged from 223 g/km to 4,339 g/km for PM_{10} and from 44 g/km to 1,627 g/km for $PM_{2.5}$. Field implementation of the hybrid-ORS method demonstrates that the method can rapidly capture multiple profiles of the PM plumes and is well suited for improved quantification of fugitive PM EFs from vehicles traveling on unpaved roads.

[1] Reprinted, with permission and minor revisions, from Yuen, W., Du, K., Koloutsou-Vakakis, S., Rood, M.J., Kim, B.J., Kemme, M.R., Hashmonay, R.A., and Meister, C. (2015). Fugitive Particulate Matter Emissions to the Atmosphere from Tracked and Wheeled Vehicles in a Desert Region by Hybrid-Optical Remote Sensing. *Aerosol Air Qual. Res.* 15: 1613–1626.

2.2 Introduction

Concentrations of particulate matter (PM) with aerodynamic diameters ≤ 10 μm (PM_{10}) and ≤ 2.5 μm ($PM_{2.5}$) have positive correlations with the occurrence of human respiratory and cardiac illnesses (Dockery and Pope, 1994; Pope and Dockery, 2006). PM impairs visibility (Watson, 2002) and influences climate change by scattering and absorbing solar radiation (Storelvmo et al., 2011). Fugitive PM refers to PM that is discharged to the atmosphere, but not in a confined flow stream (USEPA, 2011; Watson and Chow, 2000). Such is the case with fugitive PM emitted to the atmosphere when vehicles travel on unpaved surfaces. According to the 2011 U.S. National Emissions Inventory (NEI), of the primary combined natural and anthropogenic PM emissions to the atmosphere, fugitive emissions from all paved and unpaved roads were 54% and 23% of the PM_{10} and $PM_{2.5}$ emissions, respectively (USEPA, 2015b). NEI estimates are based on PM mass emission factors (EFs) in USEPA's AP-42 database and are rated as highly uncertain (USEPA, 2015a). The high uncertainty reflects the nature of fugitive emission plumes that can: 1) have short lifetimes (often less than one minute) (Du et al., 2013; McFarland et al., 2007), 2) exist with large spatial scales (tens to hundreds of meters) (Du et al., 2011a), 3) can travel aloft, and 4) be heterogeneous (McFarland et al., 2007). There remains a need for improving the accuracy of fugitive PM EFs (Du et al., 2011a) with measurement methods appropriate for the characteristics of fugitive PM plumes to improve national and global PM emission inventories.

Optical remote sensing (ORS) methods are well suited to quantify fugitive PM EFs because they allow real-time and in-situ monitoring of emissions and they measure multiple cross-sections of the plumes over a large range of length scales (tens to hundreds of meters) over time periods of tens of seconds. Thus, ORS methods have the potential to facilitate fast and cost-

effective updating of EFs according to the needs of NEIs (Miller et al., 2006; NARSTO, 2005). Another method used for estimating fugitive PM EFs is the flux tower method, where fugitive PM EFs are quantified with multiple point-measurements of PM mass concentrations, using optically-based instruments (i.e., DustTraks™). The instruments are located in vertical and horizontal arrays mounted on one or more towers (Gillies et al., 2005; Kuhns et al., 2010), so that multiple areas of the plume can be sampled simultaneously. As with other optical methods, to allow quantification of PM mass EFs, ORS measurements entail conversion of optical measurements into PM mass concentrations. This is typically achieved by quantifying the mass extinction efficiency (MEE) values of the PM, which is defined as the ratio of the measured light extinction to measured PM mass concentration.

Some fugitive PM mobile sources have been characterized previously by ORS methods. These include movement of vehicles on unpaved roads (Du et al., 2011b; Gillies et al., 2005), movement of helicopters over unpaved surface (Du et al., 2011b), movement of agricultural tractors (Holmén et al., 1998) and harvesters (Faulkner et al., 2009), and open burning and detonation (Yuen et al., 2014). Fugitive PM EFs of military and civilian vehicles have been compared using flux tower method, for vehicles traveling from 10 to 80 km/hr, and vehicle masses between 1 and 17 tonnes (Gillies et al., 2005).

This paper describes a new hybrid-ORS method and its results from field implementation to measure fugitive PM EFs for PM_{10} and $PM_{2.5}$ for tracked and wheeled military vehicles traveling on unpaved roads in a desert region. The difference between the ORS method reported in Du et al. (2011a) and this hybrid-ORS method is in the way the MEE values for PM_{10} and $PM_{2.5}$ are determined. In the earlier ORS method, MEE values were determined by first determining particle size distributions (PSDs) using wavelength-dependent light extinction

measurements obtained with an open path-laser transmissometer (OP-LT) and an open-path Fourier Transform Infrared spectrometer. Then, MEE values were calculated using PSDs and assumed particle density and refractive index using Mie-Lorenz theory (Du et al., 2011a; Varma et al., 2006). In the hybrid-ORS method reported here, MEE values are determined by simultaneously measuring real-time light extinction with an OP-LT and PM_{10} and $PM_{2.5}$ mass concentrations with optically based DustTrak™ monitors. This hybrid-ORS method offers more operational simplicity, since a PM mass concentration monitor is used that does not require assumptions pertaining to particle density or refractive index. The hybrid-ORS method also enables measurement across the entire plume cross-section. The EFs determined by this hybrid-ORS method are then compared to EFs derived from the flux tower method and AP-42 models. Current AP-42 EFs for vehicle movement on unpaved industrial roads have been based on consideration of vehicles used in a variety of industries such as surface mining and construction, and they correspond to vehicles with masses between 2 and 260 tonnes, traveling from 8 to 69 km/hr. These values encompass the characteristics of the vehicles studied here which traveled from 8 to 69 km/hr with masses between 12 and 64 tonnes (USEPA, 2015a). EFs measured in this research may be used by facilities using vehicles that travel on unpaved roads with similar masses and modes of traction to assess the contribution of such vehicles to PM emissions and subsequently impacts of the operation of such vehicles on air quality. The method is also applicable to sources that produce fugitive PM plumes.

2.3 Methods

EF Measurement with the Hybrid-ORS Method

EFs were determined by integrating two dimensional (2-D) PM mass concentration profiles during each plume event with wind speed, wind direction, and duration of each event (Eq. (2.1), Figure 2.1):

$$\mathrm{EF} = \frac{1}{Y} \times \sum_{t=0}^{T} \left(\sum C_m(\Delta A, t)\Delta A \right) u(z) \cos\theta \Delta t \quad \left(\text{g-PM/km}\right) \tag{2.1}$$

where Y is the distance the vehicle traveled when the plume was measured during each plume event; T is total duration of the event; $C_m(\Delta A, t)$ is the 2-D mass concentration profile of PM_{10} or $PM_{2.5}$ in the plume at time, t, within the differential area ΔA (Figure 2.2(A)); $u(z)$ is the wind speed at the height z; and θ is the angle between the wind direction and the normal direction to the ORS observing plane during that event. Typical ranges of values for parameters in Eq. (2.1) are shown in Table 2.1. The integration of 2-D PM mass concentration profiles (Eq. (2.1)) was completed within the ORS observing plane using polar coordinates to define ΔA with a longitudinal resolution of 15 m and vertical dimension defined by the scanning angle and the respective radial distance (Figure 2.2(A)). Values of $C_m(\Delta A, t)$ profiles for PM_{10} or $PM_{2.5}$ were determined from the 2-D light extinction profiles, and PM_{10} or $PM_{2.5}$ MEE values using Eq. (2.2):

$$C_m\left(\Delta A, t\right) = \frac{\sigma\left(\Delta A, t\right)}{\mathrm{MEE}} \tag{2.2}$$

where $\sigma(\Delta A, t)$ represents a 2-D extinction profile.

Figure 2.1. Flow chart of method used to estimate mass emission factors for PM_{10} and $PM_{2.5}$ produced from the movement of vehicles on unpaved roads. Both MPL and OP-LT measure light extinction for total suspended particles (TSP), while DustTraks™ measure mass concentrations of PM_{10} or $PM_{2.5}$.

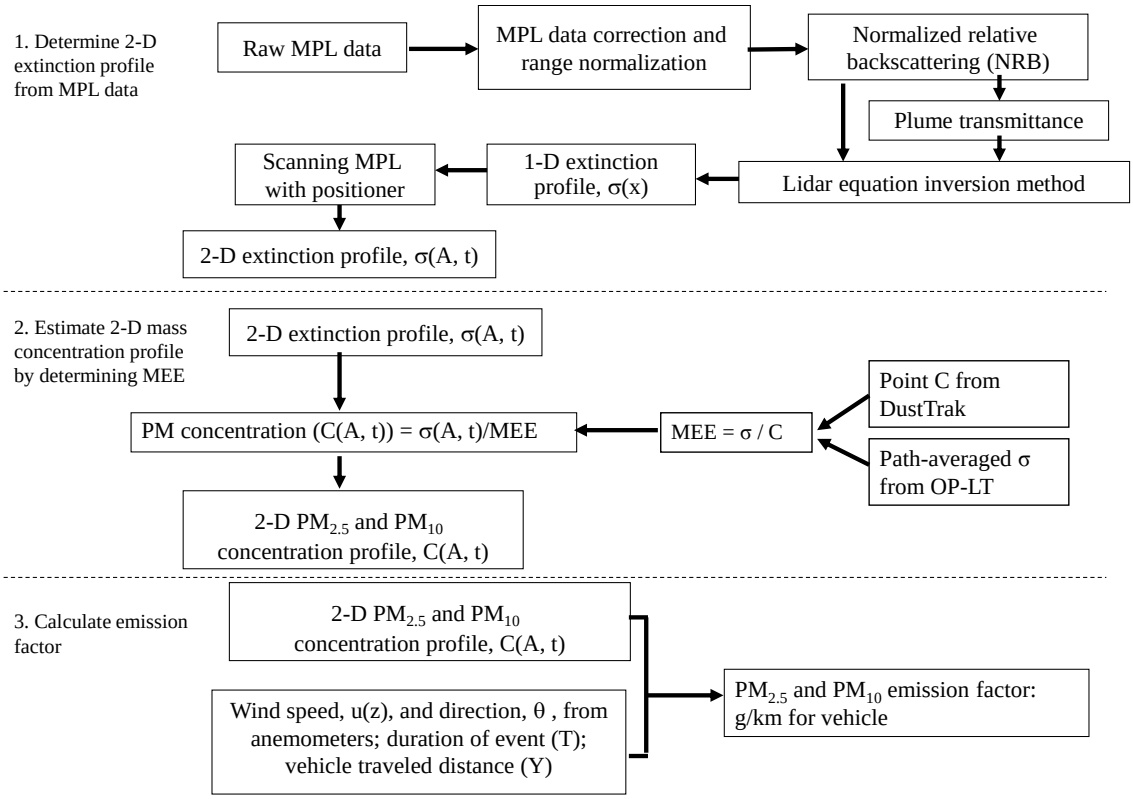

Figure 2.2. (A) Parameters in Eq. (2.1) – θ: wind angle from perpendicular to plume, Y: vehicle travelling distance, and ΔA: differential plume area, where ΔA center points are 15 m (MPL resolution) apart. All ΔAs define the ORS scanning plane (outermost dotted lines), which is parallel to the road. (B) Source and instrument layout during the field campaign.

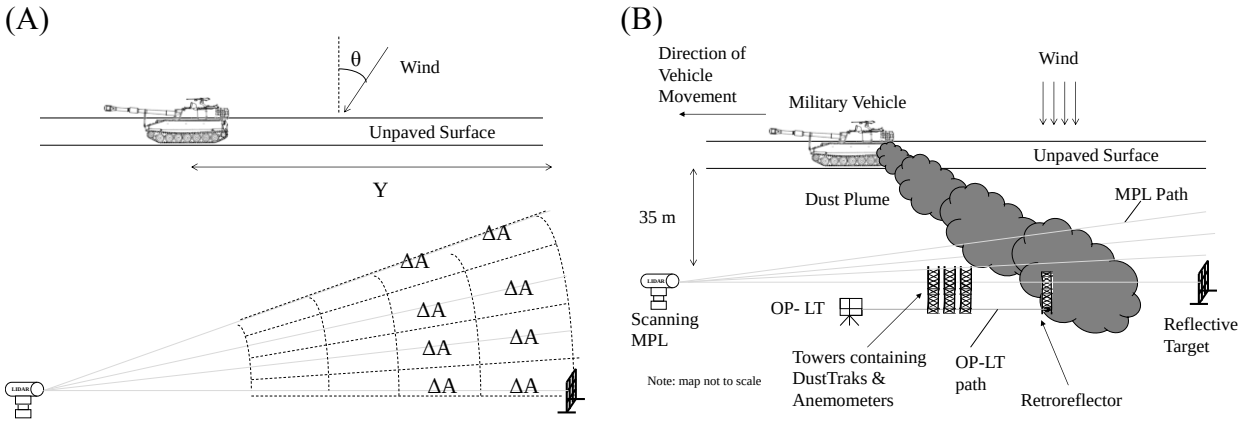

Table 2.1. Typical values in Eq. (2.1).

Parameter	**Range**
Vehicle travelling distance (Y, m)	Site 1: 258 to 341 Site 2: 172 to 270
Wind speed at 1.87 m height ($u_{1.87}$, m/s)	1 to 4
Wind direction (θ,°)	5 to 55 from the line normal to the observing plane
Duration of event (T, s)	40 to 90
Differential area for EF integration (ΔA, m^2)	10 to 461

The 2-D light extinction profiles were determined from the range-resolved backscattered photon counts measured by the Micro-Pulse Light Detection and Ranging (lidar; MPL) instrument (SigmaSpace, MPL-4B-527). To determine the 2-D light extinction profiles, the MPL was mounted on a vertically scanning positioner (ORBIT, Advanced Technologies, AL-4011-1E with control system AL-1613-3J) and pointed perpendicular to the plume's path while scanning vertically through the plume (Figure 2.2 (B)). The region scanned by the MPL defines the ORS observing plane (Figure 2.2 (A)). The photon counts were measured as pulsed laser light emitted from the MPL and then backscattered by the plume's PM toward the MPL's detector. The photon counts were corrected, normalized and then converted to normalized relative backscatter (NRB) values (Campbell et al., 2002). The MPL recorded photon counts at 1 Hz for the entire duration of each plume. To convert the 2-D NRB profiles to 2-D light extinction profiles the near-end lidar inversion technique was used (Du et al., 2011a; Fernald et al., 1972) with a reflective target that was located so that the plume was between the MPL and the target. The reflective target was used to calculate the calibration constant (K*) for MPL scans at the horizontal level, so that the light extinction profiles can be calculated at the horizontal level. To calculate the light extinction profiles at slanted angles, it is assumed that K* calculated at the horizontal level is the same as the K* at the slanted angles. With the K*, the corresponding light

extinction profiles at slanted angles can also be calculated using the near-end lidar inversion technique.

The MEE values for PM_{10} or $PM_{2.5}$ were determined from in-situ path-integrated total light extinction measurements divided by in-situ PM_{10} or $PM_{2.5}$ point mass concentration measurements, respectively. Light extinction was measured with a custom OP-LT (IMACC Inc.), at 1.7 m above ground that was co-located along the horizontal path of the MPL (Figure 2.2 (B)). The OP-LT used a modulated He-Ne laser operating at 1 Hz and transmitted light at 670 nm that was then reflected to the detector of the OP-LT by a custom retroreflector. These path-integrated light extinction values for the fugitive PM were determined by considering the signals detected by the OP-LT when a plume was and was not passing between the laser source and the retroreflector. PM_{10} and $PM_{2.5}$ mass concentrations were measured with calibrated light scattering DustTraks™ (Model 8520, TSI Inc.) at a rate of 1 Hz. The DustTraks™ were calibrated by comparing their light scattering measurements with gravimetric PM mass concentration measurements inside a dust resuspension chamber, for dust that was collected at the measurement site (Kuhns et al., 2010). The DustTraks™ were located on three vertical towers. One tower contained DustTraks™ at five different heights that measured both PM_{10} and $PM_{2.5}$. The other two towers contained DustTraks™ at five different heights that measured only PM_{10} (Kuhns et al., 2010). The average PM_{10} mass concentrations obtained at the lowest located DustTraks™ on all three towers and the $PM_{2.5}$ mass concentrations obtained at the lowest located DustTrak™ on one tower, all located at a height of 1.7 m, were used to calculate the PM_{10} and $PM_{2.5}$ MEE values, respectively. The lowest located DustTraks™ were used seeing they corresponded to the same height as the optical path of the OP-LT and they were co-located along the same path as the OP-LT, so the DustTraks™ and OP-LT sampled similar masses of PM.

MEE values were then determined by dividing the path-integrated and time-averaged total PM light extinction values from the OP-LT by the time-averaged PM_{10} or $PM_{2.5}$ mass concentrations measured by the DustTraks™, for the duration of each plume (Hashmonay et al., 2009). This method assumes that the averaged MEE values, describing the ratio of total PM light extinction to PM_{10} or $PM_{2.5}$ concentration, are representative of the PM plume within the scanning plane of the MPL during each emission event.

Use of the OP-LT required a wavelength correction in the MEE values because the OP-LT and MPL measurements occurred at 670 nm and 527 nm, respectively. The wavelength correction factor was determined by considering the PSD measured before, in a similar desert environment (Du et al., 2011a, 2011b; Varma et al., 2006) and was varied by changing the mean diameter by number, so $PM_{2.5}/PM_{10}$ was varied. Mie-Lorenz theory (Bohren and Huffman, 1983) was then used to calculate a wavelength correction factor for each selected PSD, assuming particles are spherical and a refractive index of 1.54+0i, a value that is representative of mineral dust. Based on values from Kandler et al. (2007), Petzold et al., (2009), Seinfeld et al. (2004), and Sokolik et al. (1993), the real part of refractive index ranges from 1.53 to 1.59, and imaginary part ranges from $0.3x10^{-3}$ to $9.0x10^{-3}$ for mineral dust. It was observed that the wavelength correction factor was linearly related to $PM_{2.5}/PM_{10}$. Linear regression resulted in the following wavelength correction factor $\sigma_{ext_{527}}/\sigma_{ext_{670}} = 0.74*(PM_{2.5}/PM_{10})+0.68$, $R^2 = 0.97$ for six data points, that was used to convert the extinction coefficient at 670 nm ($\sigma_{ext_{670}}$) to the extinction coefficient at 527 nm ($\sigma_{ext_{527}}$), which was used to calculate the MEE values. These MEE values of PM_{10} and $PM_{2.5}$ were combined with the MPL extinction coefficient measurements to obtain 2-D mass concentration profiles of PM_{10} and $PM_{2.5}$.

Wind speeds were determined with 2-D cup anemometers (Wind Sentry, R. M. Young) measured at five elevations (1.87, 2.80, 4.20, 6.65, and 9.34 m) and wind direction was determined with a wind vane placed at 9.34 m (Wind Sentry, R. M. Young). The anemometers and wind vane were co-located on the three towers with the DustTraks™. Power law regressions were fitted to the measured wind speed values to determine wind speed at the heights of the light extinction measurements (USEPA, 2000). Wind direction was treated as a constant vertically for each plume event. Duration of each plume event was determined by the amount of time the plume passed through the vertical measurement plane detected by the MPL. The duration of a sampling event begins when the MPL first detects non-zero light extinction at the ground level scan. The duration ends when the MPL no longer detects non-zero light extinction at the ground level scan.

Field Site and Vehicle Information

The hybrid-ORS method was implemented during September 2008 at a desert continental site located at Fort Carson, CO, USA. The three types of tracked vehicles tested and their masses are: M88 (HERCULES, 63.5 tonne), M270 (MLRS, 24.9 tonne), and M577 (12.3 tonne). A wheeled vehicle, Heavy Expanded Mobility Tactical Truck (HEMTT, 20.0 tonne), was also tested. These vehicles traveled along unpaved roads parallel to the measurement plane and perpendicular to wind direction. Each vehicle travelled at speeds between 8 and 32 km/hr and at their maximum speed. A Global Positioning System (GPS) was placed in the vehicles to monitor vehicle position and speed.

Two unpaved roads were selected for the measurements to accommodate changes in wind direction during the field campaign. The optical paths of the ORS instruments were parallel to and 35 m downwind from either road (Figure 2.2(B)). The setback distance between the MPL and the OP-LT was 185 m for Site 1 and 105 m for Site 2. The distance between the MPL and

the MPL's reflective target was 790 m for Site 1 and 445 m for Site 2 to ensure the detected plumes were between the MPL and reflective target during each plume event. The MPL continuously scanned at Site 1 at angles: 0° (horizontal), 1.519°, 3.036°, and 4.045°, or 0°, 2.025°, 4.045°, and 6.054° depending on the plume elevations. The MPL continuously scanned at Site 2 at angles: 0°, 4.588°, 9.119°, and 12.080°. The duration of a vertical scan cycle was 10 – 14 s and the duration of plumes passing through the measurement plane of the MPL was between 40 s and 90 s, which resulted in three to nine 2-D extinction profiles per plume event.

The soil type at Site 1 and Site 2 was Heldt clay loam and Razor-Midway complex clayloam, respectively (Kuhns et al., 2010). Soil moisture content was assumed to be 1%, consistent with dry weather during the campaign and previous research at desert sites where moisture content was < 1% (Kuhns et al., 2010). These values were used as inputs for the AP-42 EF models (USEPA, 2015a) to compare the AP-42 results with the measured values.

Quality Control Procedures in Data Analysis

Quality control procedures were performed to remove invalid data. A plume event was removed if any data (e.g., vehicle speed, MEE, and wind data) were missing. Plume events were also removed if any one of the following conditions occurs:

1) the wind did not direct the plume to the MPL's scanning plane due to sudden wind direction change (i.e., $\theta > 55°$) or low wind speed (i.e., < 1.0 m/s). Large θ or low wind speed will cause the plume to not travel through the MPL's scanning plane, thus the MPL does not capture the entire cross-section of the plume horizontally.

2) the largest angle of vertical scan was not high enough to capture the highest part of the plume. These were cases when non-zero light extinction was detected at the largest angle of vertical scan, indicating that the plume extended above the highest level the MPL could capture.

3) the MPL measured zero backscatter signals from the reflective target. This means that the plume is too opaque (< 1% light transmittance). High opacity results in high uncertainty in determining the light extinction profile.

Data Analysis

Results from the hybrid-ORS measurements were compared with those from the flux tower measurements reported by Kuhns et al. (2010) and estimated using AP-42 EFs. Mean Percentage Differences (MPDs) between the hybrid-ORS results and results from the flux tower method or AP-42 model for each vehicle were estimated by Eq. (2.3):

$$\text{MPD} = \frac{1}{N}\sum_{i=1}^{N}\frac{\text{EF}_{\text{alt,i}} - \text{EF}_{\text{hORS,i}}}{\text{EF}_{\text{hORS,i}}} \times 100\% \qquad (2.3)$$

In Eq. (2.3), EF_{alt} is the EF determined by a method/model alternative to the hybrid-ORS method (i.e., flux tower method or AP-42 model), EF_{hORS} is the EF determined by the hybrid-ORS method, *i* refers to the EF data point at a select vehicle type and speed, and *N* refers to total number of vehicle speeds tested for a particular vehicle. EFs determined by the flux tower method were linearly interpolated to the average vehicle speeds used with the hybrid-ORS method to allow comparison of EFs from the two methods, at the same vehicle speed range.

AP-42 model uses Eqs. (1.11) and (1.12) for industrial roads and publicly accessible roads, respectively (USEPA, 2015a):

$$\text{EF} = 281.9k\left(S/12\right)^{0.9}\left(W/3\right)^{0.45} \text{ (g-PM/km)} \qquad (1.11)$$

$$\text{EF} = 281.9\left[k'\left(S/12\right)\left(V/30\right)^{0.5}\left(m/0.5\right)^{-0.2} - C\right] \text{ (g-PM/km)} \qquad (1.12)$$

where $k = 0.15$ for $\text{PM}_{2.5}$ and $k = 1.5$ for PM_{10}, S is silt content (32%, Kuhns et al., 2010), W is mean vehicle mass (tonne), $k' = 0.18$ for $\text{PM}_{2.5}$ and $k' = 1.8$ for PM_{10}, V is mean vehicle speed (km/hr), m is surface soil moisture content (% by mass), and C is PM mass EF due to vehicle

exhaust, brake wear, and tire wear (g/km) (USEPA, 2015a). *C* is negligible compared to the fugitive PM emissions (< 1% of fugitive PM emissions, USEPA, 2011). Note that the AP-42 model for industrial roads does not include vehicle speed but includes vehicle mass as a parameter, while the model for publicly accessible roads includes vehicle speed but does not include vehicle mass as a parameter. Moreover, the model for industrial roads applies to vehicles ranging from 1.8 to 260 tonnes and from 8 to 69 km/hr, while the model for publicly accessible roads applies to vehicles ranging from 1.4 to 2.7 tonnes and 16 to 88 km/hr. While the vehicle speeds used with the hybrid-ORS measurements were within the range of the speeds used for both models and the vehicle masses were within the range of the masses used for the industrial road model, the vehicle masses were between 4 and 23 times larger than the range of masses used for the publicly accessible road model. Both AP-42 models also only consider vehicles that have four or more wheels (USEPA, 2015a). However, three out of four vehicles used in this research are tracked vehicles. For the above reasons, discrepancies between results from the hybrid-ORS method and AP-42 models may exist.

2.4 Results and Discussion

A series of the resulting 2-D PM_{10} mass concentration profiles is shown in Figure 2.3 to provide graphical insight about the length and time scales of a fugitive PM event caused by a HEMTT vehicle traveling at 24 km/hr on an unpaved road. EF statistics for PM_{10} and $PM_{2.5}$ determined by the hybrid-ORS method versus vehicle speed are presented in Figure 2.4 and 2.5, respectively. The EF data were first classified into vehicle speed ranges. The means and standard deviations of EF data within the same speed range were then calculated and plotted as data points and vertical lines, respectively. The EFs for tracked vehicles ranged from 206 g/km to 1,738 g/km for PM_{10} and from 78 g/km to 684 g/km for $PM_{2.5}$, depending on vehicle speed and vehicle

type. The EFs for the wheeled vehicle ranged from 223 g/km to 4,339 g/km for PM_{10} and from 44 g/km to 1,627 g/km for $PM_{2.5}$.

Figure 2.3. Example of evolution of PM_{10} mass concentration profiles when a HEMTT vehicle passed at the speed of 24 km/hr, as it moves along a line parallel to the MPL observation plane and towards the MPL. The time elapsed between two consecutive profiles is 14 s.

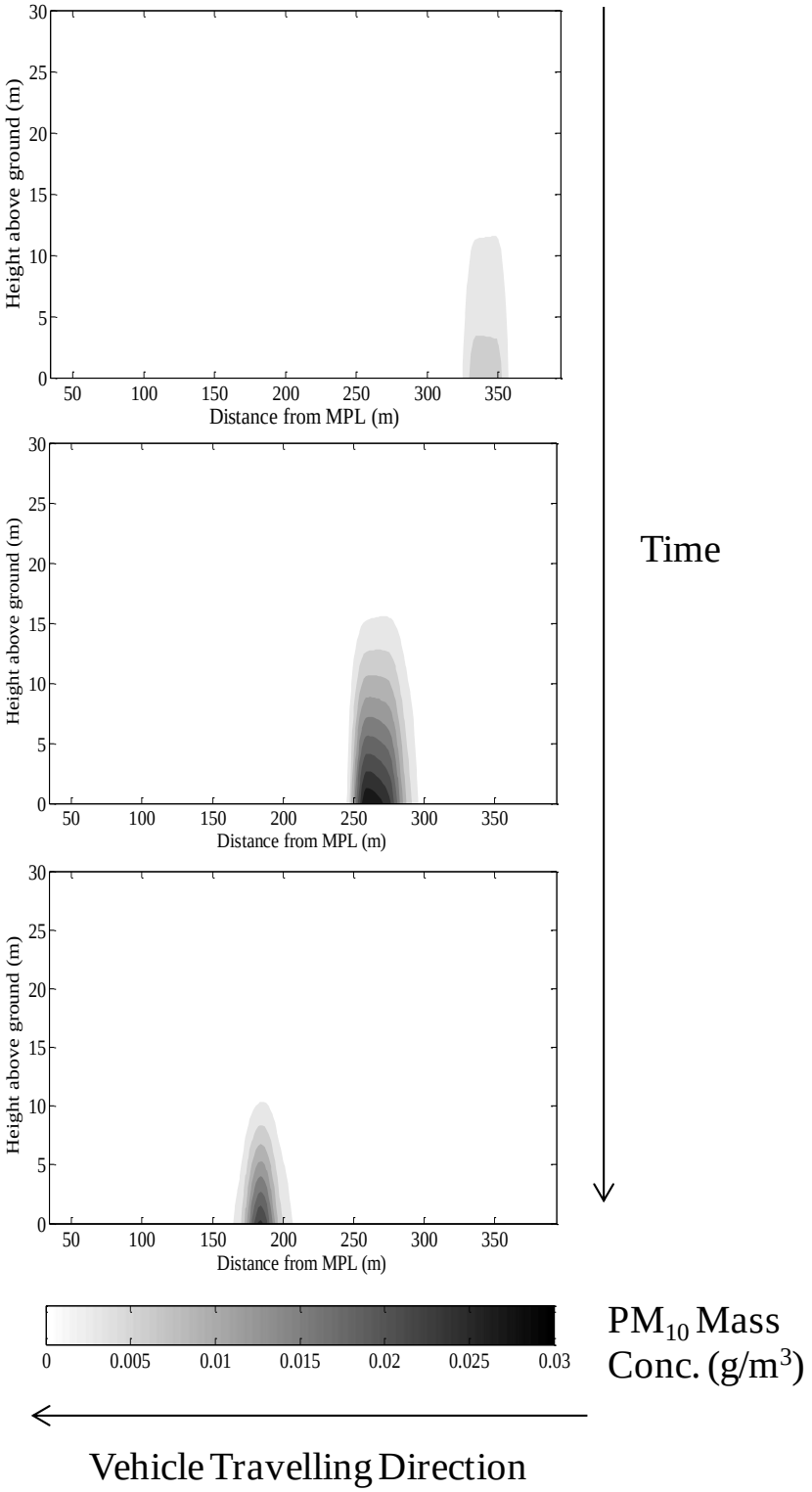

Figure 2.4. Comparison of measured PM_{10} mass emission factors by hybrid-ORS and flux tower methods (Kuhns *et al.*, 2010) and modeled PM_{10} emission factors from AP-42 industrial road model and publicly accessible road model.

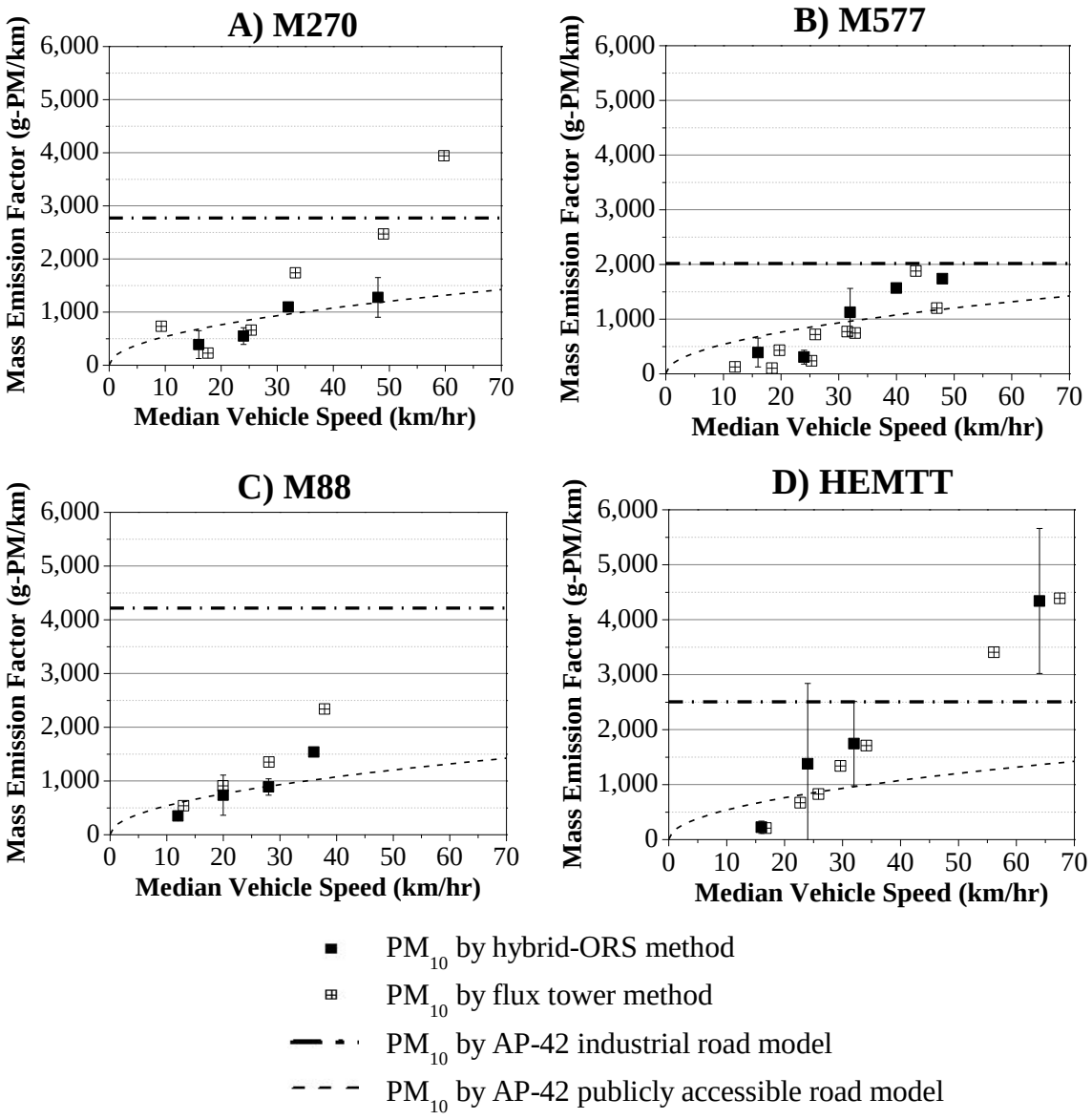

Figure 2.5. Comparison of measured $PM_{2.5}$ mass emission factors by hybrid-ORS method and modeled emission factors from AP-42 industrial road and publicly accessible road models.

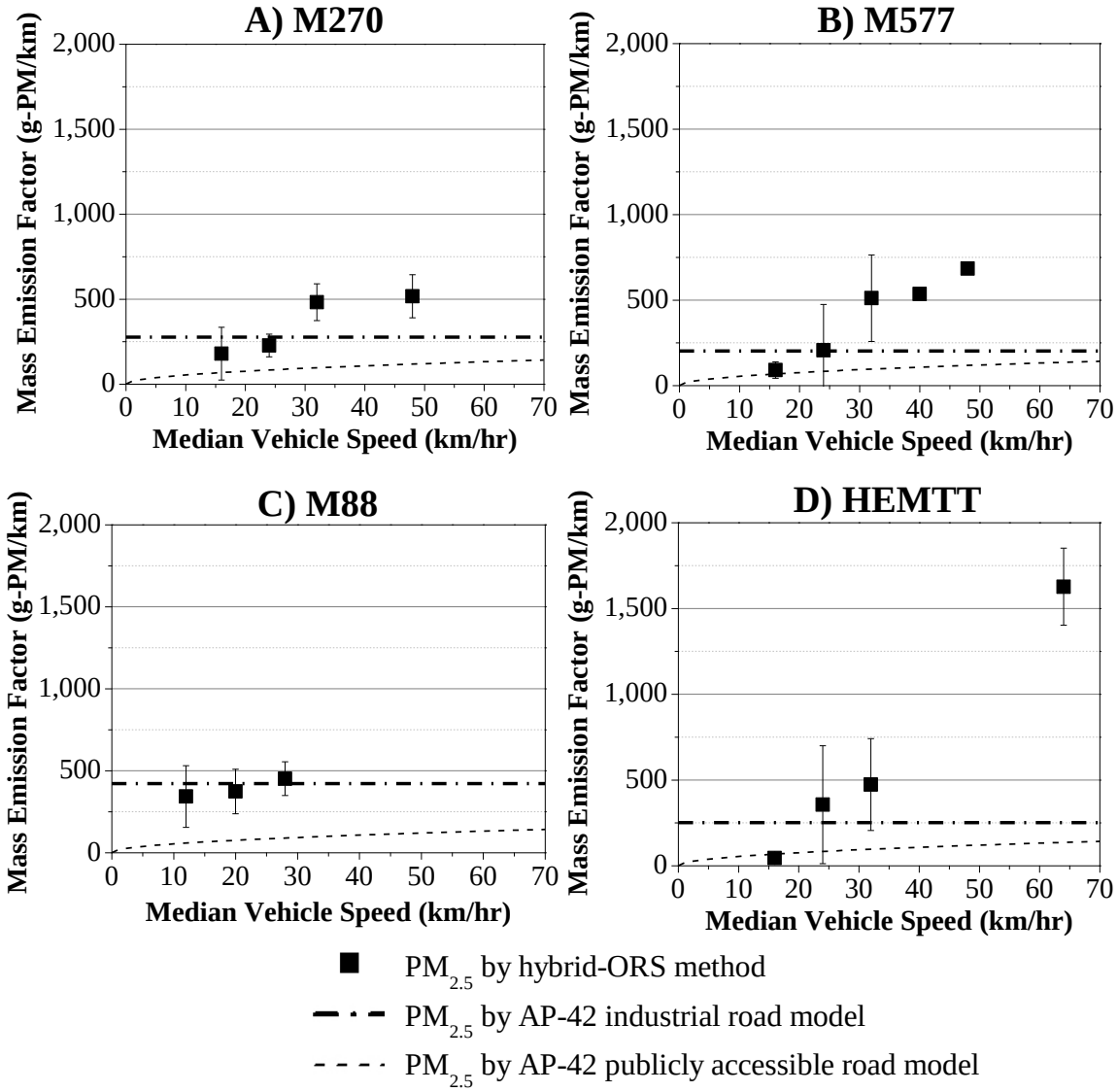

Linear, quadratic, and power law regressions were completed to fit the data for each vehicle type. The power law regression resulted in the largest mean correlation coefficients (R^2). AP-42 models also fit parameters using the power law (USEPA, 2015a), thus comparison of results from the hybrid-ORS and from AP-42 is facilitated by using the same model. Power law regressions of PM EFs obtained with the hybrid-ORS method are provided as a function of vehicle type and speed in Table 2.2.

Table 2.2. Power law regressions of PM mass emission factors as a function of speed for select vehicles.

Vehicle (traction)	Particle size range	Regression [a]	R^2	Number of tested speeds	Number of events
M270 (tracked)	PM_{10}	$EF = 15v^{1.17}$	0.92	4	13
	$PM_{2.5}$	$EF = 9v^{1.07}$	0.87		
M577 (tracked)	PM_{10}	$EF = 2.87\ v^{1.66}$	0.79	5	21
	$PM_{2.5}$	$EF = 0.51v^{1.90}$	0.95		
M88 (tracked)	PM_{10}	$EF = 15v^{1.28}$	0.97	4	14
	$PM_{2.5}$	$EF = 155v^{0.31}$	0.89		
HEMTT (wheeled)	PM_{10}	$EF = 1.49v^{1.98}$	0.86	4	15
	$PM_{2.5}$	$EF = 0.09v^{2.42}$	0.89		

[a] EF = PM mass emission factor (g/km), v = vehicle speed (km/hr)

For both PM_{10} and $PM_{2.5}$, we compared normalized EFs versus vehicle speed for four vehicles measured in this field campaign to facilitate comparison of results with Gillies *et al.* (2005). To obtain normalized EFs, the ratios of EFs at select speeds to the EF at maximum speed are calculated for each vehicle (Figure 2.6). Linear fits were forced through the origin. A t-test was also performed to examine if the slopes for tracked and wheeled vehicles are significantly different (sample sizes and t-test results are shown in Table 2.3). R^2 values for the linear regressions of the normalized PM_{10} EFs versus vehicle speed are larger than the normalized $PM_{2.5}$ EFs versus vehicle speed, especially for tracked vehicles. The slopes of the linear fits for the wheeled vehicle's normalized PM_{10} EFs versus vehicle speed support the result by Gillies *et al.* (2005), where results by both us and Gillies *et al.* are 0.014. The t-test shows that the slopes for tracked and wheeled vehicles are not significantly different from each other at 95% confidence level for both PM_{10} and $PM_{2.5}$ (p-values > 0.94 > 0.05).

Figure 2.6. Linear regression plots of (a) PM_{10} and (b) $PM_{2.5}$ normalized EFs (unitless) against vehicle speeds (km/hr) for the four vehicles measured in our field campaign. Normalized EF is defined as the ratio of EF at a specified vehicle speed to EF measured at the maximum speed for each vehicle.

(a) (b)

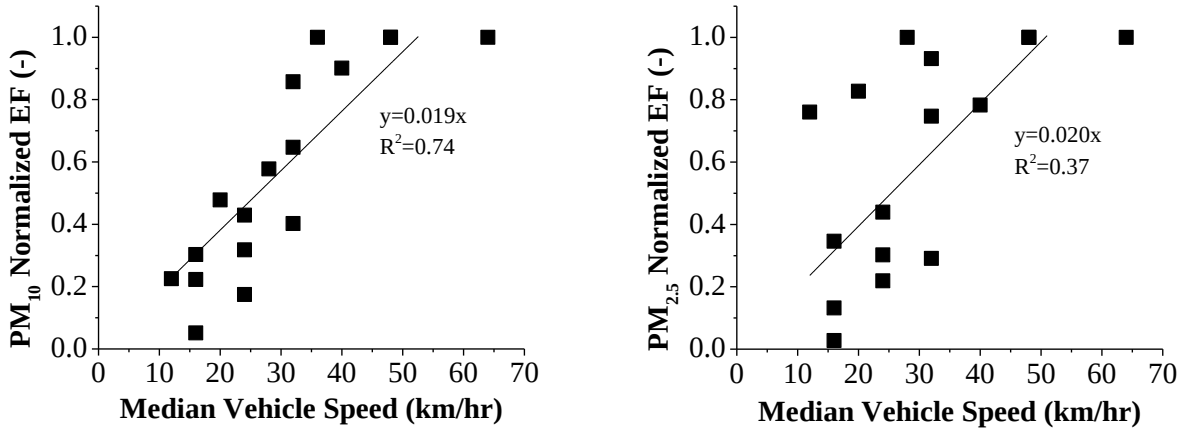

Table 2.3. Linear regression statistics of PM_{10} and $PM_{2.5}$ normalized EFs against vehicle speeds. Zero intercept was set for the linear regressions. Normalized EFs are the ratio of the EF to the EF at maximum speed for each vehicle. The p-values indicate that there is no significant difference between the slopes of tracked and wheeled vehicles for PM_{10} and $PM_{2.5}$ at 95% confidence level.

Vehicle Type	Normalized PM_{10} EF (-)			Normalized $PM_{2.5}$ EF (-)		
	Slope	R^2	Number of data	Slope	R^2	Number of data
Four vehicles combined [a]	0.019	0.74	16	0.020	0.37	15
Three tracked vehicles	0.021	0.81	12	0.023	0.31	11
One wheeled vehicle	0.014	0.91	4	0.013	0.84	4
p-value	0.94			0.95		
Nine wheeled vehicles [b]	0.014	0.77	36			

[a] Four vehicles are: M270 (tracked), M577 (tracked), M88 (tracked), and HEMTT (wheeled)
[b] Nine wheeled vehicles are: Dodge Neon, Dodge Caravan, Ford Taurus, GMC G20 van, HMMWV, GMC C5500, HEMTT, M923A2, and M1078 LMTV (Gillies et al., 2005)

The relationship between the slope of PM_{10} and $PM_{2.5}$ EF versus vehicle speed [(g/km)/(km/hr)] and the vehicle's mass (kg) were also examined and shown in Figure 2.7. To obtain the slope of PM EF versus vehicle speed, linear regression between each vehicle's PM EF versus speed is obtained. The slopes of PM_{10} EF versus vehicle speed from Gillies *et al.* (2005)

are also added in Figure 2.7 for comparison. Our results show that the slopes of PM_{10} and $PM_{2.5}$ EF versus vehicle speed are independent of vehicle masses for tracked vehicles. Linear regression significance tests of the results from the hybrid-ORS method show that p-values for PM_{10} and $PM_{2.5}$ are 0.57 and 0.31, respectively, for the three tracked vehicles. Hence, there is not a statistically significant linear relationship between the slopes of PM EF versus vehicle speed and the vehicle masses at 95% confidence level. These results are in contrast to the results by Gillies *et al.* (2005), where a strong linear relationship for wheeled vehicles was observed, with slope of PM EF versus vehicle speed [(g/km)/(kg km/hr)] = 3*vehicle masses (tonne), $R^2 = 0.95$, for nine vehicles with masses between 1 and 18 tonnes. A possible explanation is that there may be an upper limit of road surface material that is available for resuspension, so further increase in vehicle mass does not necessarily increase the PM EF per unit speed. Our tested vehicles have larger masses than vehicles tested in Gillies *et al.* (2005), so it is possible that vehicles tested in Gillies *et al.* (2005) do not resuspend the maximum amount of road surface material, thus explaining the linear relationship reported by Gillies *et al.* (2005). The slope of PM_{10} EF of HEMTT versus speed is 62.2 (g/km)/(km/hr), while the slope of the same vehicle by Gillies *et al.* (2005) is 50 (g/km)/(km/hr).

Figure 2.7. Relationship between the slope of PM EF versus vehicle speed ((g/km)/(km/hr)) and vehicle mass (kg). Our data have three data points representing three tracked vehicles. Gillies *et al.* (2005) data have nine data points representing nine wheeled vehicles.

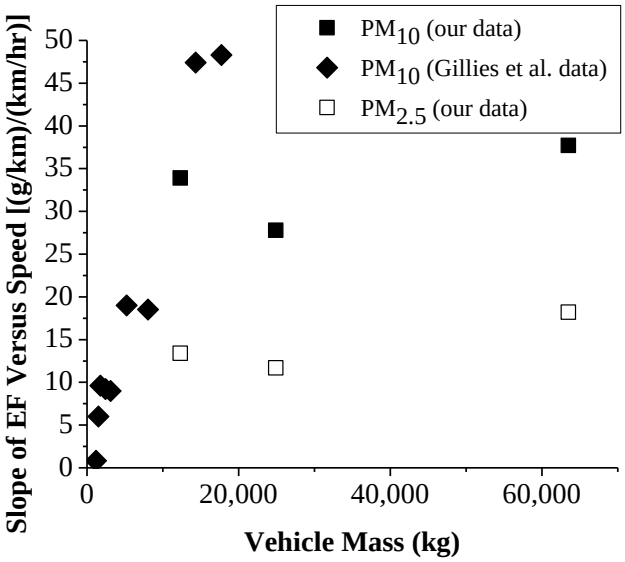

Comparison of Results from Hybrid-ORS Method to Concurrent Flux Tower Method

Results from the hybrid-ORS and flux tower methods are compared and the results of EF versus vehicle speed are shown in Figure 2.4 for PM_{10} and in Figure 2.5 for $PM_{2.5}$. MPD values for EFs from hybrid-ORS and flux tower EFs for all four vehicles are shown in Table 2.4, which range from -25% to 40% for PM_{10}. There are no variances reported from the flux tower method to statistically test the difference between the hybrid-ORS and flux tower methods. EFs for $PM_{2.5}$ from the flux tower method are not available.

Table 2.4. Mean Percentage Differences (MPD) between hybrid-ORS emission factor results to corresponding results from the flux tower and AP-42 results for industrial roads and publicly accessible roads for each vehicle type. Flux tower measurements for $PM_{2.5}$ are unavailable.

Site location and vehicle type		Flux tower measurement	AP-42 emission factor model for industrial road		AP-42 emission factor model for publicly accessible road	
Site no.	**Vehicle type**	**MPD[a] for PM_{10} (%)**	**MPD[a] for PM_{10} (%)**	**MPD[a] for $PM_{2.5}$ (%)**	**MPD[a] for PM_{10} (%)**	**MPD[a] for $PM_{2.5}$ (%)**
1	M270	31	324	-3	27	-71
1	M88	40	535	10	10	-81
2	M577	-22	222	-14	34	-66
2	HEMTT	-25	277	76	13	-49

[a] MPD = mean percent difference (Eq. (2.3))

In addition, results from the hybrid-ORS and flux tower methods for PM_{10} EF versus tracked vehicle momentum are compared and shown in Figure 2.8. Kuhns *et al.* (2010) calculated the mean ratios of PM_{10} EF to vehicle momentum for tracked and wheeled vehicles at each site. We performed similar calculations and compared our results to Kuhns *et al.* (2010) in Table 2.5. The 95% confidence intervals for our results and Kuhns *et al.* results were also compared. For tracked vehicles, the confidence intervals for both data sets did not overlap, meaning that the differences between these data sets are significant at 95% confidence level. The mean ratio of our data (0.004 (g PM_{10}/km)/(kg m/s)) is smaller than the mean ratio of data from Kuhns *et al.* (0.006 (g PM_{10}/km)/(kg m/s)) at Site 1, and larger (0.009 (g PM_{10}/km)/(kg m/s)) than data from Kuhns *et al.* (0.004 (g PM_{10}/km)/(kg m/s)) at Site 2. For wheeled vehicles, the confidence intervals overlapped, meaning that the differences between the data sets are insignificant at 95% confidence.

Figure 2.8. Comparison of hybrid-ORS and flux tower PM_{10} mass emission factors versus vehicle momentum for tracked vehicles.

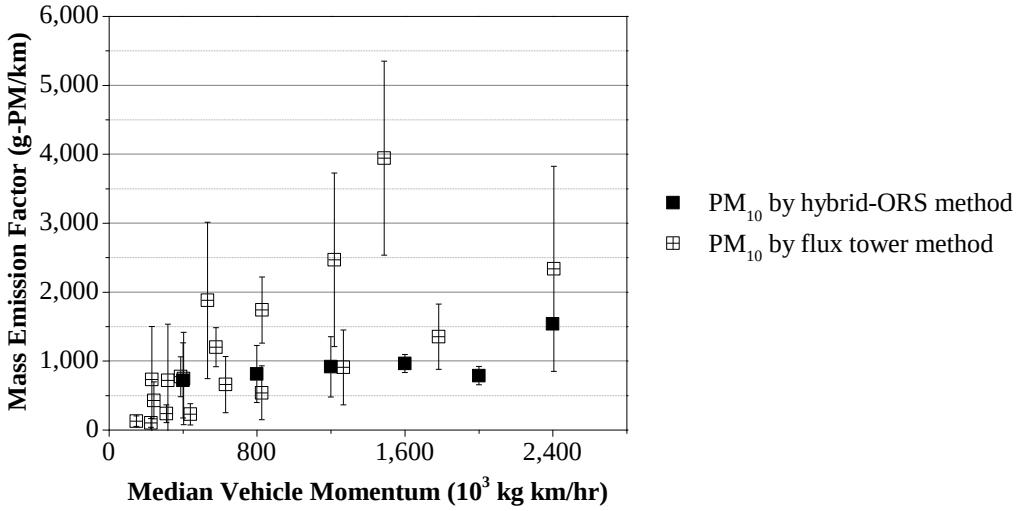

Table 2.5. Comparison of PM_{10} EFs that are normalized to their momentum for tracked and wheeled vehicles between our data and Kuhns *et al.* (2010) data. Values are presented as the ratios ± uncertainty, which are standard deviations. Numbers in parentheses represent number of samples. Numbers in brackets show the corresponding 95% confidence intervals.

	PM_{10} EF/ vehicle momentum [(g PM_{10}/km)/(kg m/s)]	
	Our data	**Kuhns *et al.*, 2010**
Site 1 Tracked	0.004±0.003 (38) [0.003, 0.005]	0.006±0.002 (157) [0.006, 0.006]
Site 2 Tracked	0.009±0.004 (9) [0.007, 0.012]	0.004±0.004 (34) [0.003, 0.005]
Site 2 Wheeled	0.009±0.007 (15) [0.005, 0.013]	0.008±0.003 (52) [0.007, 0.009]

From the above results, there is no strong evidence to support whether the flux tower EFs are generally larger or smaller than hybrid-ORS EFs. The two methods have inherent differences. The flux tower method provides PM mass concentrations measured with the light scattering based DustTraks™ that are mounted on towers to detect the cross-sections of the plumes. The hybrid-ORS method detects PM mass concentration by inferring light extinction measured by an MPL range-resolved laser beam that scans the plumes' vertical cross-sections. The time resolution of the DustTraks™ used with the flux tower method and the hybrid-ORS is 1 Hz, whereas it takes 10 – 14 s for the ORS to complete a vertical scan. Moreover, ORS requires a

longer setback distance from the area of measurement to measure taller plumes, which increases the area required to perform the ORS measurements. The ORS also requires a downwind distance so that the plume can disperse to the ORS scanning plane, but such distance introduces particle loss due to deposition. Such particle loss is believed to be insignificant. An earlier field campaign showed that PM_{10} loss is not measurable at a downwind distance of 100 m. Such results have also been compared with ISC3 model that only 4.3% of PM_{10} is removed at a downwind distance of 100 m (Etyemezian *et al.*, 2004). Both methods have been shown applicable for the measurement of fugitive PM emissions factors. Further validation and method uncertainty quantification can be achieved under controlled environmental conditions (such as choosing a location with low variations of wind speed and direction during the experiment) and with use of known emissions (such as by means of using a high volume dust generator). Such experiments in the ambient are rare due to cost considerations but they are valuable for future implementation of novel measurement methods.

Comparison of Results from Hybrid-ORS Method to AP-42 Model

PM_{10} and $PM_{2.5}$ EFs determined by the hybrid-ORS method were also compared with results from the AP-42 EFs for vehicles traveling on unpaved industrial and publicly accessible roads (Figures 2.4 and 2.5 for PM_{10} and $PM_{2.5}$, respectively). Since AP-42 industrial road model is independent of vehicle speed (Eq. (2.4)), the lines for this model are horizontal. AP-42 publicly accessible road model, however, depends on vehicle speed (Eq. (2.5)), so the lines for this model are curved. MPDs between hybrid-ORS results and AP-42 industrial and publicly accessible roads modeled values for each vehicle are shown in Table 2.4. The MPDs between the EFs estimated by the hybrid-ORS method and those modeled by AP-42 for industrial roads for all test conditions range from 222% to 535% for PM_{10}, and from -14% to 76% for $PM_{2.5}$. The MPDs between EFs measured by the hybrid-ORS method and modeled by AP-42 for publicly

accessible roads for all test conditions range from 10% to 34% for PM_{10} and from -81% to -49% for $PM_{2.5}$.

MPD values show that PM_{10} EFs provided by the AP-42 model for the industrial road were generally larger than EFs derived from the hybrid-ORS method. A similar trend was also reported regarding comparison between the flux tower method and the AP-42 model (Gillies *et al.*, 2005; Kuhns *et al*., 2010). The AP-42 model for publicly accessible road tends to underestimate $PM_{2.5}$ EFs when compared to the hybrid-ORS method. The underestimations may result because the masses of the tested vehicles during this field campaign were between 4 and 23 times higher than the upper mass limit for which the AP-42 model for publicly accessible road should be applied. This puts into perspective the high uncertainty associated with the existing AP-42 EFs, and indicates that possibly silt content and surface soil moisture in the current AP-42 EF equations do not fully capture the variability of PM EFs generated from vehicles travelling on unpaved surfaces.

Sensitivity Analysis of Wavelength Corrections of MEE Values Due to Particle Properties

The PM_{10} and $PM_{2.5}$ MEE values measured for the vehicles travelling on unpaved roads are shown in Table 2.6. The PM_{10} MEE values are within the range of the values in literature discussed in Section 1.2, which is from 0.5 to 5.9 m^2/g.

Table 2.6. MEE values for vehicle travelling on unpaved road.

Quantity	PM_{10}		$PM_{2.5}$	
	Mean	**Standard Deviation**	**Mean**	**Standard Deviation**
MEE (m^2/g)	2.1	1.1	7.2	7.1

A sensitivity analysis was performed to examine the influence of refractive index and PSD on the wavelength corrections of MEE values. As the base case, we used refractive indices

of 1.53-4.2x10^{-3}i for 527 nm (MPL) and 1.53-6.6x10^{-3}i for 670 nm (OP-LT) (Hess et al., 1998), PSD based on number concentrations (geometric mean diameter = 0.6 μm and geometric standard deviation = 1.8), and particle density of 2.6 g/cm^3 for mineral dust (Hess et al., 1998) to calculate the PM_{10} and $PM_{2.5}$ MEEs for both wavelengths. As mentioned above, the real part of refractive index ranges from 1.53 to 1.59, and imaginary part ranges from 0.3x10^{-3} to 9.0x10^{-3} for mineral dust. A previous sensitivity analysis studied MEE values when the real and imaginary parts of the refractive index were varied from 1.35 to 1.60 and 0 to 0.01, respectively, and observed that MEE values ranged from 0.33 to 0.35 m^2/g (percent difference < 6%) (Du, 2007). Realizing that the imaginary part of the refractive index does not change MEE values substantially, MEE calculations in this sensitivity analysis were repeated by using only the real part of the refractive index values of 1.50, 1.53, and 1.60. PSDs were also varied by changing the mean number-based particle diameter from 0.4 to 0.7 μm and geometric standard deviation from 1.75 to 1.90. The chosen ranges are based on PSD data of desert dust obtained during a field campaign in Yuma, AZ (Du et al., 2011b). Particle diameter was integrated from 0.05 μm to 40 μm to calculate total PM extinction coefficients with the use of Mie-Lorenz Theory, and was integrated from 0.05 μm to 10 μm or from 0.05 μm to 2.5 μm to calculate PM_{10} or $PM_{2.5}$ mass concentration, respectively. MEE values at MPL and OP-LT wavelengths were then calculated from the total PM extinction coefficients and PM_{10} or $PM_{2.5}$ mass concentration. The wavelength correction factor was calculated by taking the ratios of OP-LT to MPL derived MEE values.

The wavelength correction factors are between 0.971 and 1.081 for the ranges of PSDs and refractive indices evaluated (Table 2.7). By varying the geometric mean diameters and standard deviations of PSDs from the base case, the wavelength correction factor varied < 5%. Therefore, the correction in MEE values due to wavelength difference between the OP-LT and

MPL is not sensitive to either PSD or real refractive index for conditions experienced during the field campaign.

Table 2.7. Sensitivity analysis of mass extinction efficiency (MEE) correction factors, described by the ratio of MEE values at red (670 nm) to green (527 nm) wavelengths, for three real parts of the refractive indices. In table a) the geometric standard deviation (GSD) is 1.8 and the mean diameters range from 0.4 to 0.7 μm. In table b) the mean diameter is 0.5 μm and the GSDs range from 1.75 to 1.90.

a) Geometric standard deviation = 1.8

Real part of refractive index	**Mean diameter (μm)**							
	0.4		0.5		0.6		0.7	
	MEE red to green wavelength correction factor for $PM_{2.5}$ or PM_{10}							
	$PM_{2.5}$	**PM_{10}**	**$PM_{2.5}$**	**PM_{10}**	**$PM_{2.5}$**	**PM_{10}**	**$PM_{2.5}$**	**PM_{10}**
1.50	0.971	0.972	1.022	1.021	1.051	1.051	1.066	1.066
1.53	0.988	0.988	1.036	1.037	1.065	1.065	1.081	1.080
1.60	1.005	1.004	1.038	1.037	1.050	1.050	1.050	1.050

b) Mean diameter = 0.5 μm

Real part of refractive index	**Geometric standard deviation**							
	1.75		1.80		1.85		1.90	
	MEE red to green wavelength correction factor for $PM_{2.5}$ or PM_{10}							
	$PM_{2.5}$	**PM_{10}**	**$PM_{2.5}$**	**PM_{10}**	**$PM_{2.5}$**	**PM_{10}**	**$PM_{2.5}$**	**PM_{10}**
1.50	1.015	1.015	1.022	1.021	1.027	1.027	1.031	1.031
1.53	1.031	1.031	1.036	1.037	1.042	1.042	1.047	1.046
1.60	1.039	1.038	1.038	1.037	1.037	1.037	1.035	1.036

2.5 Conclusions

Emission Factors (EFs) for fugitive PM_{10} and $PM_{2.5}$ emitted by vehicles travelling on desert unpaved roads were measured using a hybrid-optical remote sensing (ORS) method. This ORS method uses a micro-pulse lidar (MPL) to obtain vertically scanned 2-D extinction profiles. These extinction profiles were combined with mass extinction efficiency (MEE) values obtained from point PM_{10} and $PM_{2.5}$ mass concentrations and path-integrated open path-laser transmissometer (OP-LT) measurements to determine 2-D PM_{10} and $PM_{2.5}$ mass concentration profiles across each plume. EFs for fugitive PM_{10} and $PM_{2.5}$ were obtained by integrating 2-D mass concentration profiles with wind data and duration of each event. The EFs for tracked

vehicles ranged from 206 g/km to 1,738 g/km for PM_{10} and from 78 g/km to 684 g/km for $PM_{2.5}$, depending on vehicle speed and vehicle type. The EFs for the wheeled vehicle ranged from 223 g/km to 4,339 g/km for PM_{10} and from 44 g/km to 1,627 g/km for $PM_{2.5.}$ These PM EF results may be used by facilities to determine the impact of the operation of these vehicles on air quality impacted by fugitive dust.

EFs measured by hybrid-ORS method were compared with concurrent measurements of EFs using the flux tower method and EFs estimates by USEPA AP-42 models. Mean percent differences (MPDs) between -25% and 40% were observed between the hybrid-ORS and flux tower methods for PM_{10}, which shows that there is no strong evidence to support whether the flux tower EFs are generally larger or smaller than hybrid-ORS EFs. Comparisons with AP-42 PM_{10} EFs resulted in MPD values between 222% and 535% for the industrial road case and between 10% and 34% for the publicly accessible road case. For $PM_{2.5}$, MPD values ranged between -14% and 76% for the AP-42 industrial road case and between -81% and -49% for the publicly accessible road case. These comparisons between hybrid-ORS and AP-42 EFs show that PM_{10} EFs estimated by the AP-42 model for industrial road were generally larger than EFs derived from the hybrid-ORS method. $PM_{2.5}$ EFs estimated by the AP-42 model for publicly accessible roads were generally smaller than EFs derived from the hybrid-ORS method.

Field implementation of the hybrid-ORS method shows that this method is well suited for quantifying fugitive PM EFs. The method offers the advantage of completely scanning multiple plume cross-sections during entire events and allowing for complete detection for tall or aloft plumes. Application of the method for sources of fugitive PM with different characteristics has the potential to expand the scope of current AP-42 EFs and increase their accuracy.

2.6 Acknowledgements

The authors thank the support from Department of Defense (DoD) Project SI-1400 and Chinese Academy of Sciences Visiting Professorship for Senior International Scientists, Grant 2011T2Z17. The authors also thank DRI for providing global positioning system, DustTrak™, anemometer, and wind vane data.

2.7 References

Bohren, C.F. and Huffman, D.R. (1983). Absorption and Scattering of Light by Small Particles. Wiley, New York.

Campbell, J.R., Hlavka, D.L., Welton, E.J., Flynn, C.J., Turner, D.D., Spinhirne, J.D., Scott, V.S., and Hwang, I.H. (2002). Full-Time, Eye-Safe Cloud and Aerosol Lidar Observation at Atmospheric Radiation Measurement Program Sites: Instruments and Data Processing. *J. Atmos. Ocean. Technol.* 19: 431–442.

Dockery, D.W. and Pope, C.A. (1994). Acute Respiratory Effects of Particulate Air Pollution. *Annu. Rev. Public Health* 15: 107–132.

Du, K. (2007). Optical Remote Sensing of Airborne Particulate Matter to Quantify Opacity and Mass Emissions. Ph.D. Dissertation, University of Illinois at Urbana-Champaign, Illinois, USA.

Du, K., Rood, M.J., Welton, E.J., Varma, R.M., Hashmonay, R.A., Kim, B.J., and Kemme, M.R. (2011a). Optical Remote Sensing to Quantify Fugitive Particulate Mass Emissions from Stationary Short-term and Mobile Continuous Sources: Part I. Method and Examples. *Environ. Sci. Technol.* 45: 658–65.

Du, K., Yuen, W., Wang, W., Rood, M.J., Varma, R.M., Hashmonay, R.A., Kim, B.J., and Kemme, M.R. (2011b). Optical Remote Sensing to Quantify Fugitive Particulate Mass

Emissions from Stationary Short-Term and Mobile Continuous Sources : Part II. Field Applications. *Environ. Sci. Technol.* 45: 666–672.

Du, K., Shi, P., Rood, M.J., Wang, K., Wang, Y., and Varma, R.M. (2013). Digital Optical Method to Quantify the Visual Opacity of Fugitive Plumes. *Atmos. Environ.* 77: 983–989.

Etyemezian, V., Ahonen, S., Nikolic, D., Gillies, J., Kuhns, H., Gillette, D., and Veranth, J. (2004). Deposition and Removal of Fugitive Dust in the Arid Southwestern United States: Measurements and Model Results. *J. Air Waste Manage. Assoc.* 54: 1099–1111.

Faulkner, W.B., Goodrich, L.B., Botlaguduru, V.S.V., Capareda, S.C., and Parnell, C.B. (2009). Particulate Matter Emission Factors for Almond Harvest as a Function of Harvester Speed. *J. Air Waste Manage. Assoc.* 59: 943–949.

Fernald, F.G., Herman, B.M., and Reagan, J.A. (1972). Determination of Aerosol Height Distributions by Lidar. *J. Appl. Meteorol.* 11: 482–489.

Gillies, J.A., Etyemezian, V., and Kuhns, H. (2005). Effect of Vehicle Characteristics on Unpaved Road Dust Emissions. *Atmos. Environ.* 39: 2341–2347.

Hashmonay, R.A., Kagann, R.H., Rood, M.J., Kim, B.J., Kemme, M.R., and Gillies, J. (2009). An Advanced Test Method for Measuring Fugitive Dust Emissions Using a Hybrid System of Optical Remote Sensing and Point Monitor Techniques. In, Kim,Y.J., Platt,U., Gu,M.B., and Iwahashi,H. (Eds), Atmospheric and Biological Environmental Monitoring. Springer Netherlands, 73–81.

Hess, M., Koepke, P., and Schult, I. (1998). Optical Properties of Aerosols and Clouds: the Software Package OPAC. *Bull. Am. Meteorol. Soc.* 79: 831–844.

Holmén, B.A., Eichinger, W.E., and Flocchini, R.G. (1998). Application of Elastic Lidar to PM_{10} Emissions from Agricultural Nonpoint Sources. *Environ. Sci. Technol.* 32: 3068–3076.

Kandler, K., Benker, N., Bundke, U., Cuevas, E., Ebert, M., Knippertz, P., Rodríguez, S., Schütz, L., and Weinbruch, S. (2007). Chemical Composition and Complex Refractive Index of Saharan Mineral Dust at Izaña, Tenerife (Spain) Derived by Electron Microscopy. *Atmos. Environ.* 41: 8058–8074.

Kuhns, H., Gillies, J., Etyemezian, V., Nikolich, G., King, J., Zhu, D., Uppapalli, S., Engelbrecht, J., and Kohl, S. (2010). Effect of Soil Type and Momentum on Unpaved Road Particulate Matter Emissions from Wheeled and Tracked Vehicles. *Aerosol Sci. Technol.* 44: 187–196.

McFarland, M.J., Olivas, A.C., Atkins, S.G., Kennedy, R.L., and Patel, K. (2007). Fugitive Emissions Opacity Determination Using the Digital Opacity Compliance System (DOCS). *J. Air Waste Manage. Assoc.* 57: 1317–1325.

Miller, C.A., Hidy, G., Hales, J., Kolb, C.E., Werner, A.S., Haneke, B., Parrish, D., Frey, H.C., Rojas-Bracho, L., Deslauriers, M., et al. (2006). Air Emission Inventories in North America: a Critical Assessment. *J. Air Waste Manag. Assoc.* 56: 1115–29.

NARSTO (2005). Improving Emission Inventories for Effective Air Quality Management Across North America Pasco, Washington.

Petzold, A., Rasp, K., Weinzierl, B., Esselborn, M., Hamburger, T., Dörnbrack, A., Kandler, K., Schütz, L., Knippertz, P., Fiebig, M., et al. (2009). Saharan Dust Absorption and Refractive Index from Aircraft-based Observations During SAMUM 2006. *Tellus B* 61: 118–130.

Pope, C. and Dockery, D. (2006). Health Effects of Fine Particulate Air Pollution: Lines That Connect. *J. Air Waste Manag. Assoc.* 56: 709 –742.

Seinfeld, J.H., Carmichael, G.R., Arimoto, R., Conant, W.C., Brechtel, F.J., Bates, T.S., Cahill,

T. a., Clarke, A.D., Doherty, S.J., Flatau, P.J., et al. (2004). ACE-ASIA: Regional Climatic and Atmospheric Chemical Effects of Asian Dust and Pollution. *Bull. Am. Meteorol. Soc.* 85: 367–380.

Sokolik, I., Andronova, A., and Johnson, T.C. (1993). Complex Refractive Index of Atmospheric Dust Aerosols. *Atmos. Environ. Part A. Gen. Top.* 27: 2495–2502.

Storelvmo, T., Hoose, C., and Eriksson, P. (2011). Global Modeling of Mixed-phase Clouds: The Albedo and Lifetime Effects of Aerosols. *J. Geophys. Res.* 116: D05207.

USEPA (2000). Meteorological Monitoring Guidance for Regulatory Modeling Applications.

USEPA (2015a). Emissions Factors & AP 42, Compilation of Air Pollutant Emission Factors. http://www.epa.gov/ttnchie1/ap42. (Accessed February 2015).

USEPA (2015b). Emissions Inventories. http://www.epa.gov/ttn/chief/eiinformation.html. (Accessed February 2015).

Varma, R.M., Hashmonay, R.A., Du, K., Rood, M.J., Kim, B.J., and Kemme, M.R. (2006). A Novel Method to Quantify Fugitive Dust Emissions Using Optical Remote Sensing. In, Platt,U. and Kim,Y. (Eds), Advanced Environmental Monitoring. Springer-Verlag GmbH, pp. 143–154.

Watson, J.G. (2002). Visibility: Science and Regulation. *J. Air Waste Manag. Assoc.* 52: 628–712.

Watson, J.G. and Chow, J.C. (2000). Reconciling Urban Fugitive Dust Emissions Inventory and Ambient Source Contribution Estimates: Summary of Current Knowledge and Needed Research. DRI Document No. 6110.4F.

Yuen, W., Johnsen, D.L., Koloutsou-vakakis, S., Rood, M.J., Byung, J., and Kemme, M.R. (2014). Open Burning and Open Detonation PM_{10} Mass Emission Factor Measurements

with Optical Remote Sensing. *J. Air Waste Manage. Assoc.* 64: 227–234.

CHAPTER 3: OPEN BURNING AND OPEN DETONATION PM_{10} MASS EMISSION FACTOR MEASUREMENTS WITH OPTICAL REMOTE SENSING[2]

3.1 Abstract

Emission factors (EFs) of particulate matter with aerodynamic diameter ≤ 10 μm (PM_{10}) from the open burning/open detonation (OB/OD) of energetic materials were measured using a hybrid-optical remote sensing (hybrid-ORS) method. This method is based on the measurement of range-resolved PM backscattering values with a micropulse lidar (MPL). Field measurements were completed during March 2010 at Tooele Army Depot, Utah, which is an arid continental site. PM_{10} EFs were quantified for OB of M1 propellant and OD of 2, 4, 6-trinitrotoluene (TNT). EFs from this study are compared to previous OB/OD measurements reported in the literature that have been determined with point measurements either in enclosed or ambient environments, and with concurrent airborne point measurements. PM_{10} mass EFs, determined with the hybrid-ORS method, were $7.8x10^{-3}$ kg PM_{10}/kg M1 from OB of M1 propellant, and 0.20 kg PM_{10}/kg TNT from OD of TNT. Compared to previous results reported in the literature, the hybrid-ORS method EFs were 13% larger for OB and 174% larger for OD. Compared to the concurrent airborne measurements, EF values from the hybrid-ORS method were 37% larger for OB and 54% larger for OD. For TNT, no statistically significant differences were observed for the EFs measured during the detonation of 22.7 kg and 45.4 kg of TNT, supporting that the total amount of detonated mass in this mass range does not have an effect on the EFs for OD of TNT.

[2] Reprinted, with permission and minor revisions, from Yuen, W., Johnsen, D.L., Koloutsou-vakakis, S., Rood, M.J., Byung, J., and Kemme, M.R. (2014). Open Burning and Open Detonation PM_{10} Mass Emission Factor Measurements with Optical Remote Sensing. *J. Air Waste Manage. Assoc.* 64: 227–234.

3.2 Introduction

Particulate matter (PM) in the atmosphere adversely affects health (Dockery and Pope, 1994; Jung et al., 2012), contributes to visibility degradation (Watson, 2002; Kavouras et al., 2009), and affects the radiative balance of the Earth (Anenberg et al., 2012). In the United States, (U.S.), PM that is ≤ 10 μm and ≤ 2.5 μm in aerodynamic diameter (PM_{10} and $PM_{2.5}$, respectively) is a criteria air pollutant for which National Ambient Air Quality Standards (NAAQS) have been set. For air quality management purposes, PM emission inventories are useful to identify sources and quantify their emissions. A PM emissions inventory contains emissions estimated based on emission factors (EFs) and PM producing activity levels for each PM producing source. An EF represents the amount of pollutant that is released to the atmosphere per unit of activity that releases the pollutant (e.g., mass of PM generated per unit mass of energetic material detonated) (USEPA, 2016). Primary PM, which is the focus of this paper, is emitted from a wide range of stationary, mobile, areal, and fugitive sources. This study focuses on fugitive PM, defined by the U.S. Environmental Protection Agency (USEPA) as PM that is not emitted from a confined flow stream (USEPA, 2016; Watson and Chow, 2000) because fugitive sources have a large contribution to primary PM emissions. For example, in the U.S., fugitive PM emissions are estimated to contribute 89% and 66% of the total primary PM_{10} and $PM_{2.5}$ mass emissions, respectively (Watson and Chow, 2000). As mandated by the 1990 Clean Air Act, the USEPA has developed the AP-42 database with EFs from various activities (USEPA, 2016). Emissions of PM from various fugitive sources are characterized by a high level of uncertainty. It is valuable to confirm or improve EFs in this database to ensure that emissions are properly characterized.

This paper analyzes the EFs from two sources of fugitive PM: open burning (OB) and open detonation (OD) of energetic materials. OB and OD are used by the U.S. Department of

Defense (DoD) during demilitarization activities for the disposal of waste materials such as propellants, explosives, and other military munitions. However, there is concern about the impacts that these disposal methods have on human health and the environment. DoD installations, including army ammunition plants, are required to comply with the Resource Conservation and Recovery Act (RCRA) to operate OB/OD facilities. Since 1984, DoD has undertaken activities to characterize the emissions of air pollutants emitted during military OB and OD (Mitchell and Suggs, 1998). RCRA permits provide annual limits on the amount of energetic materials that can be disposed of at OB/OD facilities. The permit limitations are based on human health risk assessments that include risk estimates from airborne exposure to emissions generated from OB/OD (Mitchell and Suggs, 1998).

Field PM emissions from OB/OD are difficult to characterize because of rapid dispersion, short event duration, heterogeneous emission concentrations, large plume lift, soil entrainment, and explosion safety restrictions. Attempts to measure OB/OD emissions with instruments on aircraft with personnel are challenging due to safety concerns for the airborne personnel and also due to the short duration of the plume events, especially after OD. Use of instruments suspended by balloons have offered an alternative (Aurell et al., 2011). Johnson (1992) reports EFs from the OB of M1 propellants that were determined using instruments aboard an aircraft and using the carbon mass balance method. The carbon mass balance method assumes that carbon mass within the energetic material remains constant during OB/OD, and the ratio of an analyte concentration to the total carbon concentration is used to determine the analyte's EF. Alternative methods that have been employed to measure EFs from OB/OD include a chamber (930 m^3) known as a BangBox (Mitchell and Suggs, 1998) and more recently a "Flyer", which is a balloon that carries instruments 20 – 70 m above ground and downwind from the source to measure select air

pollutant concentrations (Aurell et al., 2011, 2012). For BangBox measurements, small quantities (0.1 – 3 kg) of energetic materials are burned or detonated (Mitchell and Suggs, 1998). However, it is uncertain whether sampling in a confined environment provides similar results compared to OB/OD occurring in open air. Two factors that might affect results from sampling in the BangBox are 1) possible dependence of the EF on the amount of the energetic material, given that a small amount is burned or detonated inside the BangBox, and 2) possible sampling artifacts resulting from the chamber walls (Johnson, 1992).

In this research, a hybrid-optical remote sensing (hybrid-ORS) method is described to quantify fugitive PM EFs for OB/OD of energetic materials. The hybrid-ORS method is appropriate for determining OB/OD EFs because it enables to scan numerous cross-sections of the PM plume as it disperses. Thus, detection of the plume occurs in real-time, in-situ, and with no need for numerous point measurement devices (Du et al., 2011a). For the hybrid-ORS method, mass PM concentration measurements from a tapered element oscillating microbalance (TEOM) and optical measurements from a micropulse light detection and ranging (lidar, MPL) device were used to determine the PM EFs during a 2010 field campaign at the Tooele Army Depot in Utah. Results obtained with this hybrid-ORS method are presented and compared to concurrent field measurements from the "Flyer" that was operated by USEPA personnel and contractors (Aurell et al., 2011) and previously reported results (Johnson, 1992; Mitchell and Suggs, 1998). The means and coefficients of variation of PM EFs for the OB of M1 propellant and OD of 2, 4, 6-trinitrotoluene (TNT) events are reported and compared with values reported in literature. EFs from the detonation of two select amounts of TNT are also reported and compared to determine if the amount of energetic material has an effect on the EF values. This study is valuable

because, to the best of our knowledge, this is the first study that uses a hybrid-ORS technique to determine OB/OD EFs.

3.3 Methods

Field Site and Instrumentation

During March 2010, a hybrid-ORS method was implemented at Tooele Army Depot in Utah, which is an arid continental site, to quantify fugitive PM mass EFs from the OB/OD of energetic materials. Two types of energetic materials were tested: 1) M1 propellant at 22.7 kg (50 lb) per OB, and 2) TNT at 22.7 and 45.4 kg (50 and 100 lb) per OD. The schematic describing the location of the instruments relative to the OB/OD source is shown in Figure 3.1.

Figure 3.1. Source and hybrid optical remote sensing instrument layout to characterize EFs from the open burning and detonation of energetic materials during a field campaign in Tooele, Utah.

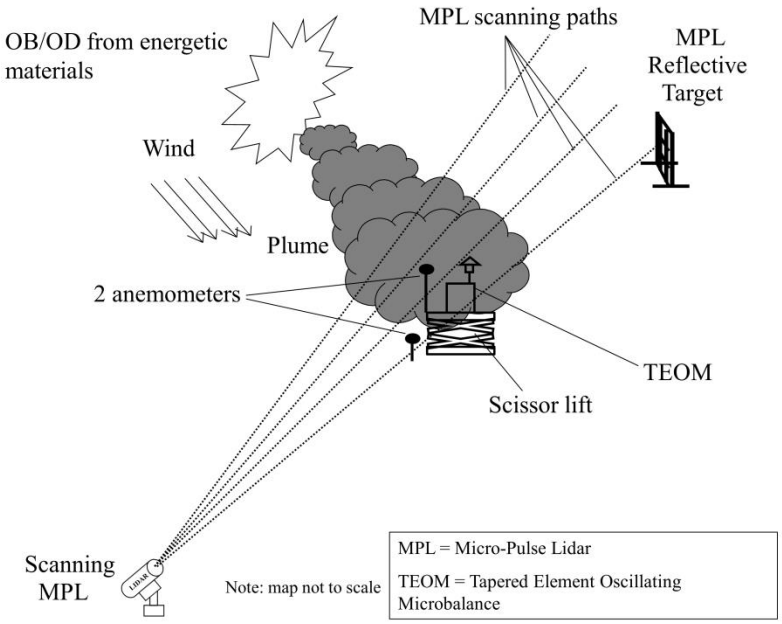

The MPL (SigmaSpace, Model: MPL-4B-527) is an elastic backscatter lidar that measures range-resolved (i.e. distance dependent) extinction coefficients. Specifications for the MPL are shown in Table 3.1. The MPL laser was aimed at a reflective target that consists of a vertical metal wire mesh with cross-section of 1.2 m by 2.4 m. The MPL and the target were

located such that the MPL's laser path was downwind from the source and, as much as possible, perpendicular to the wind and subsequently plume's dispersion direction, as determined by observation and the hourly wind direction forecast (NOAA, 2010). This ensures the entire plume was passing through the ORS's scanning plane to enable the EF quantification. Wind speed and direction requirements to ensure full plume scans will be described in the "quality assurance/quality control (QA/QC)" subsection. For safety reasons, the downwind distance of the MPL's laser path was 25 m from the OB sources and 100 m from the OD sources. As documented in a study (Etyemezian et al., 2004) PM_{10} deposition is negligible for such distances away from the point of emission. They reported measurements of deposition of PM_{10} from the movement of vehicles on unpaved roads in an arid location under different atmospheric stability conditions. Their study showed that there were no measurable emission flux differences for PM_{10} sampled at 7 m, 50 m, and 100 m away from the point of emission. They also estimated PM_{10} deposition by an algorithm similar to the one used in the USEPA ISC3 model, and their results showed < 5% loss of PM_{10} due to deposition, at a distance of 100 m away from the point of emission (Etyemezian et al., 2004). Based on these findings, PM_{10} loss due to deposition between the source and the MPL's laser path was considered negligible in our study.

Table 3.1. MPL specifications.

Wavelength	527 nm
Laser Power	1.0 W
Output Energy	~ 8 μJ
Pulse Repetition Frequency	2.5 kHz
Transceiver Aperture	178 mm
Transceiver Field-of-View	~ 100 μrad
Range Resolution	15 m
Maximum Range	60 km

The MPL was operated in a temperature-controlled trailer with hydraulic stabilizers at each corner of the trailer to provide stable alignment of the instrument. The MPL was mounted on a positioner (ORBIT, Advanced Technologies, Model: AL-4011-1E with control system AL-1613-3J, specifications are shown in Table 3.2) such that the MPL's laser measurement plane ranged vertically from an elevation of 0 m to 100 m for characterizing a plume. The 2-D range-resolved backscattered photon counts along the dust plume's cross-sections were measured with the MPL to determine the 2-D light extinction profiles of the plume, as described briefly in the "EF calculation method" subsection and in detail in Du et al. (2011a, 2011b). The photon counts were measured as pulsed laser light was emitted from the MPL and then backscattered from the plume's PM toward the MPL's detector. The MPL recorded photon counts at 1 Hz frequency for the entire duration of each plume. Scanning for plume events involved using either the fixed-position or full-scan mode. The fixed-position mode was used to determine the calibration constants for the MPL and the mass extinction efficiency (MEE) values for each plume event, while the full-scan mode was used to determine the 2-D backscattered photon count profiles measured by the MPL. In the full-scan mode, the maximum scanning angle was selected so as to contain the entire plume in accordance with the QA/QC procedures that described below.

Table 3.2. Positioner specifications.

Data Take-off Accuracy	Azimuth	$\pm 0.1^{o}$
	Elevation	$\pm 0.1^{o}$
Nominal Speed	Azimuth	$12^{o}/s$
	Elevation	$12^{o}/s$
Limit-to-limit Travel	Azimuth	$\pm 210^{o}$
	Elevation	-5^{o} to 185^{o}

The TEOM (Rupprecht & Patashnick, Model 1400) was located 10 m above the ground to intercept the dispersing plume. The locations of the TEOM and the MPL's measurement path

were co-located so that the MPL and TEOM measured the same location of the plume intermittently to determine the MEE values, as described in the "EF calculation method" subsection. Wind speed and direction were determined with two 2-D mechanical anemometers (R. M. Young Wind Sentry) located next to the TEOM, one at 11.7 m and the other 2.0 m above ground. Wind speed and direction measurements were recorded at a 1 Hz frequency.

EF Calculation Method by Hybrid Optical Remote Sensing

The method for calculating an EF from the spatially-resolved MPL photon counts is shown in Figure 3.2.

Figure 3.2. Flow chart of method used to estimate mass EFs for PM_{10} produced from open burning and open detonation (OB/OD).

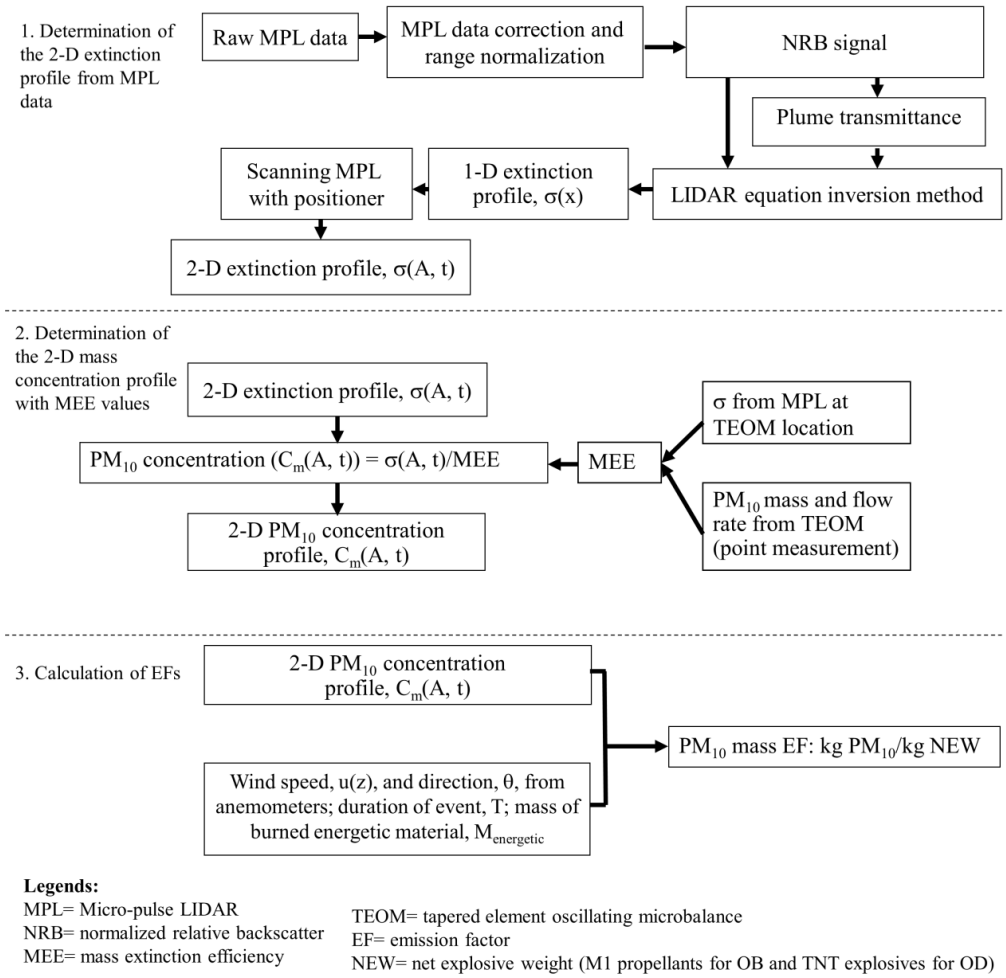

Determination of the 2-D Extinction Profile from MPL Data

The raw MPL photon counts were corrected, range normalized and then converted to normalized relative backscatter (NRB) values (Campbell et al., 2002). 2-D NRB profiles were converted to 2-D light extinction profiles with the near-end lidar inversion technique (Du et al., 2011a; Fernald et al., 1972). A reflective target that was located on the opposite side of the plume from the MPL was used to provide reference data to calculate the calibration constant, K*, for MPL scans at the horizontal level. This constant is the ratio of the MPL system constant (K) to the extinction-to-backscatter ratio (S), and is used to relate the MPL backscatter photon counts to extinction coefficients. The K* calculated from the MPL scans at the horizontal level was then assumed to be the same as the K* at the slanted angles, based on the assumption that the particle properties within the fugitive PM plume are constant. The assumed K* was used to calculate the light extinction profiles for MPL scans at the slanted angles.

Determination of the 2-D Mass Concentration Profiles with MEE Values

The hybrid-ORS method entails using a rapid-response point measurement to determine PM mass concentration and ORS (i.e. the MPL and method described in the previous section) to determine light extinction (Hashmonay et al., 2009). The 2-D PM mass concentration profiles were determined from the 2-D light extinction profiles as described above, and the PM_{10} MEEs of OB and OD activities. MEE is defined as σ/C_m, where σ is the total extinction coefficient and C_m is PM_{10} mass concentration, both measured at the same location. The MEE for PM_{10} was determined from MPL measurements and in-situ point mass concentration measurements using the TEOM. During each plume event, data from the TEOM demonstrated distinct step responses, in which collected mass increased as the plume was passing across the TEOM location and then stabilized after the plume had passed the TEOM location. MEE was determined as described by Eq. (3.1):

$$MEE = \frac{F\int_0^T \sigma(t)\,dt}{m_T} \tag{3.1}$$

where,

MEE = mass extinction efficiency (m^2/g)

T = duration of an event (s)

m_T = total collected PM_{10} mass during an event, measured by the TEOM (μg)

F = TEOM gas sample flow rate (L/min)

$\sigma(t)$ = extinction coefficient measured by MPL at the TEOM location at time t (m^{-1}).

K* and MEE values were estimated for select plume events that were measured using the fixed position mode of the MPL. In the fixed position mode, MPL measurements were taken only in the horizontal angle. MEEs calculated from events that were measured in fixed position mode were averaged for each type of activity (OB or OD). A single MEE value was estimated for all of the OB events and a different single value was estimated for all of the OD events. These MEE values were then treated as constants for events that were measured in full-scan mode, where the MPL characterized the entire cross-section of the plumes. Extinction profiles ($\sigma(\Delta A, t)$), measured in full-scan mode, were converted to PM mass concentration profiles ($C_m(\Delta A, t)$), by Eq. (3.2):

$$C_m(\Delta A, t) = \frac{\sigma(\Delta A, t)}{MEE} \tag{3.2}$$

Using a single MEE value for OB or OD assumes that MEE is spatially and temporally constant within a plume type for all events. This is a reasonable assumption since the MEE is a normalized particle property that depends on particle size distribution, particle density, and optical properties, which are assumed not to change among different OB or OD events with the

same energetic material. Upadhyay et al. (2008) show a strong linear relationship between PM_{10} extinction coefficients and mass concentrations ($R^2 = 0.87$ with 109 data points), supporting the case for MEE consistency.

Calculation of EFs

EFs were determined by integrating 2-D PM mass concentration profiles during each plume event measured in full-scan mode, with respect to wind speed, wind direction, duration of each event, source type, and mass of energetic material burned or detonated (Eq. (3.3)):

$$EF = \frac{1}{M_{energetic}} \sum_{t=0}^{T} \left(\sum C_m \left(\Delta A, t \right) \Delta A \right) u\left(z \right) \cos\theta \Delta t \qquad (3.3)$$

where $M_{energetic}$ is the mass (kg) of energetic materials burned or detonated (used as normalizing factor for EF); T is duration of the event (s); $C_m(\Delta A, t)$ is the mass concentration (g/m^3) of PM_{10} in the plume at time, t, within the differential area ΔA (m^2) (Figure 3.3); u(z) is the wind speed (m/s) at height z; and θ is the angle (deg) between the wind direction and the line that is normal to the ORS observing plane during an event. EFs are estimated here as kg-PM_{10}/kg-NEW, where NEW is the net explosive weight. Integration of the 2-D PM mass concentration profiles was performed using polar coordinates (Figure 3.3).

Figure 3.3. Parameters in Eq. (3.3) are shown in this schematic of MPL measuring a plume. θ is wind direction and ΔA is the differential area between the scan angles and MPL measurement points (areas bounded by dotted lines). ΔA center points are 15 m (MPL resolution) apart. The sum of all ΔA areas defines the ORS scanning plane (bold dotted lines). The maximum scanning plane angle is selected to contain the entire plume.

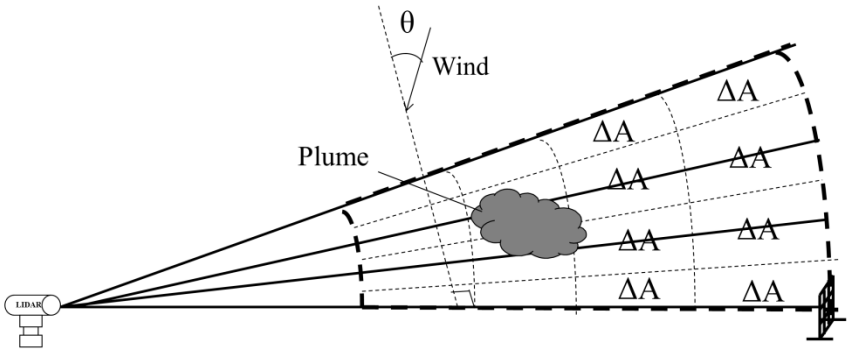

Power law regressions (USEPA, 2000) were fitted to the measured wind speeds at heights of 2.0 m and 11.7 m to determine wind speed at the heights of the measurements provided by the MPL. The fitted regression coefficients were determined for each plume event. In this field campaign, the power-law exponent coefficient ranged from -0.06 to 0.74. Measured horizontal wind directions during each event were first converted to θs and the cosine of θs were averaged for each event. It was assumed that wind direction was independent of elevation for each plume event.

The duration of each plume generation event was determined as the amount of time for the plume to pass through the vertical measurement plane, as detected by the MPL. Measured durations for each event were between 40 and 60 s. Each plume event was described by the type of energetic materials and mass that was burned or detonated.

Quality Assurance/Quality Control (QA/QC) Procedures

A three step QA/QC procedure was followed for the measurement data. First, it was verified that the MPL scanned the entire cross-section of the plume during each analyzed plume event. Plume events were not included in the analysis if any of the three conditions occurred: 1)

the wind did not direct the plume to the MPL's scanning plane due to wind direction change (i.e., $\theta > 84°$) or low wind speed (i.e., < 1.0 m/s), 2) the largest angle of vertical scan was not high enough to capture the highest part of the plume, and 3) the MPL was in the fixed-position mode. Second, if the MPL measured zero backscatter signals from the reflective target, it was an indication that the plume was too opaque to be measured and results from such plumes were not included in the analysis. Finally, outliers were evaluated for OB EF and OD EF results. Data points that were above or below three interquartile ranges from the upper or lower quartile were removed. Analysis of outliers resulted in the removal of one OD measurement value in the final analysis.

3.4 Results and Discussion

Values for the parameters used for the calculation of the EFs for OB of M1 and OD of TNT during the field campaign are shown in Table 3.3. The mean PM_{10} MEE values for OB and OD are 2.5 m^2/g and 0.44 m^2/g, which are in the similar order of magnitude to the values in literature discussed in Section 1.2, which is from 0.5 to 5.9 m^2/g.

Table 3.3. Values of parameters used for the calculation of EFs for OB and OD events.

Quantity	Open Burning of M1		Open Detonation of TNT	
	Mean	Standard Deviation	Mean	Standard Deviation
K* (km^2 m)/ (μs μJ sr)	3594	NA	3213	NA
MEE (m^2/g)	2.5	1.1	0.44	0.10
	Minimum	Maximum	Minimum	Maximum
Wind Speed at 2 m (m/s)	1.1	5.7	1.8	5.5
Wind Speed at 11.7 m (m/s)	1.6	6.5	2.3	9.1
Wind Direction (θ, °)	13	84	9	67

NA – Not applicable

A summary of PM_{10} MEE values measured by Du's ORS method (Du et al. 2011a, Kim et al., 2008) and hybrid-ORS method is shown in Table 3.4 and Table 3.5. From these two tables,

the PM_{10} MEE values for typical desert dust, dust generated by helicopter, and dust generated by OD of TNT have similar order of magnitude. These PM_{10} MEE values are between 0.34 m^2/g and 0.82 m^2/g. A possible reason that these MEE values are similar is that these activities disturb desert dust material to the air, resulting in fugitive PM plumes of similar particle properties. The moving vehicle and the OB of M1 have similar order of magnitude of PM_{10} MEE values, which are 2.1 m^2/g and 2.5 m^2/g, respectively. The PM_{10} MEE value due to the moving vehicle may need to be verified by further experiments because these activities also disturb desert dust material to the air, so the PM_{10} MEE should be in the same order of magnitude as the previous three sources. The PM_{10} MEE value due to the OB of M1 is different from the other sources possibly because the fugitive PM comes more from the burnt material, rather than the disturbance of desert dust material. Thus, the particle properties for the OB of M1 are different from the other aforementioned sources, resulting different MEE values.

Table 3.4. Summary of PM_{10} MEE values measured by the ORS method.

Source type	**Artillery back blast**	**Helicopter**
Location	Yuma, AZ	Yuma, AZ
MEE measurement method	Simulation using 25 different particle refractive indices. Assumed particle density, particle size distribution measured by OP-FTIR and OP-LT	Extinction coefficient by OP-LT, PM mass concentration by DustTrak, measured inside a tent
Time scale of measurement	OP-FTIR and OP-LT: 10 second averaged measurements	OP-LT and DustTrak: 10 second averaged measurements
Length scale of measurement	OP-FTIR and OP-LT: 3 m path-integrated	OP-LT: 4 m path-integrated, DustTrak: point measurement
# of data points	25	34 (Site 1), 30 (Site 2)
PM_{10} MEE mean (m^2/g)	0.342	0.62 (Site 1), 0.82 (Site 2)
PM_{10} MEE standard deviation (m^2/g)	0.002	Not available
R^2	Not available	0.65 (Site 1), 0.69 (Site 2)
Reference	Du et al., 2011a	Kim et al., 2008

Table 3.5. Summary of PM_{10} MEE values measured by the hybrid-ORS method.

Source type	**Moving vehicle (Chapter 2)**	**Open burning of M1**	**Open detonation of TNT**
Location	Fort Carson, CO	Tooele, UT	Tooele, UT
MEE measurement method	Extinction by OP-LT, PM mass concentration by DustTrak	Extinction by MPL, PM mass concentration by TEOM	Extinction by MPL, PM mass concentration by TEOM
Time scale of measurement	Duration of each event	Duration of each event	Duration of each event
Length scale of measurement	OP-LT: 100 m path-integrated, DustTrak: point measurement	MPL: 15 m path-integrated, TEOM: point measurement	MPL: 15 m path-integrated, TEOM: point measurement
# of data points	106	2	4
PM_{10} MEE mean (m^2/g)	2.1	2.5	0.44
PM_{10} MEE standard deviation (m^2/g)	1.1	1.1	0.10

M1: M1 propellant
TNT: 2, 4, 6-trinitrotoluene

An example of the temporal variation of the 2-D light extinction profiles for a 40 s OD event is shown in Figure 3.4. The OD plume's height, width, and light extinction coefficient reached 80 m, 70 m, and 0.03 m^{-1}, respectively, along the cross-section of the plume, as sampled by the MPL. This light extinction coefficient corresponds to a mass concentration of 68 mg/m^3. The EF for this OD event was 0.31 kg PM_{10}/kg TNT.

Figure 3.4. Time series of the 2-D light extinction profiles for an open detonation event. Profiles are shown for every 10 s of the event.

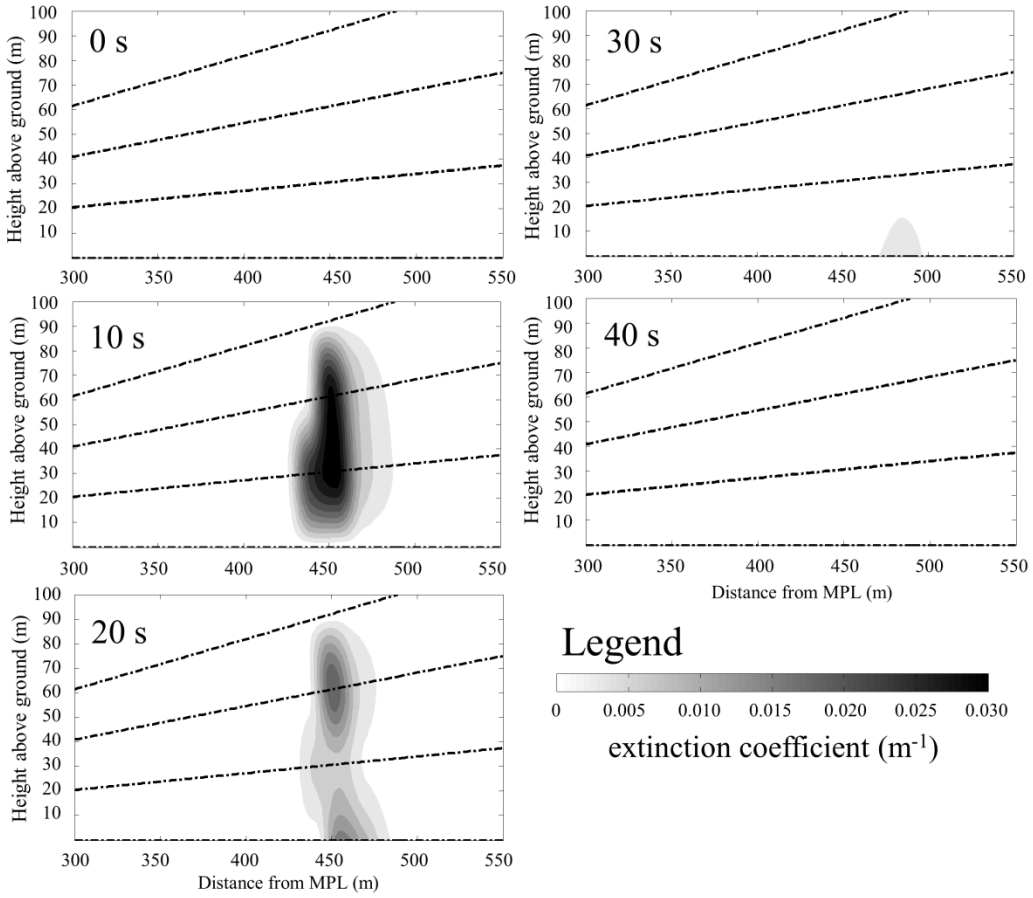

Results describing the EF values from OB/OD events measured in full-scan mode during this field campaign are displayed in Table 3.6. The PM_{10} mass EFs from OB of M1 propellant and OD of TNT were determined by the hybrid-ORS method to be 7.8×10^{-3} kg PM_{10}/kg M1 and 0.20 kg PM_{10}/kg TNT, respectively. The corresponding coefficients of variation, which is the ratio of standard deviation to the mean, are 56% and 54%. The 95% confidence intervals of the EFs measured by the hybrid-ORS method are [6.5×10^{-3}, 9.3×10^{-3}] kg PM_{10}/kg M1 for OB and [0.16, 0.24] kg PM_{10}/kg TNT for OD. The EFs determined by the hybrid-ORS method were then compared to the concurrent "Flyer" measurements and previous literature values. The "Flyer" EF results were determined by USEPA personnel and reported by Aurell et al. (2011). The literature

OB EF of M1 was cited from previous OB field measurements (Johnson, 1992), while the literature OD EF of TNT was cited from previous BangBox measurements (Mitchell and Suggs, 1998). EFs from the "Flyer" were determined to be $5.7x10^{-3}$ kg PM_{10}/kg M1 and 0.13 kg PM_{10}/kg TNT, for OB and OD, respectively (Aurell et al., 2011). Coefficient of variation for OB EFs measured by the "Flyer" is not reported, while coefficient of variation for OD EFs measured by the "Flyer" is 54% (Aurell et al., 2011). OB EF from Johnson (1992) was $6.9x10^{-3}$ kg PM_{10}/kg M1. OD EF from Mitchell and Suggs (1998) was 0.073 kg PM_{10}/kg TNT, with a coefficient of variation of 2%.

Table 3.6. Summary of PM_{10} emission factors (EFs) for open burning and open detonation events.

Test Type and EFs		Open Burning of M1		Open Detonation of TNT	
		Mean EF	**Coefficient of Variation (%)**	**Mean EF**	**Coefficient of Variation (%)**
PM_{10} (kg/kg NEW)	Hybrid-ORS [a]	$7.8x10^{-3}$	56	0.20	54
	"Flyer" [b]	$5.7x10^{-3}$	NA	0.13	54
	Literature [c]	$6.9x10^{-3}$	NA	0.073	2

NA = not available; NEW = net explosive weight (M1 propellants for OB and TNT explosives for OD)
a. Number of samples: OB of M1: 37, OD of TNT: 24
b. Aurell et al. 2011
c. Johnson 1992 for Open Burning; Mitchell and Suggs 1998 for Open Detonation

The hybrid-ORS measured EF for OB of M1 was 13% higher than the EF reported by Johnson (1992) showing close agreement between the methods. However, the hybrid-ORS measured EF for OD of TNT was 174% higher than the EF reported by Mitchell and Suggs (1998). A similar comparison of the "Flyer" measurements to previous literature values for OB of M1 showed that the EFs determined by airborne balloon measurements were 17% lower than the EF reported by Johnson (1992) for OB, and 78% higher than the EF reported by Mitchell and Suggs (1998) for OD. The OB EF from Johnson (1992) is similar to hybrid-ORS and "Flyer" measurements (absolute percentage differences < 17%), possibly because it also comes from

field measurements. However, PM_{10} EF for OD from Mitchell and Suggs (1998) is lower than those measured by the hybrid-ORS or "Flyer" methods, which is possible because the BangBox measurement was completed on a steel-lined pit (Mitchell and Suggs, 1998), which excluded entrainment of soil that occurs during OD in field conditions.

Compared to the concurrent airborne measurements, the hybrid-ORS method EFs were 37% larger for OB and 54% larger for OD. Comparisons of two-means t-test (unequal variance) (Montgomery and Runger, 2011) were performed on "Flyer" and hybrid-ORS EF measurements. The t-test shows that "Flyer" OD EF values were significantly smaller than hybrid-ORS EF values (one-tailed p-value = 0.005). Statistical testing of the means for OB is not reported because "Flyer" OB EF coefficient of variation was not reported. These differences between the hybrid-ORS and "Flyer" EF are likely caused by the following: 1) the "Flyer" sampled the plume 20 – 70 m above the location of the source with the height depending on if it was an OB or OD event (Aurell et al., 2011), whereas the MPL scanned plume cross-sections throughout the vertical extent of the plume; 2) the Flyer uses chemical properties (carbon balance method) to estimate the EFs whereas the hybrid-ORS EFs are estimated based on optical properties. All methods used to quantify PM EFs from OB/OD have uncertainty sources that are challenging to quantify. One such source for the hybrid-ORS method is the assumption that PM MEE is spatially and temporally homogeneous. A simple sensitivity analysis shows that if, for example, MEE had an error of ±10% for OB and OD, the range of average EF for OB will be 7.1×10^{-3} to 8.7×10^{-3} kg PM_{10}/kg M1 and for OD 0.18 to 0.22 kg PM_{10}/kg TNT. An additional uncertainty in the estimation of EFs by the hybrid ORS method is introduced by meteorology (variable wind speed and direction). Such uncertainties need further targeted investigation in future field campaigns.

The effect of scaling the quantity of detonated material on determining PM_{10} EFs was investigated for hybrid-ORS measurements of OD events. The effect of scaling on OB events was not studied because 45.4 kg (100 lb) of M1 propellant was used for all OB events. For OD events, explosive quantities were 22.7 kg (50 lb) and 45.4 kg (100 lb). A comparison of two-means t-test (unequal variance) was performed (Montgomery and Runger, 2011) using the average EFs, measured by the MPL method, for events corresponding to 22.7 kg and 45.4 kg of TNT detonations, as shown in Table 3.7. The two-tailed p-value is 0.69 (> 0.05), demonstrating that the two mean EFs are not significantly different at the 95% confidence level. This is encouraging because it indicates that changes in TNT mass are not expected to affect EFs.

Table 3.7. Two-sample t-test (unequal variance) to examine the significance of difference between the hybrid-ORS EFs determined for select TNT masses.

Mass Detonated (kg TNT)	**22.7**	**45.4**
Number of Events	10	14
Mean EF (kg PM_{10}/kg TNT)	0.21	0.19
Standard Deviation (kg PM_{10}/kg TNT)	0.11	0.10
p-value of Two-tailed t-test	0.69	

3.5 Conclusions

Emission factors (EFs) of particulate matter with aerodynamic diameters < 10 μm (PM_{10}) were obtained by the hybrid-optical remote sensing (hybrid-ORS) method. These results are compared with independent yet simultaneous measurements completed by a USEPA "Flyer" instrument carrying platform for OB and OD. EFs estimated from the hybrid-ORS method are higher than those obtained by the "Flyer" during the same field campaign. Both hybrid-ORS and "Flyer" EFs are higher than the EFs obtained with BangBox OD EF during past measurements. Regarding scaling effects, results from the hybrid-ORS method show that the amount of

energetic material is not statistically significant for OD EF determination given the variation in the measurements.

What we have learned from these experiments is that all methods involve uncertainties that can only be quantified with specific measurements that are targeted toward quantifying uncertainty. Until such measurements are possible, the existing measurements offer a wide range of values for OB and OD PM_{10} EFs. The advantage offered by the hybrid-ORS method is that it enables scanning of the whole plume as it disperses past the MPL measurement plane. Increasing the MPL's resolution can further improve the accuracy of the measurements.

3.6 Acknowledgements

The authors thank Strategic Environmental Research and Development Program (SERDP Project WP-1672) for the funding of this project.

3.7 References

Anenberg, S.C., Schwartz, J., Shindell, D., Amann, M., Faluvegi, G., Klimont, Z., Janssens-Maenhout, G., Pozzoli, L., Van Dingenen, R., Vignati, E., et al. (2012). Global Air Quality and Health Co-benefits of Mitigating Near-term Climate Change Through Methane and Black Carbon Emission Controls. *Environ. Health Perspect.* 120: 831–839.

Aurell, J., Gullett, B.K., Pressley, C., Tabor, D.G., and Gribble, R.D. (2011). Aerostat-lofted Instrument and Sampling Method for Determination of Emissions from Open Area Sources. *Chemosphere* 85: 806–811.

Aurell, J., Gullett, B.K., and Yamamoto, D. (2012). Emissions from Open Burning of Simulated Military Waste from Forward Operating Bases. *Environ. Sci. Technol.* 46: 11004–11012.

Campbell, J.R., Hlavka, D.L., Welton, E.J., Flynn, C.J., Turner, D.D., Spinhirne, J.D., Scott, V.S., and Hwang, I.H. (2002). Full-Time, Eye-Safe Cloud and Aerosol Lidar Observation at

Atmospheric Radiation Measurement Program Sites: Instruments and Data Processing. *J. Atmos. Ocean. Technol.* 19: 431–442.

Dockery, D.W. and Pope, C.A. (1994). Acute Respiratory Effects of Particulate Air Pollution. *Annu. Rev. Public Health* 15: 107–132.

Du, K., Rood, M.J., Welton, E.J., Varma, R.M., Hashmonay, R.A., Kim, B.J., and Kemme, M.R. (2011a). Optical Remote Sensing to Quantify Fugitive Particulate Mass Emissions from Stationary Short-term and Mobile Continuous Sources: Part I. Method and Examples. *Environ. Sci. Technol.* 45: 658–65.

Du, K., Yuen, W., Wang, W., Rood, M.J., Varma, R.M., Hashmonay, R.A., Kim, B.J., and Kemme, M.R. (2011b). Optical Remote Sensing to Quantify Fugitive Particulate Mass Emissions from Stationary Short-Term and Mobile Continuous Sources : Part II. Field Applications. *Environ. Sci. Technol.* 45: 666–672.

Etyemezian, V., Ahonen, S., Nikolic, D., Gillies, J., Kuhns, H., Gillette, D., and Veranth, J. (2004). Deposition and Removal of Fugitive Dust in the Arid Southwestern United States: Measurements and Model Results. *J. Air Waste Manage. Assoc.* 54: 1099–1111.

Fernald, F.G., Herman, B.M., and Reagan, J.A. (1972). Determination of Aerosol Height Distributions by Lidar. *J. Appl. Meteorol.* 11: 482–489.

Hashmonay, R.A., Kagann, R.H., Rood, M.J., Kim, B.J., Kemme, M.R., and Gillies, J. (2009). An Advanced Test Method for Measuring Fugitive Dust Emissions Using a Hybrid System of Optical Remote Sensing and Point Monitor Techniques. In, Kim,Y.J., Platt,U., Gu,M.B., and Iwahashi,H. (Eds), Atmospheric and Biological Environmental Monitoring. Springer Netherlands, 73–81.

Johnson, M. (1992). *Development of Methodology and Technology for Identifying and*

Quantifying Emission Products from Open Burning and Open Detonation Thermal Treatment Methods. Field Test Series A, B, and C, Volume 1 Test Summary - Final Report.

Jung, M.H., H.R. Kim, Y.J. Park, D.S. Park, K.H. Chung, and S.M. Oh (2012). Genotoxic Effects and Oxidative Stress Induced by Organic Extracts of Particulate Matter (PM_{10}) Collected from a Subway Tunnel in Seoul, Korea. *Mutat. Res. Genet. Toxicol. Environ. Mutagen.* 749 (1-2): 39–47.

Kavouras, I.G., V. Etyemezian, D.W. DuBois, J. Xu, and M.L. Pitchford (2009). Source Reconciliation of Atmospheric Dust Causing Visibility Impairment in Class I Areas of the Western United States. *J. Geophys. Res.* 114: D02308.

Kim, B.J., Kemme, M.R., Rood, M,J., Du, K. (2008). *Development of Emission Factors for Dust Generated by Unique Military Activities (SI-1400): Rotary Wing Aircraft. Annual Report for SERDP.*

Mitchell, W.J., and J.C. Suggs (1998). *Emission Factors for the Disposal of Energetic Materials by Open Burning and Open Detonation (OB/OD); EPA/600/R-98/103.*

Montgomery, D.C., and G.C. Runger (2011). Applied Statistics and Probability for Engineers. 5th ed. John Wiley & Sons, Inc.

NOAA (2010). Weather. http://www.noaa.gov/wx.html. (Accessed February 2018).

USEPA (2000). Meteorological Monitoring Guidance for Regulatory Modeling Applications.

USEPA (2016). Emissions Factors & AP 42, Compilation of Air Pollutant Emission Factors. http://www.epa.gov/ttnchie1/ap42. (Accessed July 2016).

Upadhyay, J.K., Auvermann, B.W., Paila, A.N., and Hiranuma, N. (2008). Open-path Transmissometry to Determine Atmospheric Extinction Efficiency Associated with Feedyard Dust. *Trans. ASABE* 51: 1433–1441.

Watson, J.G. and Chow, J.C. (2000). *Reconciling Urban Fugitive Dust Emissions Inventory and Ambient Source Contribution Estimates: Summary of Current Knowledge and Needed Research. DRI Document No. 6110.4F*.

CHAPTER 4: LIDAR EQUATION INVERSION METHODS AND UNCERTAINTIES IN MEASURING FUGITIVE PARTICULATE MATTER EMISSION FACTORS[3]

4.1 Abstract

Measurements from two field campaigns that employed a micropulse lidar are used to compare the near-end and the far-end lidar equation inversion methods for estimating emission factors (EFs) of particulate matter (PM) from three types of anthropogenic fugitive sources: vehicles moving on unpaved roads, open burning, and open detonation. As optical depth increased from 0 to 2, relative EF uncertainty increased from 54% to 300% using the near-end method and decreased from 69% to 42% using the far-end method. This research is the first time to use field measurements to compare results from these methods for anthropogenic PM plumes and quantify their uncertainties.

4.2 Introduction

Particulate matter (PM) is an air pollutant (USEPA, 2016a; WHO, 2006) that adversely affects human health (Dockery and Pope, 1994; Pope and Dockery, 2006), reduces visibility (Malm, 1999), and affects climate (Boucher et al., 2013). Therefore, identifying source contributions to ambient PM concentrations is important. Fugitive PM, which is defined as PM emitted from unconfined sources (e.g., unpaved roads and agricultural tilling) (USEPA, 2016b; Watson and Chow, 2000), is estimated to contribute 89% of the total primary mass emissions of PM with diameters ≤ 10 μm (PM_{10}) (Watson and Chow, 2000), but accurate quantification of such contribution is challenging because fugitive PM emissions are ubiquitous and vary spatially and temporally, resulting in highly uncertain fugitive PM emission estimates (Yuen et al., 2015, 2014). Optical remote sensing (ORS), described by Du et al. (Du et al., 2011), offers advantages

[3] Reprinted, with permission and minor revisions, from Yuen, W., Ma, Q., Koloutsou-vakakis, S., Du, K., and Rood, M.J. (2017). Lidar Equation Inversion Methods and Uncertainties in Measuring Fugitive Particulate Matter Emission Factors. *Appl. Opt.* 56: 7691–7701.

for the quantification of PM emission factors (EFs) because it quantifies PM plume cross-sections in a short time interval (< 20 s) by measuring range-resolved light extinction coefficients. This method is based on using micropulse lidar (MPL) to quantify PM_{10} emissions (Campbell et al., 2002; Du et al., 2011; Yuen et al., 2015, 2014).

The goals of this research are to improve the current understanding of the MPL-based ORS method in calculating PM_{10} mass EFs and their uncertainties. We focus on: 1) comparison of two lidar equation inversion methods (referred to as inversion methods below), namely the near-end and the far-end methods, to retrieve extinction coefficients to determine EFs; and 2) quantification of uncertainties in estimating these fugitive PM EFs when using the MPL-based ORS method and each inversion method. Fixed extinction profiles in vertical, horizontal, and slant directions, determined by the MPL using the far-end method, have been compared with in-situ measurements from an observatory (Welton et al., 2000). Studies have also compared different inversion methods, considering vertical lidar scans of ambient PM and gases with relatively low extinction coefficients (order of $10^{-4} – 10^{-3}$ m^{-1}) (Böckmann et al., 2004; Yoon et al., 2008). By comparison, the new results reported here are with regard to extinction profiles that are scanned between horizontal and slant directions, have short plume durations (30 – 90 s), and have high extinction coefficients (order of $10^{-3} – 10^{-2}$ m^{-1}). Lidars have been used in previous research to map the spatial and temporal distributions of fugitive PM plumes (Holmén et al., 1998; Marchant et al., 2009; Moore et al., 2013). However, the effects of inversion method on the PM EF estimates have not been examined before with such plumes. Our research is the first to evaluate with field data the impact of the near-end and the far-end methods on the resulting fugitive PM EFs from sources such as moving vehicles on unpaved roads, open burning, and open detonation, as well as to identify the sources of fugitive PM EF measurement

uncertainties and quantify their contributions to uncertainty of the ORS method in quantifying PM EFs from such sources.

ORS has high potential for characterizing fugitive PM emission sources. The results from this research are important because: 1) they demonstrate that the choice of the inversion method can considerably affect the PM EF estimates and their uncertainties, from measurements of concentrated fugitive PM plumes generated at the surface of the Earth; 2) the results of the uncertainty calculations can be used to provide guidance relevant to reducing PM EF uncertainties to improve PM EF inventory data quality; and 3) the calculated uncertainties for this ORS method provide a benchmark for comparing the uncertainties with other ORS fugitive PM EF measurement methods.

4.3 Methods

Data Sources

This research analyzes ORS data from two field campaigns that measured fugitive PM EFs generated by: 1) moving vehicles on unpaved roads (Yuen et al., 2015), and 2) open burning (OB) and open detonation (OD) of energetic materials (Yuen et al., 2014). For all of these PM plumes, EFs are estimated using two inversion methods, and their corresponding uncertainties are estimated. For OB plumes, only the EFs are reported for both inversion methods because there are not enough data to provide a meaningful statistical analysis (which will be further explained in "Uncertainty Analysis" Section). Nevertheless, the OB plumes are important to include here because this is the first set of OB PM EF measurements where the effects of the two inversion methods are investigated.

Details of the field campaigns and the MPL-based ORS method have been published previously in the peer-reviewed literature (Yuen et al., 2015, 2014). In brief, temporally and spatially resolved extinction coefficients are calculated from the backscattered signals that are

received by a vertically scanning MPL as its green laser light (527 nm) passes through individual fugitive PM plumes, and are integrated at 1 Hz. The range resolution of the MPL is 15 m, which was the best resolution for this MPL at the time of these studies. This MPL is now available with improved resolution which is recommended for future measurements. A wire mesh, located behind the plumes (500 – 700 m away from the MPL), is used as a reflective target to measure total light transmittance at the horizontal level; the transmittance allows conversion of the MPL signals into extinction coefficients (Du et al., 2011). Extinction coefficients are converted to PM_{10} mass concentrations through the use of PM_{10} mass extinction efficiency (MEE) values, which are determined by collocated measurements of PM_{10} mass concentration and light extinction coefficient (Hashmonay et al., 2009; Yuen et al., 2015, 2014). Wind speeds and directions are measured by anemometers at 1 Hz and at multiple heights.

EF Calculation Comparison Based on Differences in Inversion Methods

The flowchart that describes the calculation method of EFs for fugitive PM sources is shown in Figure 4.1 (Du et al., 2011; Yuen et al., 2014). The raw MPL backscatter values are first corrected and normalized to provide normalized relative backscatter (NRB) signals (Eq. (4.1)) (Campbell et al., 2002):

$$\mathrm{NRB}(x) = \frac{\left\{p_{raw}(x) \cdot D_c\left[p_{raw}(x)\right] - p_{dc}(x) - p_{ap}(x) - p_{bg}\right\} x^2}{E \cdot O(x)} \qquad (4.1)$$

where: $p_{raw}(x)$ = raw MPL signal at distance x (photon count/(μs)(pulse)); $D_c[p_{raw}(x)]$ = dead-time correction of the raw MPL signal; $p_{dc}(x)$ = dark count MPL signal at distance x; $p_{ap}(x)$ = afterpulse MPL signal at distance x; p_{bg} = background light MPL signal; E = output pulse energy of the MPL laser; and O(x) = overlap correction factor at distance x.

Figure 4.1. Flowchart describing how emission factors (EFs) are calculated for fugitive PM sources.

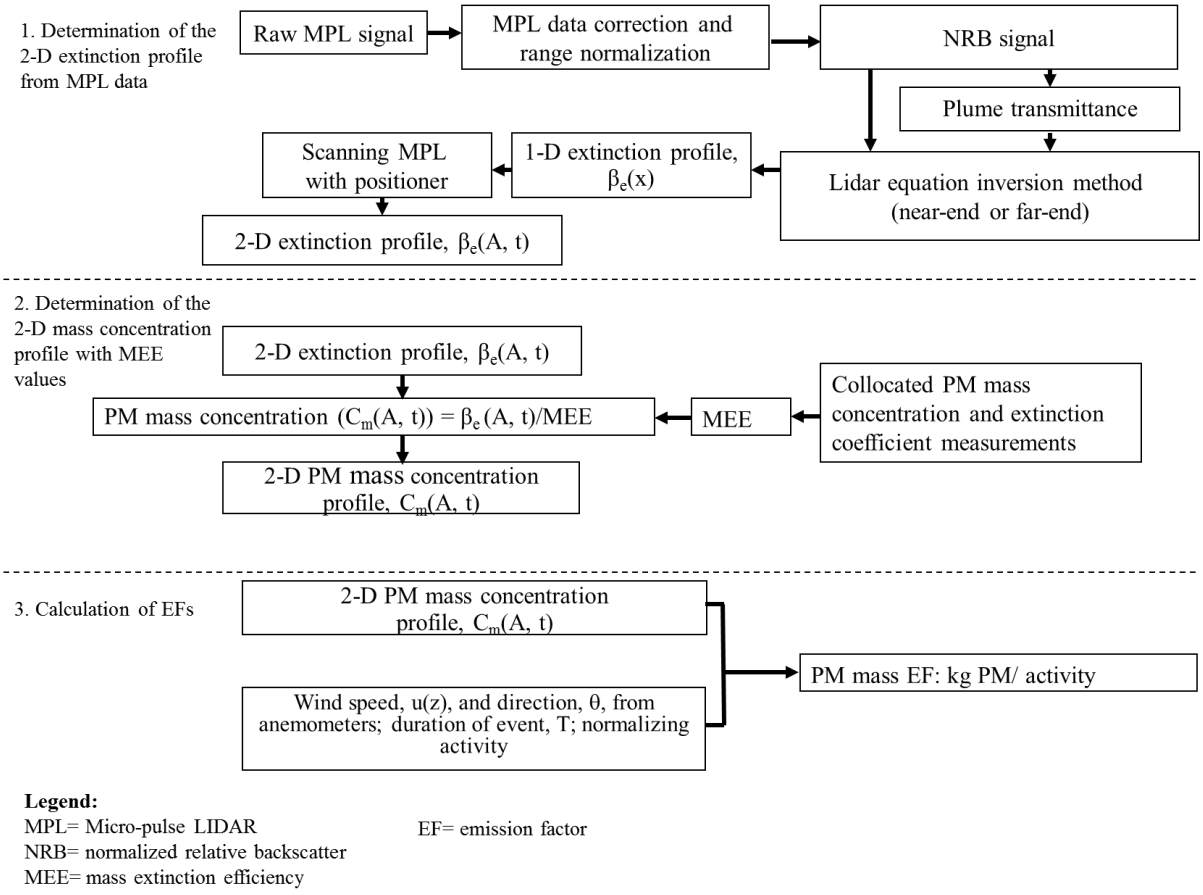

All corrections are determined with established procedures (Campbell et al., 2002; Du et al., 2011), except for p_{bg}. In (Campbell et al., 2002), p_{bg} is measured by the MPL directed vertically into the atmosphere, from signals between 40 and 55 km in altitude, where the PM and gas extinction coefficients are negligible. In the field campaigns reported here, measurements occur in the lower atmosphere, where background PM and gas extinction coefficients cannot be assumed to be zero, and other objects such as trees and hills are in the near proximity (< 45 km) and impact the measured signals. Thus, p_{bg} is interpreted as raw signal when the plume is absent between the MPL and the reflective target, i.e., as raw signal due to background PM and gas. Such interpretation of p_{bg} is applied to the field campaign measurements in (Yuen et al., 2015, 2014).

NRB signals are then converted to extinction coefficients through an inversion method based on the single-scatter lidar equation (Du et al., 2011). In the earlier research, the near-end method is used, where the extinction coefficient calculation begins at the lidar, and continues away from the lidar (Eq. (4.2)). The equation is based on the near-end method developed by Fernald et al. (Fernald et al., 1972), modified by Du et al. (Du et al., 2011):

$$\beta_e(x_j) = \frac{NRB(x_j)}{K^* - 2\sum_{k=1}^{j} NRB(x_k)\Delta x} \tag{4.2}$$

where: $\beta_e(x_j)$ = extinction coefficient at distance x_j, which is the distance from the lidar at bin j (distance x_1 is the closest distance from the lidar); $NRB(x_j)$ = normalized relative backscatter signal at x_j; K^* = lidar system constant that was determined by the lidar system properties divided by the PM's extinction-to-backscatter ratio (Du et al., 2011); and Δx = spatial resolution of lidar, with distances x_j and x_{j+1}, separated by Δx.

In this research, the far-end method is also considered, where extinction coefficient calculations begin from a location where the lidar's light passes through the far end of the plume, moving to distances closer to the lidar (Eq. (4.3)). The equation is based on the far-end method developed by Klett (Klett, 1981):

$$\beta_e(x_j) = \frac{NRB(x_j)}{K^* T^2(x_c) + 2\sum_{k=j}^{c} NRB(x_k)\Delta x} \tag{4.3}$$

where: x_c = the farthest distance from the lidar that acts as a calibration point (15 to 45 m before the reflective target at the horizontal level); and $T^2(x_c)$ = two-way transmittance from the lidar at x_c. The distance x_c cannot be set exactly at the reflective target from the MPL (x_t) because the NRB signal at the calibration point should only include the background PM and gas, but the NRB signal at x_t includes the signal from the reflective target.

Extinction profiles and K* are calculated by solving a system of equations, Eq. (4.2) or Eq. (4.3), where j is from 1 to c, and Eq. (4.4) that relates $T^2(x_c)$ and $\beta_e(x)$ by Beer-Lambert Law, at all distances between 0 and x_c, with NRB(x), $T^2(x_c)$, and Δx as inputs (Du et al., 2011). $T^2(x_c)$ relates to the plume's optical depth, τ, (Eq. (4.4)), which is the product of path length and extinction coefficient, the latter of which relates to PM mass concentration of the plume.

$$T^2\left(x_c\right) = \frac{NRB\left(x_t\right)_{plume\_present}}{NRB\left(x_t\right)_{plume\_absent}} = \exp\left(-2\tau\right) = \exp\left[-2\Delta x\sum_{i=1}^{c}\beta_e\left(x_i\right)\right] \quad (4.4)$$

When the MPL scans at the horizontal level, $T^2(x_c)$ is determined by using the NRB signal at x_t, when the plume is present ($NRB(x_t)_{plume\_present}$) and absent ($NRB(x_t)_{plume\_absent}$) (Eq. (4.4)). The calculation assumes that the total transmittance between x_c and x_t is one, which is a good assumption because the distance between x_c and x_t is 15 – 45 m, and literature shows that the total transmittance is 0.998 in the ambient atmosphere at a path length of 50 m (Du et al., 2009). When the MPL scans at the elevated levels, the reflective target is not available for calculating $T^2(x_c)$. $T^2(x_c)$ is thus calculated by using K* calculated for the horizontal-level measurement, and assuming that K* measured at the horizontal level is applicable to the elevated levels. Then, the systems of equations mentioned above are solved numerically, with NRB(x), K*, and Δx as inputs, and $\beta_e(x)$ and $T^2(x_c)$ as outputs. K* calculated from the method above assumes that K* is constant spatially and temporally. In reality, however, the differences in particle properties within a plume may result in variable K* values. Such K* variation is analyzed as K* uncertainty.

PM_{10} mass concentration profiles are then determined by the extinction profiles and PM_{10} MEE values. PM_{10} MEE values are determined using extinction coefficients measured at the same location as the mass concentration measurement (Hashmonay et al., 2009; Yuen et al.,

2015, 2014). PM_{10} EFs are then calculated by integrating the plume's range-resolved PM_{10} mass concentration profiles with wind speed and direction, duration of event, and source characterization (i.e., distance for a specific moving vehicle type or mass of energetic material) (Eq. (4.5)):

$$EF = \frac{1}{Y}\sum_{t=0}^{T}\left[\sum C_m(\Delta A, t)u(z)\cos\theta\Delta A\right]\Delta t \quad (4.5)$$

where: Y = activity of the source (e.g., distance travelled by vehicle or mass of energetic material); T = duration of the event; $C_m(\Delta A, t) = PM_{10}$ mass concentration at differential area ΔA at time t; u(z) = wind speed at height z; θ = angle between the wind direction and the normal direction to the ORS observing plane during that event; and Δt = differential time. For the rest of the paper, EF in the equation means PM_{10} EF.

By their mathematical formulation, the far-end method offers an advantage over the near-end method because the near-end method (Eq. (4.2)) can become mathematically unstable when the denominator approaches zero or becomes negative (Klett, 1981). In Eq. (4.2), K* is constant but the summation of NRB signals in the denominator increases, since all NRB signals are positive. When the summation of NRB signals increases to approach K*, the denominator of Eq. (4.2) approaches zero, leading to extinction coefficient approaching infinity. When the summation of NRB signals is larger than K*, the denominator of Eq. (4.2) becomes negative, yielding negative extinction coefficients that are invalid (Klett, 1981). In the far-end method (Eq. (4.3)), the denominator of the equation is always positive, thus there is no instability issue as with the near-end method.

Uncertainty Analysis

In our previous research, initial uncertainties of MEE, wind speed, and wind direction values are discussed with a recommendation to provide a more rigorous uncertainty analysis as

future research (Du et al., 2011). In this research, extinction profiles (related to NRB(x) and K*), MEE, and wind factor that considers wind speed and wind direction are studied more rigorously for their contributions to PM_{10} EF uncertainty. Uncertainty analysis is performed for both the near-end and the far-end methods for comparison purposes. The uncertainties of PM_{10} EFs (δEFs) are calculated by performing error propagation on the equations in Figure 4.1. The error propagation method is based on the first order term of the Taylor series expansion (Ku, 1966). In this research, δEFs are analyzed for one small τ plume and one large τ plume for the moving vehicle sources, as well as a plume for the OD source. As previously mentioned, the PM_{10} EF uncertainty of OB is not analyzed because K* values from only two measurements are available, which is not enough to provide meaningful statistics for the uncertainty analysis.

NRB Signal Uncertainties (δNRB)

δNRB(x) was calculated using Eq. (4.6) (Welton and Campbell, 2002):

$$\delta NRB(x) = NRB(x)\sqrt{\frac{\left[\delta p_{raw}(x)\right]^2 + \delta p_{bg}{}^2 + \left[\delta p_{ap}(x)\right]^2}{\left[p_{raw}(x) - p_{bg} - p_{ap}(x)\right]^2} + \left(\frac{\delta E}{E}\right)^2 + \left[\frac{\delta O(x)}{O(x)}\right]^2} \qquad (4.6)$$

where: δ = uncertainty (standard deviation) of a parameter.

Several assumptions are used to calculate δNRB(x) (Welton and Campbell, 2002). The uncertainty of dead-time correction is determined to be negligible, based on the uncertainty analysis of this correction factor determination method that uses the ratios between the calibration signals and the observed signals (Welton and Campbell, 2002). The uncertainty of dark count is assumed to be zero, since the dark count itself is negligible (three orders of magnitude smaller than p_{bg}, as determined in our field measurements). The relative uncertainty of output pulse energy (δE/E) is determined to be 1% because this uncertainty depends on the temperature fluctuation of the MPL, but when MPL signals are collected at < 1 min interval, the

temperature fluctuation is negligible (Welton and Campbell, 2002). Although the overlap correction factor increases with increasing distance when the distance is < 1 km, the relative uncertainty of overlap correction factor ($\delta O(x)/O(x)$) is estimated to be constant at 3%, when the plume is between 300 m and 500 m from the MPL (Welton and Campbell, 2002). This distance range is chosen because plumes are located between 150 m and 500 m from the MPL in our measurements. Lastly, uncertainties of $p_{raw}(x)$, $p_{ap}(x)$, and p_{bg} are calculated, assuming they followed the Poisson distribution (Welton and Campbell, 2002). Thus:

$$\delta p = \sqrt{\frac{p}{N\Delta t_x}} \tag{4.7}$$

where: $p = p_{raw}(x)$, $p_{ap}(x)$, or p_{bg}; N = total number of pulses within the integration time of MPL signals; and Δt_x = pulse traveling time for two-way range resolution distance (i.e., $\Delta t_x = 2\Delta x/c$, where c = speed of light). N equals 2,500 when the MPL integration time is 1 s, as reported in its manual. For a 15-m range resolution of MPL, $\Delta t_x = 0.1$ μs.

Relative Uncertainties of Extinction Profiles ($\delta\beta_e(x)/\beta_e(x)$)

After finding δNRB for each measurement point (Eq. (4.6)), error propagation is performed on the near-end (Eq. (4.8)) and the far-end (Eq. (4.9)) methods, similar to the method in (Rocadenbosch et al., 2010), to find the relative extinction profile uncertainties of each measurement point ($\delta\beta_e(x)/\beta_e(x)$):

$$\frac{\delta\beta_e(x_j)}{\beta_e(x_j)} = \left(\left\{ \frac{2\Delta x \beta_e(x_j)}{NRB(x_j)} \sqrt{\sum_{k=1}^{j-1} \left[\delta NRB(x_k)\right]^2} \right\}^2 + \left\{ \left[\frac{1}{NRB(x_j)} - \frac{2\Delta x \beta_e(x_j)}{NRB(x_j)} \right] \delta NRB(x_j) \right\}^2 + \left[\frac{\beta_e(x_j)}{NRB(x_j)} \delta K^* \right]^2 \right)^{\frac{1}{2}} \tag{4.8}$$

$$\frac{\delta\beta_e(x_j)}{\beta_e(x_j)}=\left(\left\{\frac{2\Delta x\beta_e(x_j)}{NRB(x_j)}\sqrt{\sum_{k=j+1}^{c}\left[\delta NRB(x_k)\right]^2}\right\}^2+\left\{\left[\frac{1}{NRB(x_j)}-\frac{2\Delta x\beta_e(x_j)}{NRB(x_j)}\right]\delta NRB(x_j)\right\}^2\right.$$
$$\left.+\left[\frac{\beta_e(x_j)}{NRB(x_j)}T(x_c)^2\,\delta K^*\right]^2+\left[\frac{\beta_e(x_j)}{NRB(x_j)}K^*\delta T^2(x_c)\right]^2\right)^{\frac{1}{2}} \quad (4.9)$$

where: δK^* = uncertainties of K^*, calculated by the standard deviation of K^* for all plumes of the same source; and $\delta T^2(x_c)$ = uncertainty of two-way transmittance, calculated by using the uncertainties of NRB signals (Eq. (4.6)), based on error propagation of Eq. (4.4).

$$\delta T^2(x_c)=T^2(x_c)\sqrt{\left[\frac{\delta NRB(x_t)_{plume\_absent}}{NRB(x_t)_{plume\_absent}}\right]^2+\left[\frac{\delta NRB(x_t)_{plume\_present}}{NRB(x_t)_{plume\_present}}\right]^2} \quad (4.10)$$

The relative extinction coefficient uncertainty increases with the extinction coefficient in Eq. (4.8) and (4.9). Since extinction coefficient can approach infinity when the near-end method is unstable, the relative extinction coefficient uncertainty becomes infinite as well. Thus, in theory, the near-end method gives higher relative extinction coefficient uncertainty than the far-end method, when the near-end method becomes unstable.

Uncertainties of PM_{10} EF (δEF)

PM_{10} δEF value is then determined by Eq. (4.11), after $\delta\beta_e(x)/\beta_e(x)$ at each measurement point is calculated.

$$\delta EF=\frac{1}{Y}\sum_{t=0}^{T}\left(\sum C_m(\Delta A,t)\,u(z)\cos\theta\,\Delta A\right.$$
$$\left.\sqrt{\left(\frac{\delta MEE}{MEE}\right)^2+\left\{\frac{\delta\left[u(z)\cos\theta\right]}{u(z)\cos\theta}\right\}^2+\left[\frac{\delta\beta_e(\Delta A,t)}{\beta_e(\Delta A,t)}\right]^2}\right)\Delta t \quad (4.11)$$

where: $\delta MEE/MEE$ = relative uncertainty of MEE value; and $\delta[u(z)\cos(\theta)]/u(z)\cos(\theta)$ = relative uncertainty of wind factor value ($u(z)\cos(\theta)$). Relative EF uncertainty ($\delta EF/EF$) is calculated by

dividing δEF by EF. The two relative uncertainties are determined by the coefficient of variation (COV, i.e., standard deviation / mean x 100%) of their corresponding measurements in field campaigns. The statistics of MEE values are obtained from replicate measurements for each source type, each at the same location. This means that MEE values are assumed not to be varied spatially. In contrast, the statistics of wind factor values are obtained from anemometer measurements for each plume at multiple heights, so the effect of heights on wind factor values is considered.

The relative uncertainties for Y, ΔA, and Δt are not considered in uncertainty calculations because these uncertainties are much lower than the ones introduced by inversion method, wind speed, and MEE. The relative uncertainties for Y, ΔA, and Δt are < 5%, < 1%, and < 1%, respectively. The relative uncertainties for Y and Δt are determined by the means and the standard deviations of the Y and MPL's scanning time measurements, respectively. The relative uncertainty for ΔA is determined by expressing ΔA as a function of MPL's range resolution and scanning angle, applying error propagation on it, and using the means and the standard deviations of these two parameters to calculate the relative uncertainty for ΔA.

Effect of τ on δEF/EF by Simulation

Since the most concentrated part of the plume generated by a moving vehicle is observed at the horizontal level (Figure 4.2), horizontal-level MPL measurements are used to examine the effect of the magnitude of τ on δEF/EF. Different τ values are simulated by treating the NRB signals as surrogates for τ values and multiplying NRB values by multipliers, resulting in τ values between 0 and 2. The two inversion methods (either Eq. (4.2) or (4.3), where j is from 1 to c) and Beer-Lambert Law (Eq. (4.4)) are then used to calculate τ and δEF/EF.

Assessment of Contributions to δEF

The percent contributions to δEF due to MEE values ($\%\delta EF_{MEE}$), wind factor values ($\%\delta EF_{wind}$), and 2-D extinction profiles ($\%\delta EF_{\beta e}$) are calculated by Eqs. (4.12), (4.13), and (4.14), respectively. Both the numerator and denominator are squared because of the error propagation method that we use.

$$\%\delta EF_{MEE} = \frac{\left\{\frac{1}{Y}\sum_{t=0}^{T}\left[\sum C_m(\Delta A,t)\,u(z)\cos\theta\Delta A\left(\frac{\delta MEE}{MEE}\right)\right]\Delta t\right\}^2}{\delta EF^2}\,x100\% \tag{4.12}$$

$$\%\delta EF_{wind} = \frac{\left[\frac{1}{Y}\sum_{t=0}^{T}\left(\sum C_m(\Delta A,t)\,u(z)\cos\theta\Delta A\left\{\frac{\delta\left[u(z)\cos\theta\right]}{u(z)\cos\theta}\right\}\right)\Delta t\right]^2}{\delta EF^2}\,x100\% \tag{4.13}$$

$$\%\delta EF_{\beta e} = \frac{\left(\frac{1}{Y}\sum_{t=0}^{T}\left\{\sum C_m(\Delta A,t)\,u(z)\cos\theta\Delta A\left[\frac{\delta\beta_e(\Delta A,t)}{\beta_e(\Delta A,t)}\right]\right\}\Delta t\right)^2}{\delta EF^2}\,x100\% \tag{4.14}$$

4.4 Results and Discussion

EF Calculation Comparison Based on Differences in Inversion Methods

One small τ (τ = 0.15 in Figure 4.2 (F2)) and one large τ (τ = 1.29 in Figure 4.3 (F2)) plumes, generated by moving vehicles on unpaved roads, are used as representative conditions to demonstrate the differences in PM_{10} EFs using the near-end and the far-end methods. Examples of successive 2-D extinction coefficient profiles, at 10 s intervals, calculated by the near-end and the far-end methods, are shown in Figures 4.2 and 4.3, for the small and the large τ plumes, respectively. PM_{10} EF statistics for the small and the large τ plumes are shown in Figure 4.4. In generating both plumes, the vehicle travelled parallel to the vertical scanning plane and toward the MPL, resulting in plumes moving primarily along the horizontal level, as shown in Figures 4.2 and 4.3. As mentioned in the "Methods" Section, the mathematical instability issue of the

near-end method leads to negative extinction coefficient values. This can be observed in Figure 4.3, where negative extinction coefficients with the near-end method are calculated at further distances away from the MPL (> 340 m in the horizontal level for the Figure 4.3 (N2) profile and > 240 m in the horizontal level for the Figure 4.3 (N3) profile) for the large τ plume. In the horizontal level, the small τ and the large τ plumes have 0% and 30% of the extinction coefficients calculated to be negative, respectively, for the near-end method. There are 0% negative extinction coefficients calculated by the far-end method.

Figure 4.2. Example light extinction profiles for a small τ plume generated by a moving vehicle (τ = 0.15, at horizontal level for Figure 4.2 (F2)), calculated by the near-end (N) and the far-end (F) methods. Profiles are 10 s apart. The highest dash line of the profiles corresponds to the highest vertical scanning position of the MPL.

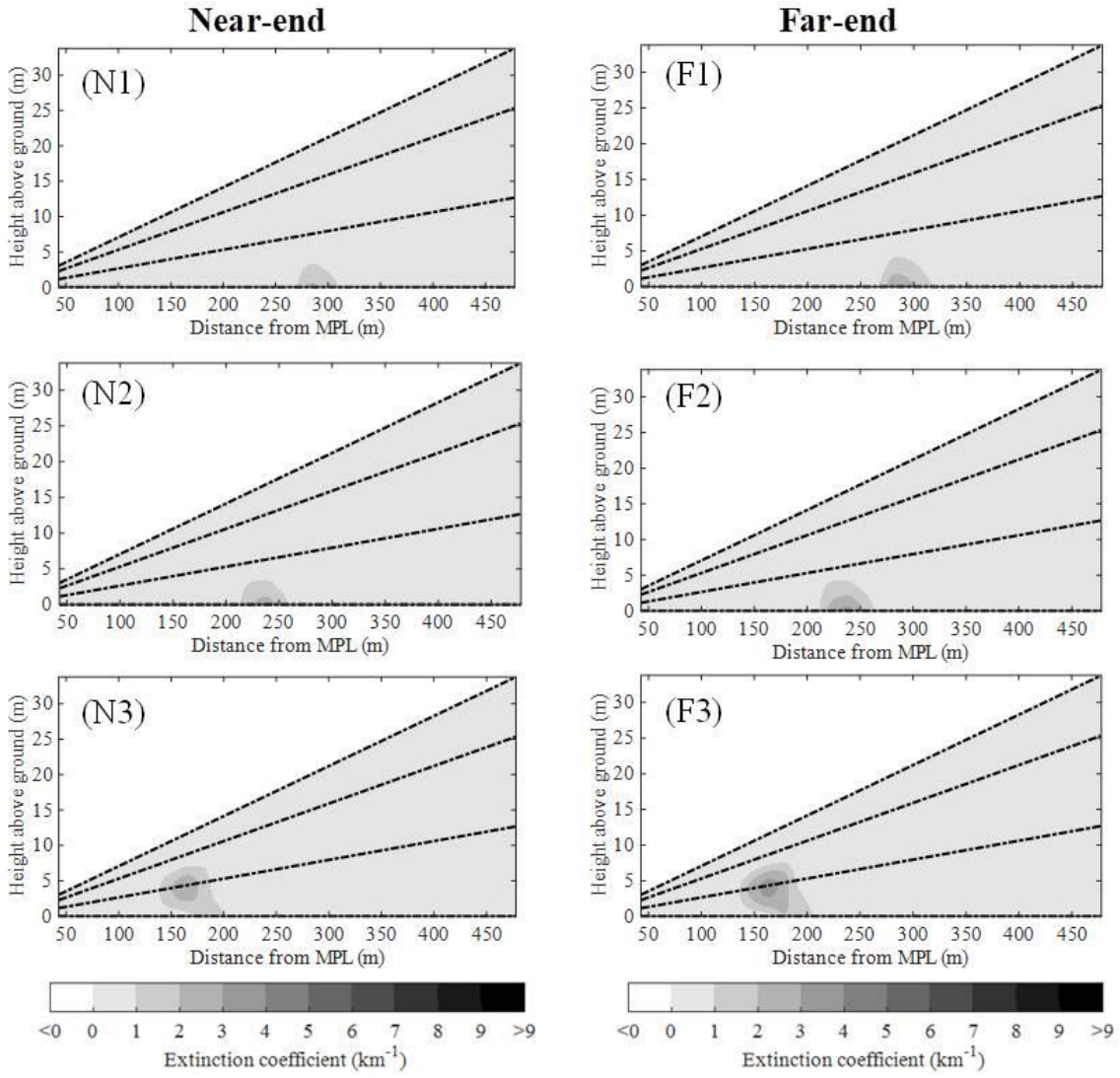

Figure 4.3. Example light extinction profiles for a large τ plume generated by a moving vehicle (τ = 1.29, at horizontal level for Figure 4.3 (F2)), calculated by the near-end (N) and the far-end (F) methods. Profiles are 10 s apart. The highest dash line of the profiles corresponds to the highest vertical scanning position of the MPL.

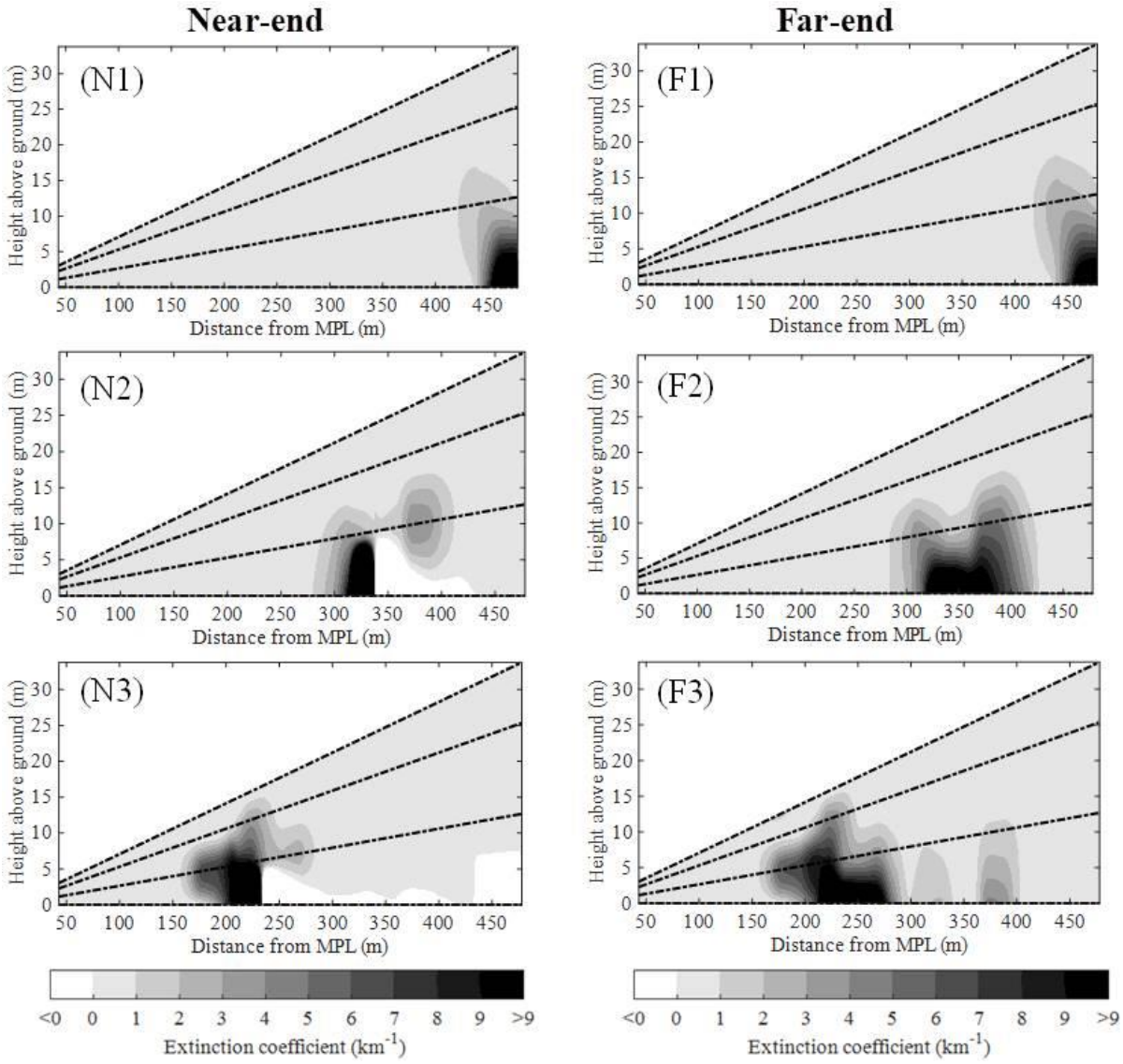

Figure 4.4. Emission factors (EFs, vertical bar) and their uncertainties (δEFs, vertical lines) for the small τ plume (τ = 0.15, at horizontal level for Figure 4.2 (F2)) and the large τ plume (τ = 1.29, at horizontal level for Figure 4.3 (F2)) generated by vehicles travelling on unpaved roads, calculated by the near-end and the far-end methods.

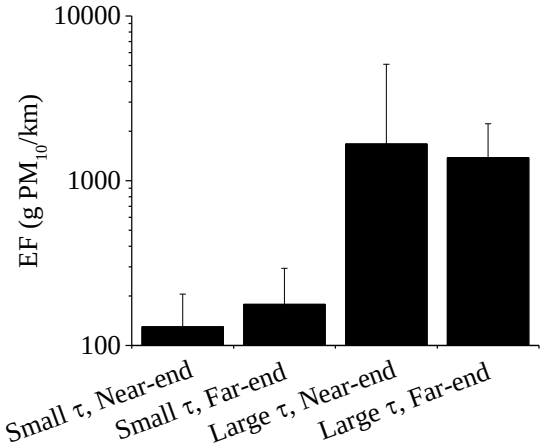

The resulting PM_{10} EFs are 130 g PM_{10}/km for the near-end method and 178 g PM_{10}/km for the far-end method for the small τ plume (Figure 4.2), with a -27% relative difference (($EF_{near\text{-}end}$ - $EF_{far\text{-}end}$) / $EF_{far\text{-}end}$ x 100%). The resulting PM_{10} EFs are 1,673 g PM_{10}/km for the near-end method and 1,379 g PM_{10}/km for the far-end method for the large τ plume (Figure 4.3), with a 21% relative difference. However, for the large τ plume, the relative difference is estimated without including the extinction profiles where the negative extinction coefficients are produced by the near-end method. Thus, the relative difference in EF between the two inversion methods would be much greater than 21% for the large τ plume, if the negative extinction coefficients by the near-end method are included for the comparison.

Statistical results comparing the near-end and the far-end methods for all the PM_{10} plumes for the tracked and wheeled vehicles are summarized in Table 4.1. PM_{10} EFs are normalized by vehicle momentum to account for vehicle speed and mass (Yuen et al., 2015). The p-values for all site and vehicle types examined, using two-sample t-test (Montgomery and

Runger, 2011), are > 0.05, which indicate that the normalized PM_{10} EF between the near-end and the far-end methods have no significant differences at 95% confidence.

Table 4.1. Comparison statistics for PM_{10} emission factors (EFs) calculated with the near-end and the far-end methods for all tracked and wheeled vehicle plumes. EFs are normalized by vehicle momentum.

Site and vehicle type (Yuen et al., 2015)			Site 1 Tracked	Site 2 Tracked	Site 2 Wheeled
PM_{10} EF / vehicle momentum [(g PM_{10}/km) / (kg m/s)]	**Near-end (Yuen et al., 2015)**	**Mean**	0.004	0.009	0.009
		Standard deviation	0.003	0.004	0.007
		Number of samples	38	9	15
	Far-end	**Mean**	0.004	0.012	0.006
		Standard deviation	0.003	0.006	0.004
		Number of samples	38	9	15
p-value			1.00	0.23	0.16

Similar analyses and comparisons are done for representative OB and OD events. Examples of successive 2-D extinction profiles, at 10 s intervals, calculated by the near-end and the far-end methods, are shown in Figures 4.5 and 4.6, for the OB and the OD plumes, respectively. PM_{10} EF statistics for the OB and the OD plumes are shown in Figure 4.7. Unlike the moving vehicle events, the sources of the OB and OD plumes do not move to or away from the MPL, and their plumes are primarily aloft, as shown in Figures 4.5 and 4.6. The 2-D extinction profiles for the near-end method show smaller extinction coefficients than for the far-end method, and smaller PM_{10} EFs of 5.3×10^{-3} kg PM_{10} / kg net explosive weight (NEW) for the near-end method compared to 6.1×10^{-3} kg PM_{10} / kg NEW for the far-end method (Figure 4.7), for the plume generated by an OB event (Figure 4.5). This is a -13% EF relative difference when using the far-end method as the reference. The 2-D extinction profiles for the near-end method also show smaller extinction coefficients than for the far-end method, and smaller PM_{10} EFs of

0.30 kg PM_{10} / kg NEW for the near-end method compared to 0.32 kg PM_{10} / kg NEW for the far-end method (Figure 4.7), for a plume generated by an OD event (Figure 4.6). This is a -6% EF relative difference when using the far-end method as the reference. Both OB and OD plumes have 0% negative extinction coefficients using either inversion method.

Figure 4.5. Example light extinction profiles for a plume generated by open burning (OB), calculated by the near-end (N) and the far-end (F) methods. Profiles are 10 s apart. The highest dash line of the profiles corresponds to the highest vertical scanning position of the MPL.

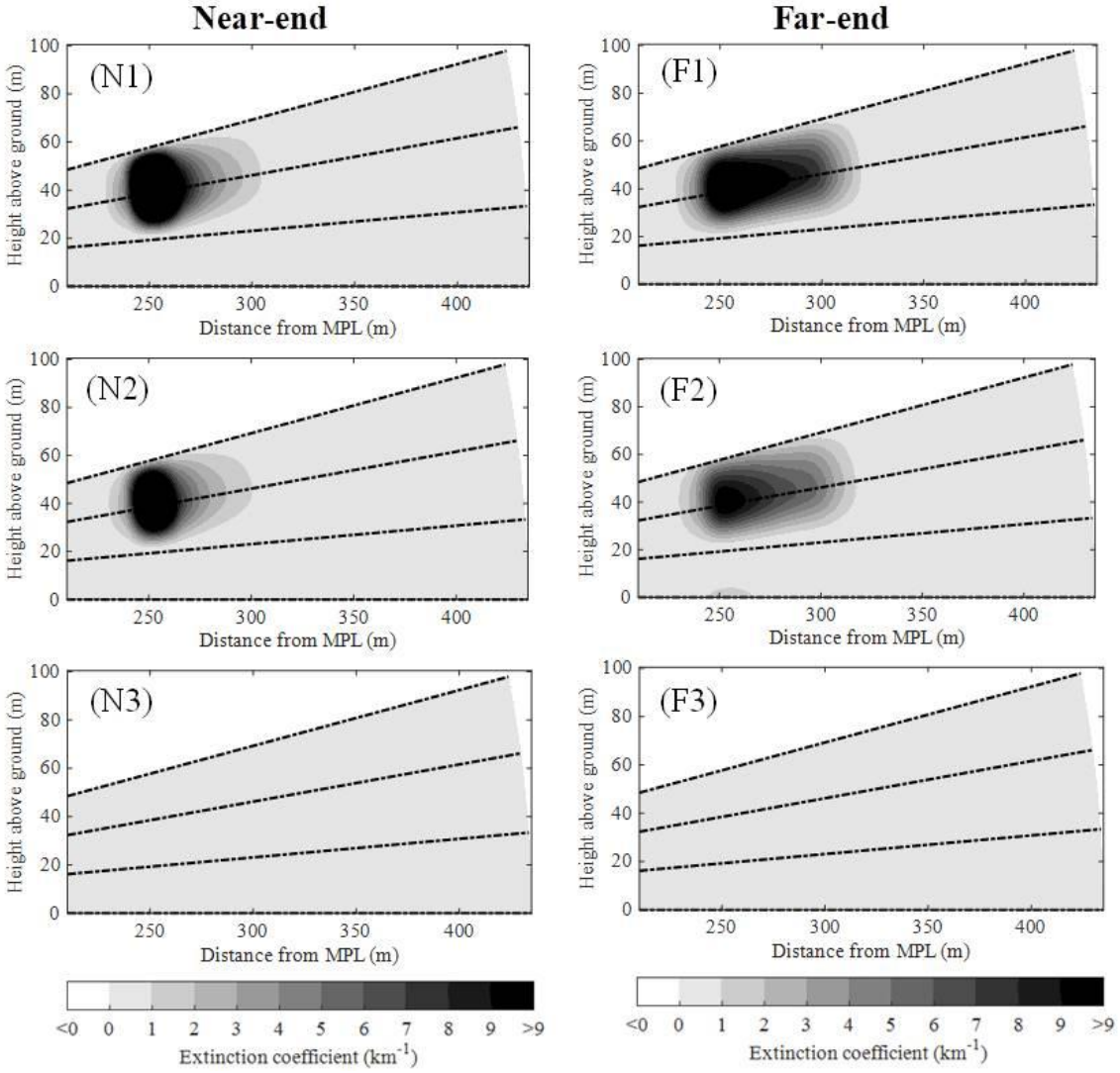

Figure 4.6. Example light extinction profiles for a plume generated by open detonation (OD), calculated by the near-end (N) and the far-end (F) methods. Profiles are 10 s apart. The highest dash line of the profiles corresponds to the highest vertical scanning position of the MPL.

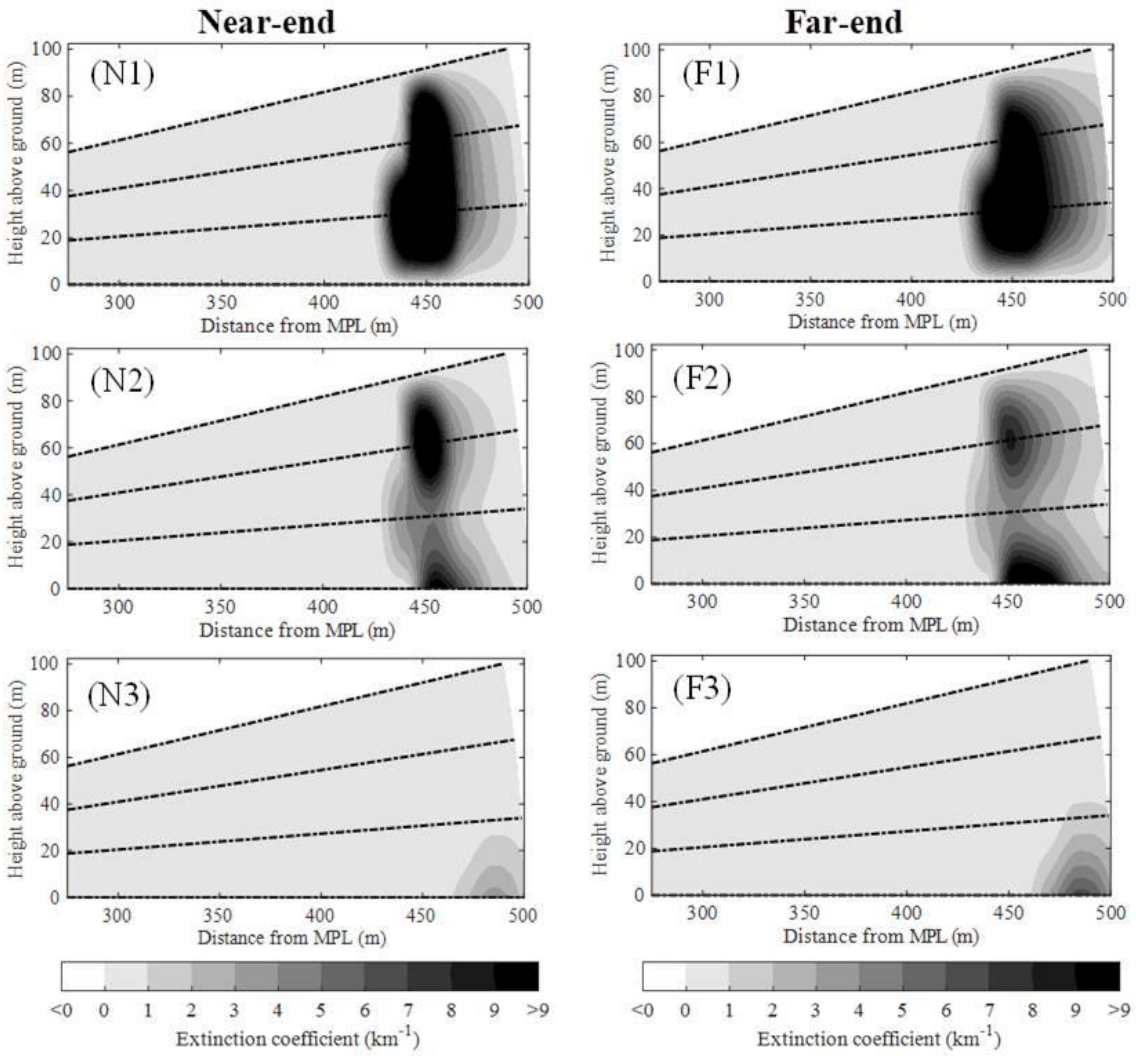

Figure 4.7. Emission factors (EFs, vertical bar) and their uncertainties (δEFs, vertical lines) for the plumes generated by an OB and an OD events, calculated by the near-end and the far-end methods. The EF uncertainty of the OB plume is not shown due to K* values from a small number of measurements (2) to calculate uncertainties.

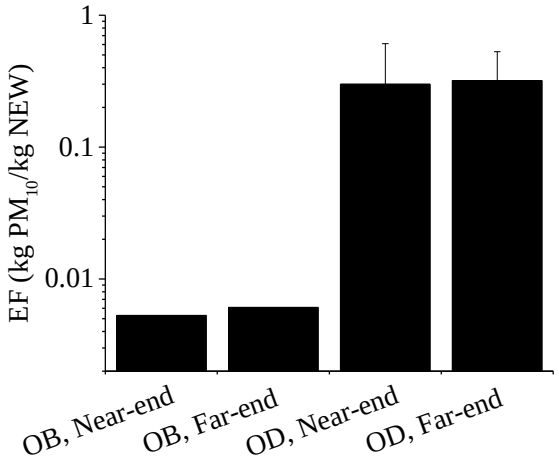

Statistical results comparing the near-end and the far-end methods for all of the plumes caused by the OB and OD events are summarized in Table 4.2. The p-values that compare the two inversion methods for the OB and OD events are all > 0.05, which indicate that the PM_{10} EF between the near-end and the far-end methods have no significant differences.

Table 4.2. Comparison of statistics for PM_{10} emission factors (EFs) calculated with the near-end and the far-end methods for all open burning (OB) and open detonation (OD) events in the field campaign previously reported in (Yuen et al., 2014).

Source type			OB	OD
PM_{10} EF (kg PM_{10} / kg NEW)	**Near-end (Yuen et al., 2014)**	**Mean**	7.8×10^{-3}	0.20
		Standard deviation	4.4×10^{-3}	0.11
		Number of samples	37	24
	Far-end	**Mean**	8.8×10^{-3}	0.21
		Standard deviation	4.5×10^{-3}	0.12
		Number of samples	37	24
p-value			0.33	0.77

NEW = net explosive weight

Based on the above results, the fugitive PM plumes are non-uniform spatially and temporally for moving vehicle, OB, and OD sources, as demonstrated by the extinction profiles in Figures 4.2, 4.3, 4.5, and 4.6. The PM_{10} EFs for moving vehicle, OB, and OD sources between

the near-end and the far-end methods are not statistically different, provided that negative extinction coefficients resulting from the near-end method are ignored for high τ plumes. Based on the results presented here, it is preferable to use the far-end method in calculating extinction coefficients from the NRB signals for high τ plumes. The difference between the two methods becomes smaller for low τ cases, such as cases where lidars have been employed for measuring τ along vertical columns in the ambient atmosphere.

Uncertainty Analysis

This uncertainty analysis describes NRB, extinction, and PM_{10} EF uncertainties for representative plumes. The relationship between relative PM_{10} EF uncertainty and τ is then described to show the difference of uncertainty behavior between the near-end and the far-end methods. Factors that contribute to the overall PM_{10} EF uncertainties are then discussed.

NRB Signal Uncertainties (δNRB)

An example of the NRB signals, their uncertainties (δNRB), and relative uncertainties (δNRB/NRB) for a horizontal-level MPL measurement of a plume from a moving vehicle is shown in Figure 4.8, for a representative MPL scan. In Figure 4.8, the NRB signals indicate detection of the plume between 250 m and 400 m from the MPL. Detection of the plume occurs when NRB ≥ 0.11, the limit of detection of the MPL, which is 3 times the standard deviation of 15 NRB signals when the plume is not detected (Currie, 1968). At NRB detection levels, δNRB/NRB = 3%, since δNRB/NRB is dominated by the overlap correction uncertainty (3%), rather than by the pulse energy uncertainty (1%) and by the raw MPL signal uncertainty (0.2%-2%). Absence of the plume (NRB < 0.11) results in δNRB/NRB > 3%, since the raw MPL signal uncertainty increases to become dominant, resulting in an increase of δNRB/NRB. However, since the uncertainties of PM_{10} EFs also depend on extinction coefficients at each point (Eq. (4.11)), plume-absent areas contribute negligibly (<1%) to δEF.

Figure 4.8. Relationships between NRB signals, δNRB, and δNRB/NRB of a horizontal-level scan by MPL for a large τ plume (Figure 4.3 (F2)).

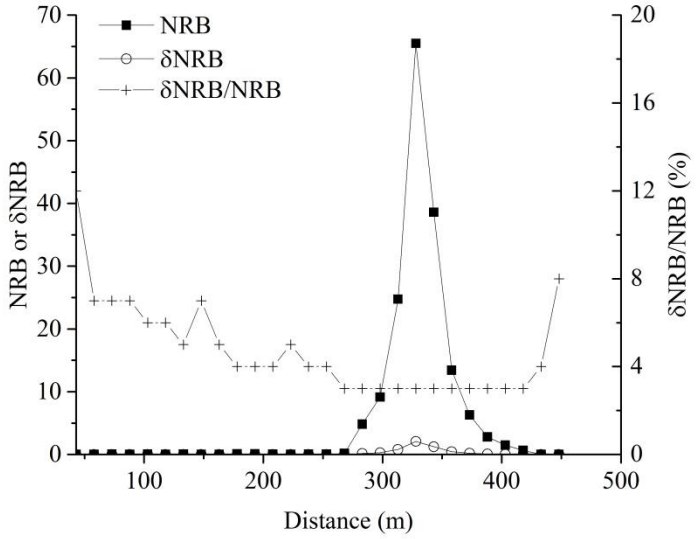

Relative Uncertainties of Extinction Profiles (δβe(x)/βe(x))

$\delta\beta_e(x)/\beta_e(x)$ profiles are calculated for a small and a large τ plumes generated by moving vehicles corresponding to Figures 4.2 and 4.3, respectively, and are shown in Figures 4.9 and 4.10. $\delta\beta_e(x)/\beta_e(x)$ values increase with increasing distance from the MPL. As expected, where the unstable near-end method produces negative $\beta_e(x)$ values in Figure 4.10, $\delta\beta_e(x)/\beta_e(x)$ values also become negative. For the small τ plume, all $\delta\beta_e(x)/\beta_e(x)$ values are >10% using either method. For the large τ plume, the $\delta\beta_e(x)/\beta_e(x)$ values are >10% for most $\delta\beta_e(x)/\beta_e(x)$ values for either method (93% of values for the near-end method, 89% of values for the far-end method). This shows that δNRB/NRB values of 3% do not dominate $\delta\beta_e(x)/\beta_e(x)$ values.

Figure 4.9. Example relative uncertainty profiles of light extinction coefficients ($\delta\beta_e(x)/\beta_e(x)$) for a small τ plume generated by a moving vehicle ($\tau = 0.15$, at horizontal level for Figure 4.2 (F2)), calculated by the near-end (N) and the far-end (F) methods. Profiles are 10 s apart. The highest dash line of the profiles corresponds to the highest vertical scanning position of the MPL.

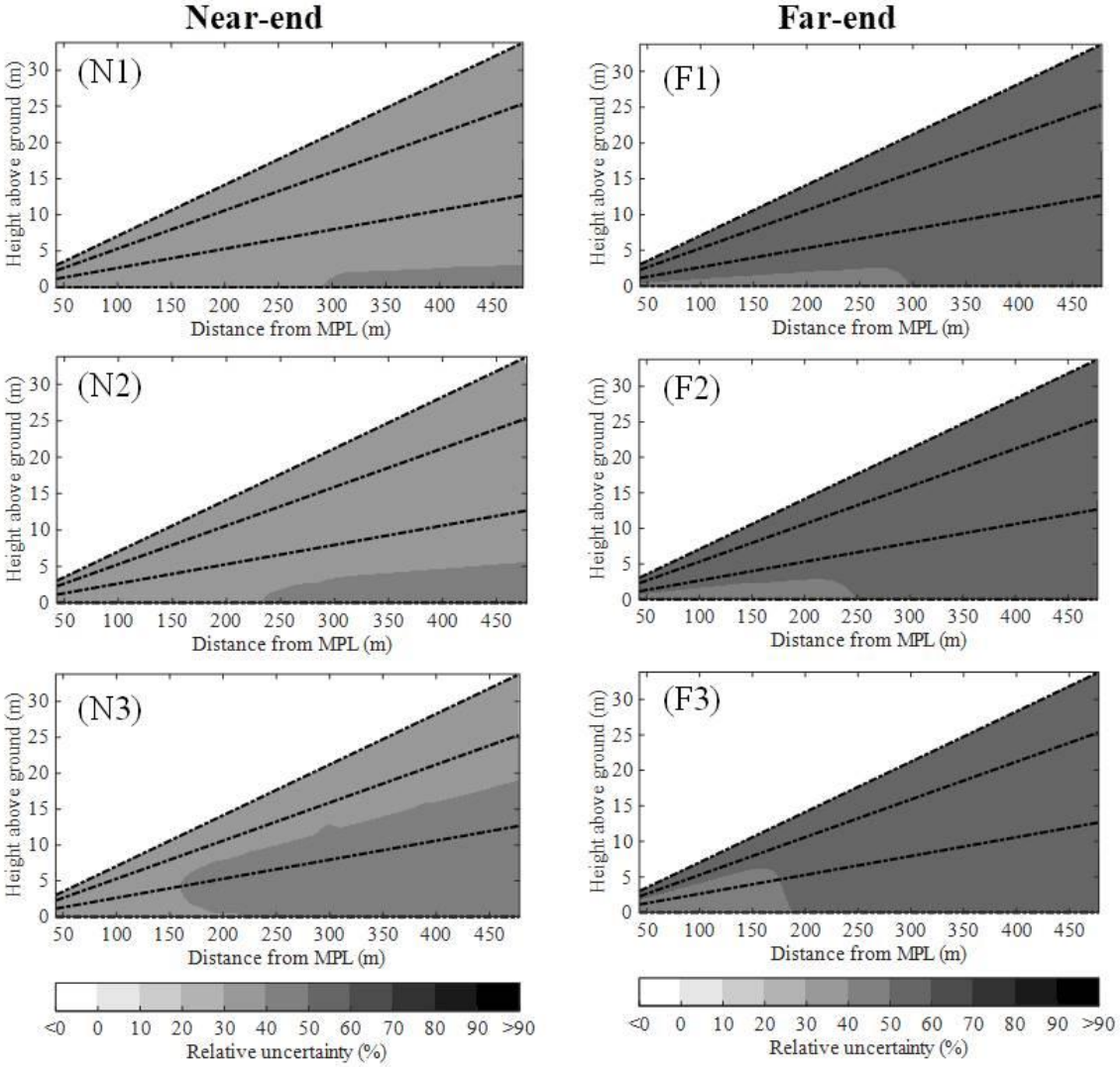

Figure 4.10. Example relative uncertainty profiles of light extinction coefficients ($\delta\beta_e(x)/\beta_e(x)$) for a large τ plume generated by a moving vehicle (τ = 1.29, at horizontal level for Figure 4.3 (F2)), calculated by the near-end (N) and the far-end (F) methods. Profiles are 10 s apart. The highest dash line of the profiles corresponds to the highest vertical scanning position of the MPL.

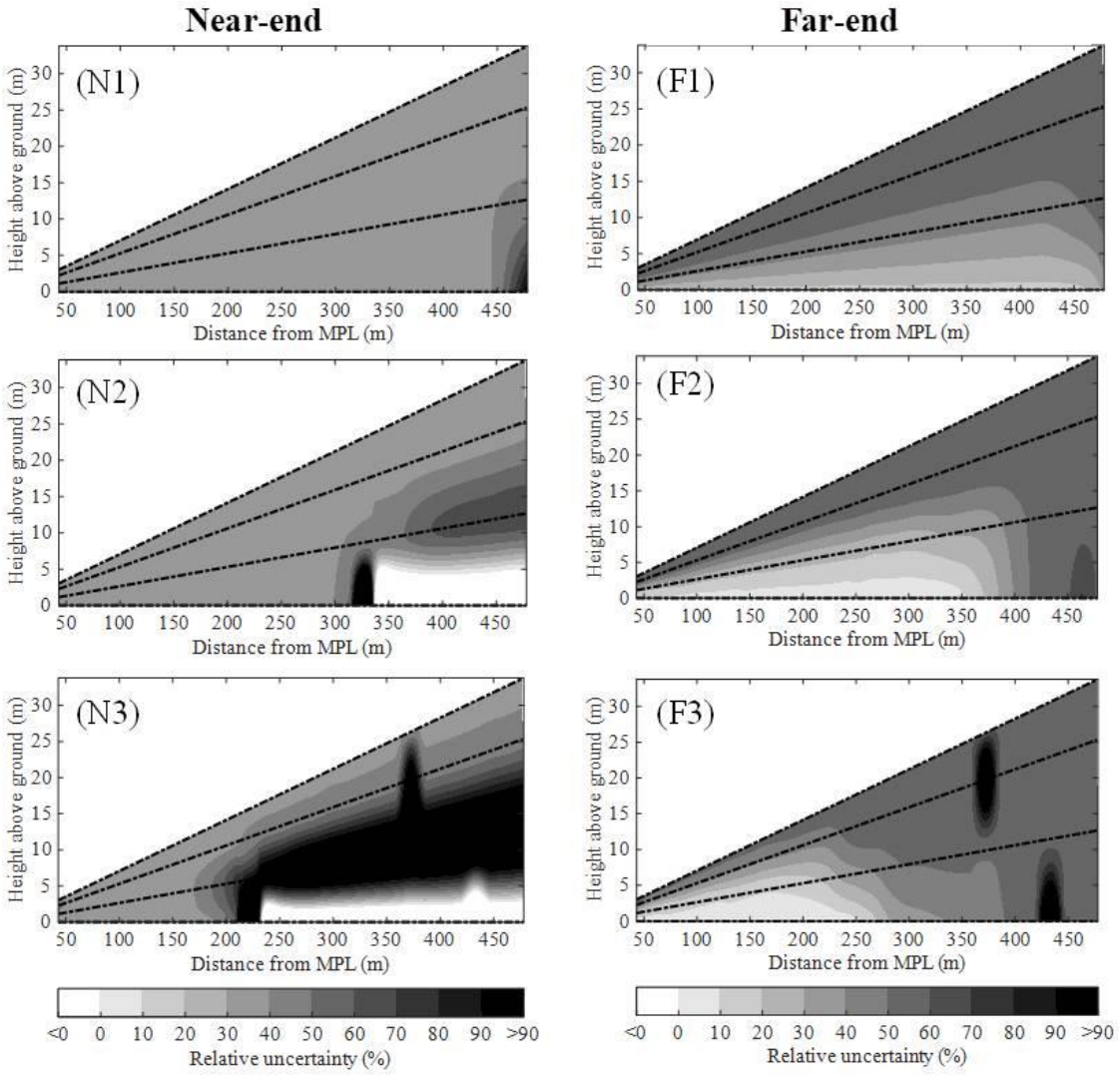

For the small τ plume, $\delta\beta_e(x)/\beta_e(x)$ values for the near-end method are lower than the far-end method by -22% to 0% as differences between $\delta\beta_e(x)/\beta_e(x)$ (i.e., $\delta\beta_e(x)/\beta_e(x)$ by the near-end method minus $\delta\beta_e(x)/\beta_e(x)$ by the far-end method), with a mean of -18%. The $\delta\beta_e(x)/\beta_e(x)$ profiles have similar shapes between the near-end and the far-end methods (Figure 4.9). In contrast, for the large τ plume, $\delta\beta_e(x)/\beta_e(x)$ calculated by the near-end method differ from the far-end method by -22% to 375% with a mean of 6%. The values of $\delta\beta_e(x)/\beta_e(x)$ for the near-end

method increase more rapidly than those for the far-end method with increasing distance from the MPL (Figure 4.10).

Comparisons of $\delta\beta_e(x)/\beta_e(x)$ profiles in Figure 4.10 (N3) and (F3) demonstrate two types of abrupt $\delta\beta_e(x)/\beta_e(x)$ changes. The first type occurs for the near-end method at 220 m from the MPL (Figure 4.10 (N3)), where $\delta\beta_e(x)/\beta_e(x)$ value increases rapidly with distance from the MPL, and then abruptly decreases to negative values, coinciding with the negative values of $\beta e(x)$, consistent with the respective profile shown in Figure 4.3 (N3). The second type occurs for both the near-end and the far-end methods at 370 m and 430 m from the MPL (Figure 4.10 (N3) and Figure 4.10 (F3)). In this case, $\delta\beta_e(x)/\beta_e(x)$ value increases rapidly in scanned areas where the plume is absent (Figure 4.3 (N3) and (F3)), and the NRB values are near zero (<0.0001). The reason for the second type of abrupt change is due to higher δNRB/NRB values (>150%) when the NRB values are closer to zero (Figure 4.8), which leads to high $\delta\beta_e(x)/\beta_e(x)$ values based on the second terms of Eqs. (8) and (9). Comparisons of the range of values on the $\delta\beta_e(x)/\beta_e(x)$ differences and the profiles in Figures 4.9 and 4.10 show that $\delta\beta_e(x)/\beta_e(x)$ for the near-end method is more sensitive to τ values than for the far-end method.

$\delta\beta_e(x)/\beta_e(x)$ for the OD plume corresponding to Figure 4.6 are shown in Figure 4.11. $\delta\beta_e(x)/\beta_e(x)$ also increases with increasing distance from the MPL when using either the near-end or the far-end method. The $\delta\beta_e(x)/\beta_e(x)$ values are >10% for most $\delta\beta_e(x)/\beta_e(x)$ values for either method (100% of values for the near-end method, 90% of values for the far-end method). $\delta\beta_e(x)/\beta_e(x)$ calculated by the near-end method differ from those calculated by the far-end method, by -4% to 96% (differences calculated as above) and a mean of 5% for this plume.

Figure 4.11. Example relative uncertainty profiles of light extinction coefficients ($\delta\beta_e(x)/\beta_e(x)$) for a plume generated by open detonation (OD), calculated by the near-end (N) and the far-end (F) methods. Profiles are 10 s apart. The highest dash line of the profiles corresponds to the highest vertical scanning position of the MPL.

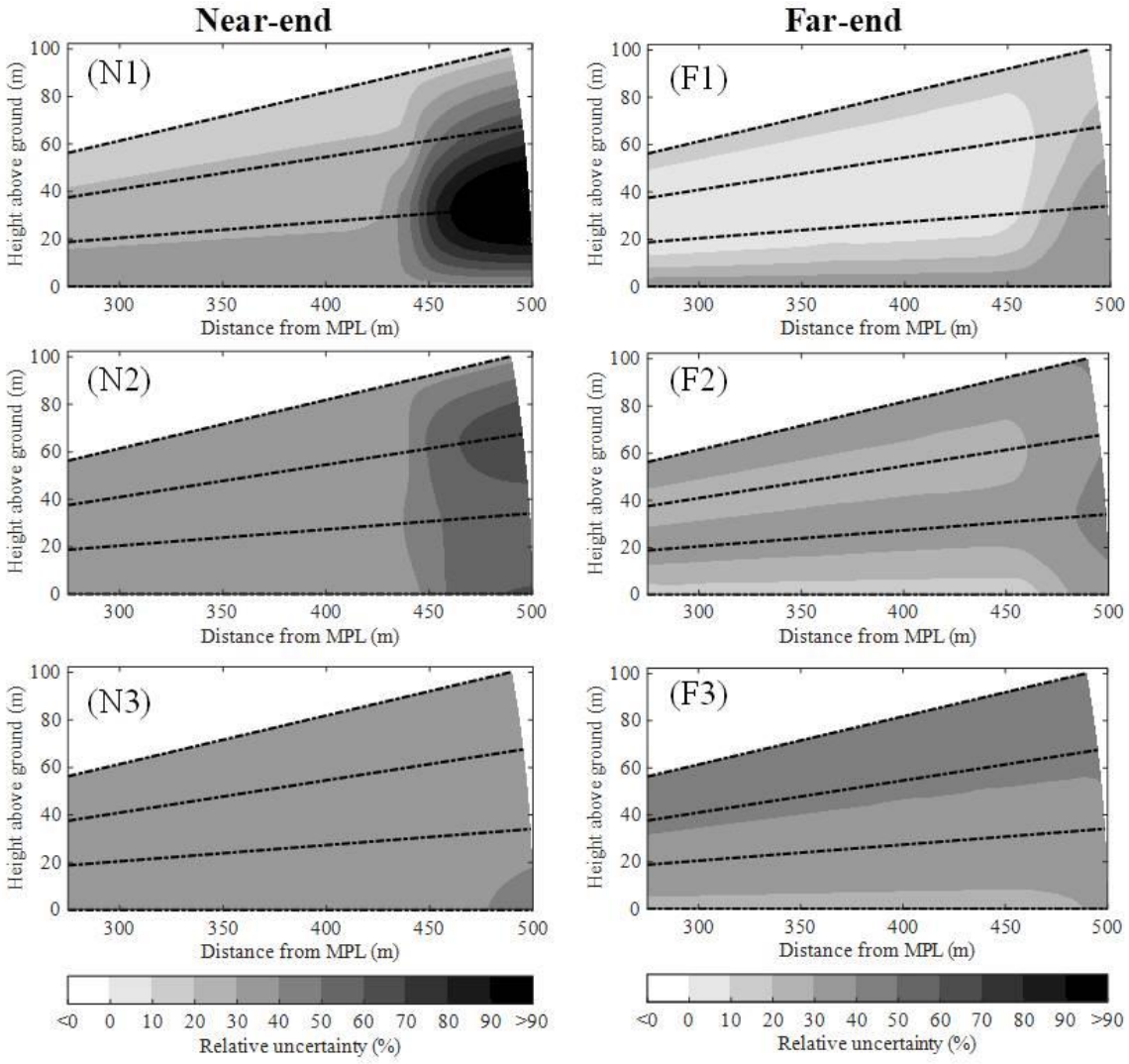

Uncertainties of PM_{10} EF (δEF)

The resulting δEF values for plumes emitted from a moving vehicle with small and large τ values have been shown in Figure 4.4, and δEF values for one OD plume have been shown in Figure 4.7, as vertical lines. For the small τ plume generated by the moving vehicle, the δEF/EF value is 58% using the near-end method, which is smaller than 65% using the far-end method. For the large τ plume generated by the moving vehicle, the δEF/EF value is 204% using the near-

end method, which is larger than 61% using the far-end method. For OD, the near-end method results in higher δEF/EF of 103%, compared to 66% for the far-end method. The above results show that δEF/EF is at least 58% when analyzing the δEF/EF from all field measurements in this study, which is important as a quantification of the ORS method uncertainty. The δMEE/MEE values are 31% for moving vehicles and 23% for OD on average, while the $\delta[u(z)\cos(\theta)]/u(z)\cos(\theta)$ values are 50% for moving vehicles and 55% for OD on average. These two relative uncertainties that are used to calculate δEF/EF are not affected by the inversion methods.

Effect of τ on δEF/EF by Simulation

Results describing the dependence of δEF/EF on τ when using the near-end and the far-end methods are shown in Figure 4.12. A representative NRB profile taken from the horizontal-level measurement of the large τ plume for the moving vehicle (Figure 4.2 (F2)) was chosen for this analysis. Results using the near-end method show that when τ values increase from 0 to 2, δEF/EF values increase from 54% to 300%. In contrast, δEF/EF values using the far-end method are less sensitive to τ, with δEF/EF values for the same condition decreases from 69% to 42%. The reason for lower sensitivity to τ is that the $\delta\beta_e(x)/\beta_e(x)$ profiles for the far-end method are less sensitive to τ values.

Figure 4.12. Relationship between relative PM_{10} emission factor uncertainty (δEF/EF) at horizontal-level and optical depth (τ) for the near-end and the far-end methods. Lines of τ = 0.15 for small τ plume and τ = 1.29 for large τ plume for the moving vehicles are shown for reference.

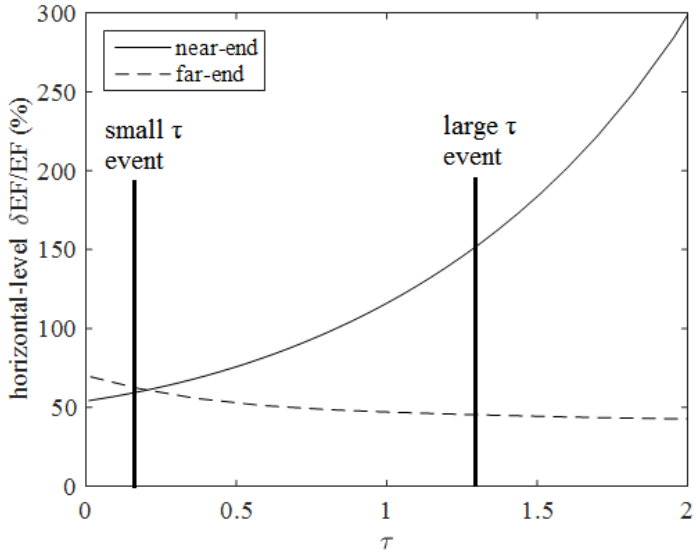

Assessment of Contributions to δEF

$\%\delta EF_{MEE}$, $\%\delta EF_{wind}$, and $\%\delta EF_{\beta e}$ for plumes generated by a moving vehicle with small and large τ values (Figures 4.2 and 4.3, respectively), and a plume generated by an OD event (Figure 4.6), are shown in Figure 4.13 (A). For the near-end method, $\%\delta EF_{\beta e}$ is the largest (47% for the small τ plume generated by the moving vehicle, 94% for the large τ plume generated by the moving vehicle, and 64% for the OD plume). For the far-end method, $\%\delta EF_{\beta e}$ is lower (25% for the large τ plume generated by the moving vehicle and 11% contribution for the OD plume), except for the small τ plume generated by the moving vehicle (58%). Seeing that the relative uncertainties of MEE and wind factor are not affected by the change in inversion methods, change of $\%\delta EF_{\beta e}$ suggests change due to $\delta\beta_e(x)/\beta_e(x)$. In other words, changing from the near-end method to the far-end method reduces the uncertainties of the 2-D extinction profiles.

Relationship between δEF/EF and $\%\delta EF_{\beta e}$ for the six event-method combinations shown in Figure 4.13 (A) is shown in Figure 4.13 (B). Based on these six event-method combinations, δEF/EF increases with increasing $\%\delta EF_{\beta e}$ when $\%\delta EF_{\beta e}$ is >60%, but levels between 42% and

69% when $\%\delta EF_{\beta e}$ is ≤60%. Thus, to further reduce δEF/EF that is determined by the far-end method, the uncertainties of MEE values and the wind factor values need to be reduced. Reducing the uncertainties of these parameters is challenging because: 1) the measurements of MEE values in our method assume that the particle properties (e.g., particle size distribution) are constant across the plume and throughout the duration of the plume event, but this may not be the case because of the heterogeneities of the plumes over time, which require more elaborate field setup to measure MEE values at multiple points, making measurement more complex and expensive; and 2) the uncertainties of wind factor values are challenging to be controlled in the outdoor ambient environment because of the stochastic nature of micrometeorology.

Figure 4.13. (A) Comparisons of the percent contributions of PM_{10} EF uncertainties (δEF) due to the 2-D extinction profiles, the MEE values, and the wind factor values, for the small τ and the large τ moving vehicle plumes and the OD plume in Figures 4.2, 4.3, and 4.6, respectively, calculated by the near-end and the far-end methods. (B) Relationship between δEF/EF and $\%\delta EF_{\beta e}$ by plotting each point corresponding to each bar in (A).

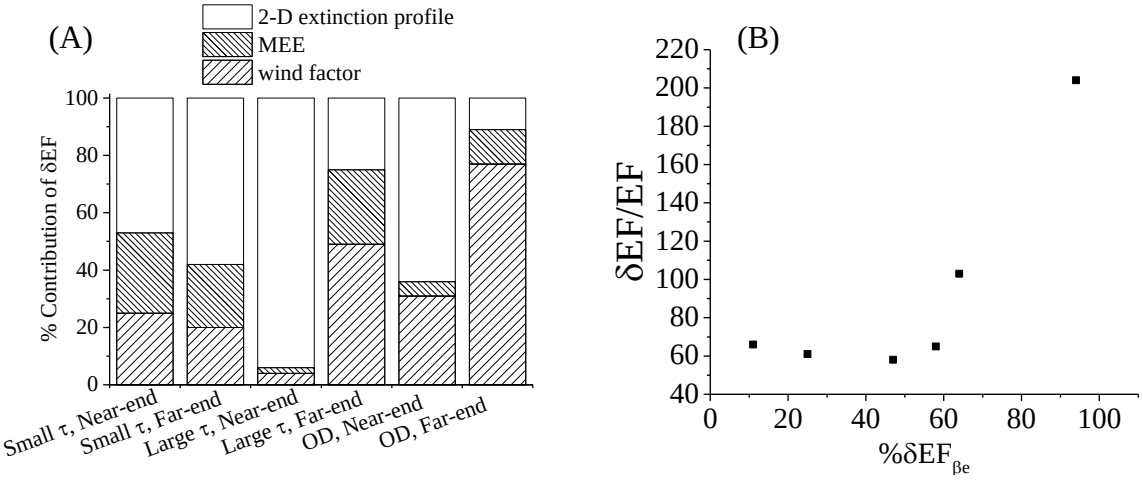

4.5 Conclusions

Plumes of fugitive particulate matter (PM), measured by optical remote sensing (ORS) with micropulse lidar (MPL), are analyzed using two different lidar equation inversion methods. The comparison of inversion methods demonstrates that although the near-end and the far-end

methods yield PM_{10} emission factors (EFs) that are not significantly different (Table 4.1), such PM_{10} EFs do not account for the negative extinction coefficients by the near-end method at large optical depth (τ) plumes, due to its inherent instability (30% of extinction coefficients in the plume events examined are negative by the near-end method, compared to 0% by the far-end method). When using the near-end method, the relative uncertainty of PM_{10} EFs ($\delta EF/EF$) values increases from 54% to 300% as plume τ values increase from 0 to 2. In contrast, when using the far-end method and the same plume τ values, the change in $\delta EF/EF$ values is smaller (from 69% to 42%, as τ values increase). Results support that the far-end method is preferable because: 1) this method does not demonstrate instability (also discussed with simulations in (Klett, 1981)), resulting in negative extinction coefficients; and 2) $\delta EF/EF$ values are less sensitive to the value of τ.

The uncertainty analysis also shows that changing from the near-end method to the far-end method can reduce 2-D extinction profile uncertainty, and subsequently $\delta EF/EF$ values, when the plume has high τ values. However, further reduction of $\delta EF/EF$ values is more challenging for the far-end method, since the MEE and wind factor uncertainties are larger. Reducing the latter two uncertainties are more challenging because MEE values and their uncertainties within the plume may have spatial and temporal variation, and wind factor uncertainty is difficult to control outdoors.

This research is the first time to use full-scale field data for concentrated fugitive PM plumes (extinction coefficients in the order of $10^{-3} – 10^{-2}$ m^{-1}), emitted from anthropogenic activities near ground level, to compare the performance and the uncertainty of the ORS method with the near-end and far-end methods, for two different sources of fugitive PM_{10}. The relative contributions of the major sources of uncertainties to overall uncertainty are also identified for

the first time. These results show that choice of inversion method is important when using the ORS method for estimating EFs for fugitive PM sources. Such results provide guidance for improving PM EF inventory data quality that is determined by ORS, and provide a benchmark for comparing the uncertainties with other fugitive PM EF measurement methods.

4.6 Acknowledgements

The authors thank the Department of Defense (DoD) Projects SI-1400 and WP-1672, as well as the Department of Civil and Environmental Engineering Research Experience for Undergraduates (CEE-REU) in the University of Illinois for funding this research.

4.7 References

Böckmann, C., Wandinger, U., Ansmann, A., Bösenberg, J., Amiridis, V., Boselli, A., Delaval, A., De Tomasi, F., Frioud, M., Grigorov, I. V, et al. (2004). Aerosol Lidar Intercomparison in the Framework of the EARLINET Project. 2. Aerosol Backscatter Algorithms. *Appl. Opt.* 43: 977–989.

Boucher, O., Randall, D., Artaxo, P., Bretherton, C., Feingold, G., Forster, P., Kerminen, V.-M., Kondo, Y., Liao, H., Lohmann, U., et al. (2013). *Clouds And Aerosols*. In, Stocker, T.F., D. Qin, G.-K. Plattner, M. Tignor, S.K. Allen, J. Boschung, A. Nauels, Y. Xia,V.B. and P.M.M. (Ed), *Climate Change 2013: the Physical Science Basis. Contribution of Working Group I to the Fifth Assessment Report of the Intergovernmental Panel on Climate Change*. Cambridge University Press, Cambridge, United Kingdom and New York, NY, USA, 571–657.

Campbell, J.R., Hlavka, D.L., Welton, E.J., Flynn, C.J., Turner, D.D., Spinhirne, J.D., Scott, V.S., and Hwang, I.H. (2002). Full-Time, Eye-Safe Cloud and Aerosol Lidar Observation at Atmospheric Radiation Measurement Program Sites: Instruments and Data Processing. *J.*

Atmos. Ocean. Technol. 19: 431–442.

Currie, L.A. (1968). Limits for Qualitative Detection and Quantitative Determination. Application to Radiochemistry. *Anal. Chem.* 40: 586–593.

Dockery, D.W. and Pope, C.A. (1994). Acute Respiratory Effects of Particulate Air Pollution. *Annu. Rev. Public Health* 15: 107–132.

Du, K., Rood, M.J., Kim, B.J., Kemme, M.R., Franek, B., and Mattison, K. (2009). Evaluation of Digital Optical Method to Determine Plume Opacity During Nighttime. *Environ. Sci. Technol.* 43: 783–789.

Du, K., Rood, M.J., Welton, E.J., Varma, R.M., Hashmonay, R.A., Kim, B.J., and Kemme, M.R. (2011). Optical Remote Sensing to Quantify Fugitive Particulate Mass Emissions from Stationary Short-term and Mobile Continuous Sources: Part I. Method and Examples. *Environ. Sci. Technol.* 45: 658–665.

Fernald, F.G., Herman, B.M., and Reagan, J.A. (1972). Determination of Aerosol Height Distributions by Lidar. *J. Appl. Meteorol.* 11: 482–489.

Hashmonay, R.A., Kagann, R.H., Rood, M.J., Kim, B.J., Kemme, M.R., and Gillies, J. (2009). *An Advanced Test Method for Measuring Fugitive Dust Emissions Using a Hybrid System of Optical Remote Sensing and Point Monitor Techniques*. In, Kim,Y.J., Platt,U., Gu,M.B., and Iwahashi,H. (Eds), *Atmospheric and Biological Environmental Monitoring*. Springer Netherlands, 73–81.

Holmén, B.A., Eichinger, W.E., and Flocchini, R.G. (1998). Application of Elastic Lidar to PM_{10} Emissions from Agricultural Nonpoint Sources. *Environ. Sci. Technol.* 32: 3068–3076.

Klett, J.D. (1981). Stable Analytical Inversion Solution for Processing Lidar Returns. *Appl. Opt.* 20: 211–220.

Ku, H.H. (1966). Notes on the Use of Propagation of Error Formulas. *J. Res. Natl. Bur. Stand. Sect. C Eng. Instrum.* 70C: 263–273.

Malm, W.C. (1999). *Introduction to Visibility*. Colorado State University, Fort Collins, CO.

Marchant, C.C., Wilkerson, T., Bingham, G.E., Zavyalov, V. V, Andersen, J.M., Wright, C.B., Cornelsen, S.S., Martin, R.S., Silva, P.J., and Hatfield, J.L. (2009). Aglite Lidar: a Portable Elastic Lidar System for Investigating Aerosol and Wind Motions at or Around Agricultural Production Facilities. *J. Appl. Remote Sens.* 3: 20.

Montgomery, D.C. and Runger, G.C. (2011). *Applied Statistics and Probability for Engineers*. 5th ed. John Wiley & Sons, Inc.

Moore, K.D., Wojcik, M.D., Martin, R.S., Marchant, C.C., Bingham, G.E., Pfeiffer, R.L., Prueger, J.H., and Hatfield, J.L. (2013). Particulate Emissions Calculations from Fall Tillage Operations Using Point and Remote Sensors. *J. Environ. Qual.* 42: 1029–1038.

Pope, C.A. and Dockery, D.W. (2006). Health Effects of Fine Particulate Air Pollution: Lines That Connect. *J. Air Waste Manag. Assoc.* 56: 709–742.

Rocadenbosch, F., Reba, M.N.M., Sicard, M., and Comerón, A. (2010). Practical Analytical Backscatter Error Bars for Elastic One-component Lidar Inversion Algorithm. *Appl. Opt.* 49: 3380–93.

USEPA (2016a). National Ambient Air Quality Standards (NAAQS). https://www.epa.gov/criteria-air-pollutants/naaqs-table (Accessed August 2016).

USEPA (2016b). *Emissions Factors & AP 42, Compilation of Air Pollutant Emission Factors*. http://www.epa.gov/ttnchie1/ap42. (Accessed July 2016).

Watson, J.G. and Chow, J.C. (2000). *Reconciling Urban Fugitive Dust Emissions Inventory and Ambient Source Contribution Estimates: Summary of Current Knowledge and Needed*

Research. DRI Document No. 6110.4F.

Welton, E.J., Voss, K.J., Gordon, H.R., Maring, H., Smirnov, A., Holben, B., Schmid, B., Livingston, J.M., Russell, P.B., Durkee, P.A., et al. (2000). Ground-based Lidar Measurements of Aerosols During ACE-2: Instrument Description, Results, and Comparisons with Other Ground-based and Airborne Measurements. *Tellus B* 52: 636–651.

Welton, E.J. and Campbell, J.R. (2002). Micropulse Lidar Signals: Uncertainty Analysis. *J. Atmos. Ocean. Technol.* 19: 2089–2094.

WHO (2006). *WHO Air Quality Guidelines for Particulate Matter, Ozone, Nitrogen Dioxide and Sulfur Dioxide.* Copenhagen.

Yoon, S., Kim, S., Kim, M., Shimizu, A., and Sugimoto, N. (2008). Ground-Based Mie-Scattering Lidar Measurements of Aerosol Extinction Profiles During ABC-EAREX 2005 : Comparisons of Instruments and Inversion Algorithms. *J. Meteorol. Soc. Japan* 86: 377–396.

Yuen, W., Du, K., Koloutsou-Vakakis, S., Rood, M.J., Kim, B.J., Kemme, M.R., Hashmonay, R.A., and Meister, C. (2015). Fugitive Particulate Matter Emissions to the Atmosphere from Tracked and Wheeled Vehicles in a Desert Region by Hybrid-Optical Remote Sensing. *Aerosol Air Qual. Res.* 15: 1613–1626.

Yuen, W., Johnsen, D.L., Koloutsou-vakakis, S., Rood, M.J., Byung, J., and Kemme, M.R. (2014). Open Burning and Open Detonation PM_{10} Mass Emission Factor Measurements with Optical Remote Sensing. *J. Air Waste Manage. Assoc.* 64: 227–234.

PART III: IMPROVEMENTS IN USING DIGITAL STILL CAMERAS AND CAMCORDERS TO MEASURE PLUME OPACITY

CHAPTER 5: PERFORMANCE AND UNCERTAINTY IN MEASURING ATMOSPHERIC PLUME OPACITY USING COMPACT AND SMARTPHONE DIGITAL STILL CAMERAS[4]

5.1 Abstract

Quantification of visible ambient plume opacity measurements using compact and smartphone digital still cameras (DSCs), and Digital Optical Method (DOM) are evaluated here. A new camera calibration method that employs exposure value compensation in place of exposure time or radiance of a surface is described and evaluated. This new method allows an automatic exposure controlled DSC to be calibrated using its own DSC settings. We also test the use of color in place of grayscale pixel values (PVs) to measure opacity. Finally, we determine the uncertainty of the opacity measurements. Two compact DSCs and two smartphone DSCs are tested to measure plume opacity values of smoke generated with an outdoor smoke generator, in comparison to the plume opacity values measured with an in-stack transmissometer. Results show that: 1) smartphone DSCs, like compact DSCs, can pass opacity measurement requirements set by USEPA; 2) the new simpler calibration method generates values within 5% in opacity on average compared to opacity values from the reference transmissometer; 3) non-uniform background color dominates the uncertainty of opacity measurements, and such uncertainty is wavelength dependent; and 4) the diffusive scattering parameter, used in DOM's transmission model, is lower for black plumes than white plumes, and is wavelength dependent. These results improve our understanding of using DSCs and the parameters that introduce

[4] Reprinted, with permission and minor revisions, from Yuen, W., Gu, Y., Mao, Y., Koloutsou-Vakakis, S., Rood, M.J., Son, H.-K., Mattison, K., Franek, B., and Du, K. (2017). Performance and Uncertainty in Measuring Atmospheric Plume Opacity Using Compact and Smartphone Digital Still Cameras. *Aerosol Air Qual. Res.* 17: 1281–1293.

uncertainty to DOM to improve measurements of plume opacity that can improve protection of human health.

5.2 Introduction

Technological advances have made possible the development of low-cost environmental sensors that are portable, and offer ability for rapid acquisition, transmission, storage, and analysis of data (Snyder et al., 2013). Questions have arisen regarding the accuracy of such methods compared to traditional standard methods (Nieuwenhuijsen et al., 2015; Reis et al., 2015). We present here results from using such method for monitoring plume opacity. Opacity is defined as the percent of visible light attenuated by a plume. Opacity relates to particulate matter (PM) concentration in plumes because PM is typically the most significant contributor of visible light attenuation. Measuring PM is important because it is an air pollutant that causes adverse health effects (Dockery and Pope, 1994; Pope and Dockery, 2006), reduces visibility (Malm, 1999; Watson, 2002), and affects climate (Anenberg et al., 2012). PM is regulated by the United States Environmental Protection Agency (USEPA) as a criteria air pollutant under the 1990 Clean Air Act Amendments (USEPA, 2016). The World Health Organization (WHO) also has established Air Quality Guidelines (WHO, 2006) for PM that provide an international reference for countries to set ambient air quality standards (Vahlsing and Smith, 2012). United States (US) legislation mandates opacity measurements at select industrial facilities to monitor emitted pollution (40 CFR Part 60, USEPA, 1993). Each US state may also have separate opacity standards specified in their State Implementation Plans (USEPA, 1993). USEPA promulgated Method 9 in 1974 for opacity evaluation, which specifies using human observers to measure plume opacity (USEPA, 1993). Drawbacks of Method 9 are subjective opacity readings by humans and difficulty to provide archival digital records of opacity readings and the

environment, such as meteorology or observational background during the measurement (Du et al., 2007). To resolve these issues, digital still cameras (DSCs) were evaluated and approved by American Society of Testing Materials (ASTM) as an appropriate technique to measure plume opacity values (ASTM Standard D7520, 2016). Besides the US, Canada regulates opacity from electricity generation sources (Environment and Climate Change Canada, 2010). Thailand also regulates opacity emitted from select sources, using measurement methods based on the USEPA Method 9 (Pollution Control Department, 2004). Other applications of DSCs in monitoring air quality include measurements of concentrations of black carbon (Du et al., 2011b; Ramanathan et al., 2011), fugitive PM emissions (Du et al., 2013), gaseous air pollutants such as ozone (Hasenfratz et al., 2012) and visibility monitoring (Poduri et al., 2010).

Digital Optical Method (DOM) was developed to measure ambient plume opacity values with DSCs (Du et al., 2007). DOM can be implemented using either the contrast or the transmission models. The contrast model requires the digital image to contain a plume that passes in front of and near two contrasting backgrounds. The transmission model requires the digital image to contain a plume that passes in front of and near one background that is in contrast to the plume. In the transmission model, the contrast between the plume and its background is parametrized by using a diffusive scattering parameter (K). DSCs are calibrated to relate amount of light exposure to pixel value (PV). Compact DSCs were classified into two types: manual exposure controlled, where exposure time and/or aperture size can be controlled, and automatic exposure controlled, where neither exposure time nor aperture size can be controlled. Previously, they were calibrated either by varying their exposure time for manual exposure controlled DSCs, or by varying the surface radiance of the same image for automatic

exposure controlled DSCs (Du, 2007). Average PVs are measured at several regions in an image and are used to determine the amount of exposure and then opacity.

Smartphones have become ubiquitous and provide additional desirable capabilities for monitoring plume opacity. Such capabilities could include software adaptation as a smartphone application, internet connectivity, and potential for crowdsourcing of plume opacity measurements. Thus, smartphone DSCs could be deployed for community monitoring of plume opacity values. Given the capabilities of smartphone technology, it is important to investigate how such technology can be used to obtain reliable opacity measurements.

This research improves our knowledge of using compact and smartphone DSCs in three areas. First, an alternative calibration method is evaluated. This does not require another calibrated DSC to calibrate automatic exposure controlled DSCs. Second, the effects of background color on measured opacity values are quantified. This is important because color contrasts between background(s) and plumes affect opacity measurement uncertainty. Third, the sources of uncertainty in the opacity measurements are identified, and their relative importance is quantified. Uncertainties of measured opacity values are determined using error propagation of DOM models. Such uncertainty evaluation describes the factors that affect uncertainty of opacity measurements, which are important for better decision in choosing appropriate environmental conditions for opacity measurements. Overall, these contributions increase the applicability and confidence in using DOM to measure plume opacity at non-ideal conditions, which encourages community monitoring of PM.

5.3 Methods

Two compact DSCs (Sony Cybershot DSC-P100 (Sony A) and Sony Cybershot DSC-S30 (Sony B)) and two smartphone DSCs (Samsung GT-S5360 (Samsung) and Nokia E61i

(Nokia)) were used during the field campaign. Both compact DSCs are manual-exposure controlled, and both smartphone DSCs are automatic-exposure controlled. Exchange Image File Format (EXIF) data from these DSCs are available in Table 5.1.

Table 5.1. Exchange Image File Format (EXIF) of the four digital still cameras. Cells marked with "(Unknown)" mean that the DSCs do not record that data. Such unrecorded data will not affect our measurement results because they are not included in our methods and analyses.

	Sony A	**Sony B**	**Samsung**	**Nokia**
Dimensions (pixel x pixel)	1280 x 960	1472 x 1104	1200 x 1600	1600 x1200
Horizontal resolution (dpi)	72	72	72	300
Vertical resolution (dpi)	72	72	72	300
Bit depth	24	24	24	24
Color representation	sRGB	sRGB	sRGB	sRGB
Typical f-stop	f/10	f/14	f/2.8	f/3.2
Exposure time (sec)	1/200 – 1/125	1/700 – 1/485	1/4000 – 1/2000	(Unknown)
ISO speed	ISO - 100	ISO - 100	ISO - 100	(Unknown)
Focal length (mm)	24	18	3	5
Flash mode	No flash	No flash	(Unknown)	No flash
White balance	Auto	(Unknown)	Auto	Auto
EXIF version	0220	0210	0220	0220

Camera Calibration

Camera calibration determined the relationship between exposure and PVs in a particular DSC, known as the response curve. Grayscale PV was calibrated by varying exposure time (ET method) for manual exposure controlled DSCs, and varying surface radiance (SR method) for automatic exposure controlled DSCs (Du, 2007). The ET method involves taking pictures of the same white surface, with the DSC's aperture size fixed and exposure time setting varied from 1/500 to 2 sec for 15 settings. Average PV is measured at the center of the each picture's white surface, with a sample size of 700 pixels by 500 pixels. A regression is then fit for ln(exposure time) against ln(PV), and the coefficients characterize the response curve of the DSC. Since exposure is proportional to exposure time, and DOM only requires relative exposure (ratio of exposure) between any two regions, exposure time is used as a proxy of relative exposure (Du,

2007). The SR method involves a calibrated manual exposure controlled DSC, an un-calibrated automatic exposure controlled DSC, and a checkerboard with twelve different shades of gray. The manual exposure controlled DSC is the reference for the SR method. The two DSCs are placed next to each other and each takes a digital image of the checkerboard. The average PV is obtained for each DSC within the center of each of twelve squares, typically 30 pixels by 30 pixels. PVs measured by the calibrated DSC are converted to the amount of relative exposure, based on exposure time. A quadratic regression is then fitted for ln(relative exposure) of the calibrated DSC against ln(PV) of the un-calibrated DSC, similar to the ET method.

The SR method requires an additional calibrated DSC to calibrate automatic exposure controlled DSCs. Therefore, we developed and tested the new exposure value compensation method (EC) to calibrate automatic exposure controlled DSCs as an alternative to the SR method. Automatic exposure controlled DSCs typically allow compensating exposure values (EVs), which describe the combined effects of exposure time and aperture size, using DSC settings. Each addition of one EV means doubling the exposure. This property allows obtaining the camera response curve by using the DSC settings and a white surface, without using a calibrated DSC. The EC method is similar to the ET method in that a DSC takes digital images of a white surface by varying the EV compensation, from -2 to +2 for 13 settings. An average PV for each digital image is determined as with the ET method. The quadratic fit procedure is also used, except $\ln(2^{EV})$ against ln(PV) is plotted because of the relationship of EV to exposure. The calibrations were performed with grayscale PVs and with Red-Green-Blue (RGB) PVs, resulting to four response curves for each DSC. These four curves were then used to quantify opacity values.

DSCs were calibrated with more than one method to compare the effect of calibration methods on measuring plume opacity. Sony A was calibrated by EC and ET methods, while Sony B was calibrated by the EC, ET, and SR methods. Both smartphone DSCs were only calibrated by the SR method because settings for changing exposure time and EV compensation are not available with these DSCs. Nevertheless, the recent smartphone DSCs (e.g., iPhone 8 and Samsung GT-I8190) have EV compensation setting (Apple Inc., 2018; Samsung, 2012), and more smartphone DSCs are expected to have such setting, so the EC method can be applied to more smartphone DSCs in the future. The ET response curve for Sony A was used to calibrate Sony B and the two smartphone DSCs through the SR method. We performed three replicates of calibrations for each calibration method and DSC combination. The replicates were used to characterize the effect of calibration uncertainty on opacity measurement uncertainty. The resulting fitted coefficients for each DSC, color, and calibration methods are provided in Table 5.2.

Table 5.2. Fitted coefficients (a, b, c) of calibration curves for each camera, color, and calibration method (ET, SR, and EC) and the regressions' corresponding R^2 values. The calibration curve has the following form for ET and SR: $\ln(\text{exposure})=a \ln^2(PV)+b \ln(PV)+c$, and has the following form for EC: $\ln(2^{EV})=a \ln^2(PV)+b \ln(PV)+c$. These fitted coefficients and R^2 values are the mean values from three replicated calibration curve measurements. Each replicate uses the following numbers of samples for calculating the regression – ET: 15, EC: 13, SR: 12.

Sony A

Color	Coefficients	ET	EC
Grayscale	a	0.37	0.71
	b	-1.60	-4.88
	c	-3.46	6.92
	R^2	0.98	1.00
Red	a	0.35	1.00
	b	-1.60	-7.76
	c	-3.45	13.57
	R^2	0.99	1.00
Green	a	0.29	0.69
	b	-0.98	-4.70
	c	-4.48	6.60
	R^2	0.99	1.00
Blue	a	0.14	0.21
	b	0.07	-0.55
	c	-4.96	-1.27
	R^2	0.99	0.99

Table 5.2 (cont.)

Sony B

Color	Coefficients	ET	SR	EC
Grayscale	a	1.08	0.77	0.61
	b	-7.39	-4.87	-3.69
	c	5.64	2.54	3.53
	R^2	0.98	1.00	1.00
Red	a	1.08	0.69	0.64
	b	-7.38	-4.38	-3.98
	c	5.61	1.69	4.03
	R^2	0.98	1.00	1.00
Green	a	1.21	0.62	0.60
	b	-8.55	-3.60	-3.57
	c	8.15	0.04	3.26
	R^2	0.98	1.00	1.00
Blue	a	0.58	0.47	0.50
	b	-3.00	-2.44	-2.71
	c	-3.10	-1.07	1.82
	R^2	0.98	1.00	1.00

Samsung

Color	Coefficients	SR
Grayscale	a	0.36
	b	-1.45
	c	-3.79
	R^2	0.99
Red	a	0.34
	b	-1.46
	c	-3.80
	R^2	0.99
Green	a	0.31
	b	-1.07
	c	-4.30
	R^2	0.98
Blue	a	0.20
	b	-0.38
	c	-3.92
	R^2	0.98

Table 5.2 (cont.)

Nokia

Color	Coefficients	SR
Grayscale	a	0.33
	b	-1.08
	c	-4.81
	R^2	0.99
Red	a	0.26
	b	-0.76
	c	-5.09
	R^2	0.99
Green	a	0.34
	b	-1.15
	c	-4.89
	R^2	0.99
Blue	a	0.17
	b	-0.23
	c	-4.13
	R^2	1.00

Field Campaign and Opacity Calculation

Calibrated DSCs were field tested in July 2013 in Springfield, IL, USA, during a daytime Illinois EPA visible emission evaluation course (Illinois EPA, 2015). A smoke generator produced black or white plumes from an elevated stack. A white-light transmissometer in the stack monitored plume opacity at 15 Hz and was the reference for comparison with DSC measured opacity values. During the visible emission evaluation course, DSCs observed plumes with the sun within 140° sector behind the DSCs, as per Method 9 and ASTM requirements (ASTM, 2013). All DSCs were 20 m from the smoke generator. Two different pairs of existing contrasting backgrounds were tested for black plumes and white plumes using the contrast model. The first background pair was a dark gray roof and the white (cloudy) sky. The second background pair was a red sign background and the white sky. In addition, we tested a single

white sky background using the transmission model for black plumes only. The statistics of grayscale and RGB PVs for the dark gray roof, the white sky, and the red backgrounds, measured by Sony B with EC calibration, are shown in Table 5.3 to justify the use of these color designations. Examples of digital images for such backgrounds are shown in Figure 5.1.

Table 5.3. Statistics of PV of the dark gray roof, the white sky, and the red backgrounds, measured by Sony B with EC calibration.

		Dark Gray Roof	**White Sky**	**Red Background**
Number of Data		29	29	20
Grayscale	Mean	114	210	42
	Standard Deviation	11	19	6
Red	Mean	118	201	100
	Standard Deviation	12	24	16
Green	Mean	113	212	14
	Standard Deviation	11	18	3
Blue	Mean	107	224	34
	Standard Deviation	9	16	4

Figure 5.1. Example digital images for each test conditions.

Black plume, dark gray roof and white sky background	White plume, dark gray roof and white sky background
	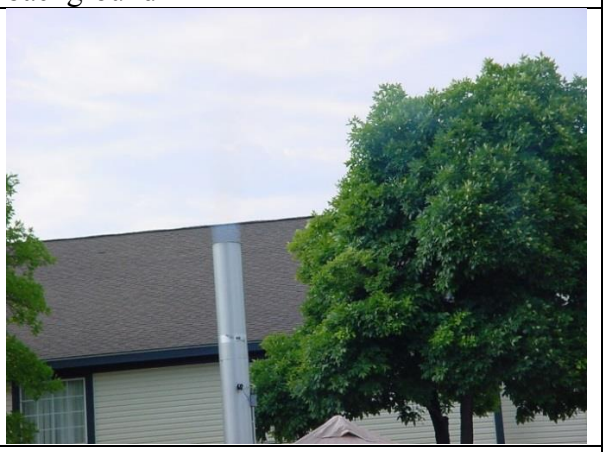
Black plume, red background and white sky background	White plume, red background and white sky background
	

The contrast model calculates plume opacity using two contrasting and co-located backgrounds. Four regions are selected in each digital image: two regions with a bright background with and without the plume in front of the backgrounds, and two regions with a dark background with and without the plume in front of the backgrounds. PVs within each of the four regions are determined and then averaged arithmetically. The average PVs in each region are then converted into amounts of relative exposure using the response curve for the respective calibrated DSC. The calculation to determine opacity values assumes that the light attenuation by the aerosol between the DSC and the plume is insignificant, which was verified previously (Du, 2007). Opacity is calculated using Eq. (5.1) (Du et al., 2007):

$$O_c = 1 - \frac{\frac{E_{wp}}{E_w} - \frac{E_{bp}}{E_w}}{1 - \frac{E_b}{E_w}} \tag{5.1}$$

where: O_c = plume opacity using contrast model; E_{wp} = amount of exposure caused by the bright background with plume; E_w = amount of exposure caused by the bright background without plume; E_{bp} = amount of exposure caused by the dark background with plume; and E_b = amount of exposure caused by the dark background without plume.

The transmission model calculates plume opacity using one background that is in contrast to the plume. Average PVs are measured at areas of background with the plume in front of and next to the background. The average PVs of each of the two regions are then converted to relative exposure using the camera response curve of a specific DSC. Opacity is calculated using Eq. (5.2) (Du et al., 2007):

$$O_t = \frac{1 - \frac{E_p}{E}}{1 - K} \tag{5.2}$$

where: O_t = plume opacity using transmission model; E_p = amount of exposure caused by the background with plume; E = amount of exposure caused by the background without plume; and K = diffusive scattering parameter. K is defined as:

$$K = \frac{\omega}{4\pi I_{np}(\theta = 0)} \left(\int_0^{2\pi} \int_{-1}^{1} I_{bg}(\theta) P(\theta) d\mu d\phi + P(\theta_S) S_0 e^{-\frac{\tau}{\mu_0}} \right) \tag{5.3}$$

where: ω = single scattering albedo of the plume; $I_{np}(\theta = 0) = I_{bg}(\theta = 0)$ = radiance of background light pointing at the referenced path; $I_{bg}(\theta)$ = radiance of background light at angle θ from the referenced path; $P(\theta)$ = scattering phase function of the plume at angle θ from the referenced path; μ = cos (zenith angle); ϕ = azimuth angle; $P(\theta_s)$ = scattering phase function at

angle between the sunlight and the referenced light path (θ_s); S_0 = solar constant = 1360 W/m^2; τ = optical depth of background atmosphere; and μ_0 = cos (solar zenith angle).

Inside the parentheses, the first term relates to the diffuse scattering of the background, and the second term relates to the direct solar radiation. Du (2007) also shows that when K = 1, the radiances of the plume and the background are equal, thus lacking contrast. Using Eq. (5.3), K was calculated to be 0.16 for a black plume in front of a blue sky, and 1.43 for a white plume in front of a blue sky (Du, 2007). Using the same method described by Du (2007), K was calculated to be 0.14 for a black plume in front of a white (overcast) sky background. K for a white plume against a white overcast was not calculated because of lack of contrast between the plume and the background colors, but such K should be 1 in theory. Since the K calculation method provided by Du (2007) requires assumptions of particle properties and models that simulate the radiance distribution of background light, we here used an empirical method to obtain K, which is described in the section "Analysis of Diffusive Scattering Parameter (K)" below. The empirical K values will be compared by the theoretical K values above.

Opacity Measurement Performance Metrics

The individual opacity errors (IOEs) and average opacity errors (AOEs) were calculated to evaluate the quantification of opacity values by the DSCs as defined by Method 9. IOE and AOE are defined as follows:

$$\mathrm{IOE} = \left| O_{c,i} - O_{t,i} \right| \tag{5.4}$$

where: $O_{c,i}$ = ith individual opacity measured by DSC and $O_{t,i}$ = ith individual opacity measured by transmissometer (reference signal).

$$\mathrm{AOE} = \frac{1}{N}\sum_{i=1}^{N}\left| O_{c,i} - O_{t,i} \right| \tag{5.5}$$

where: N = the total number of individual measurements in a set for a plume type.

Human observers are certified to measure plume opacity if the maximum IOE does not exceed 15% in opacity and AOE does not exceed 7.5% in opacity for black and white plumes during a test sequence (Method 9, USEPA, 1993). Using these criteria, DOM has been successfully tested with grayscale PV measurements (Du et al., 2007). In this research, these criteria will be tested on grayscale and RGB PVs.

Uncertainty Analysis

Uncertainty of opacity values can be due to two reasons: uncertainty in camera calibration and uncertainty due to the non-uniformity of the background colors, as quantified by PVs. The former relates to DSC hardware uncertainty, while the latter relates to conditions external from the DSCs. To determine the uncertainty due to camera calibration, we calculated amounts of relative exposure due to plume opacity value three times, using DOM models and the three replicate camera calibrations that were mentioned previously. The greatest opacity absolute difference resulting from the three response curves was treated as uncertainty and reported.

In both DOM models, backgrounds are assumed to be uniformly colored, which means the standard deviation of PVs within a select region is zero. However, such condition is challenging to achieve in the ambient environment. To determine the uncertainty due to non-uniformity of the background colors, the standard deviation of PVs was determined for each background first. To do so, a color image that includes a plume in front of and next to two contrasting backgrounds was selected. Four regions in the picture describing the backgrounds, defined by the contrast model, were randomly selected ten times, using random dimensions of rectangles (typically with sizes between 10 pixel x 10 pixel and 30 pixel x 30 pixel, within a 50 pixel x 50 pixel area). These four regions have average PVs between 75 and 200. The standard deviations of the PVs for these replicates for each background region were calculated. The

results showed that the standard deviations ranged from 0.3 to 2.1 PV and coefficients of variations (COVs, (standard deviation/mean)×100%) from 0.4% to 1.8%. For the pictures from our field experiment, the maximum PV standard deviation occurs at the dark gray roof region with plume present, where the edges of tiles on the roof introduce non-uniform color. Next, measured mean PVs of the select regions in other digital images were increased or decreased by a PV deviation of 2 because this was the maximum standard deviation determined in the background PV standard deviation tests that is explained above, rounded to an integer because PVs can only be set as integer values. Uncertainties of exposures (δEs) in each of the select regions in a digital image were then calculated by determining the difference in E between the measured PVs, with and without PV deviation, using the camera response curve. Opacity uncertainties were then calculated by using error propagation (Bevington and Robinson, 2002) on Eqs. (5.1) and (5.2) and δEs, assuming that the measured quantities are independent of each other. The opacity uncertainty for the DOM contrast model (δO_c) results in:

$$\delta O_c = \left| \frac{1}{E_w - E_b} \right| \sqrt{\left(\delta E_{wp}{}^2 + \delta E_{bp}{}^2 \right) + \left(1 - O_c \right)^2 \left(\delta E_w{}^2 + \delta E_b{}^2 \right)} \tag{5.6}$$

while the opacity uncertainty for the transmission model (δO_t) results in:

$$\delta O_t = \left| \frac{1}{1 - K} \right| \sqrt{\left(\frac{E_p}{E} \right)^2 \left[\left(\frac{\delta E_p}{E_p} \right)^2 + \left(\frac{\delta E}{E} \right)^2 \right] + \left(O_t \delta K \right)^2} \tag{5.7}$$

where δO_c and δO_t describe the uncertainties of O_c and O_t in Eqs. (5.1) and (5.2), respectively. The uncertainty of the K (δK) was determined empirically by the standard deviation of K (see the section "Analysis of Diffusive Scattering Parameter (K)" below). Eq. (5.6) indicates that when the two contrasting backgrounds lack contrast, E_w - E_b approaches zero and opacity uncertainty approaches infinity. Similarly, Eq. (5.7) indicates that when K approaches to 1,

which happens when the plume and the background lack contrast, opacity uncertainty also approaches infinity. Increasing contrast between two backgrounds, or between a background and a plume, is therefore needed so that uncertainty of opacity value decreases. Both positive and negative deviations by 2 PV were tested, but since positive deviations differ from negative deviations by < 0.3% opacity for all grayscale and RGB measurements, only results with positive deviations are shown in the section "Results and Discussion".

Analysis of Diffusive Scattering Parameter (K)

To empirically obtain K for select background and plume color combinations, we first calculated the plume opacity using two contrasting backgrounds and the contrast model (Eq. (5.1)). Then, for each DSC, we used the transmission model (Eq. (5.2)), opacity values from the contrast model, and the one background that was in contrast to the plume to back-calculate K. Means and standard deviations of K were calculated and are reported, by each background-plume color combination, and by grayscale and RGB PV values. Before calculating the statistics of K, outliers were identified by using 1.5 times inter-quartile range of all the K data in each category, and were removed (Montgomery and Runger, 2011). These outliers are possibly caused by unknown random errors introduced by, for instance, fast changing micrometeorological conditions that can alter the plume direction and turbulent dispersion.

5.4 Results and Discussion

Number of pictures taken by each DSC, for each background type and plume color, are shown in Table 5.4. Although we aimed to obtain at least 25 digital images for each DSC in each measurement condition due to Method 9 requirements, some DSCs using red background and white sky have less than 25 digital images because of the short window of measurement period for this condition.

Table 5.4. Summary of digital images used for this study.

Background type	Plume color	Camera Identification	Number of digital images
Dark gray roof and white sky	Black	Sony A	58
		Sony B	59
		Samsung	51
		Nokia	54
	White	Sony A	30
		Sony B	29
		Samsung	27
		Nokia	26
Red background and white sky	Black	Sony A	20
		Sony B	20
		Samsung	21
		Nokia	20
	White	Sony A	30
		Sony B	22
		Samsung	28
		Nokia	28

Opacity Measurement Performance

The comparisons between opacity measurements of DSCs and the transmissometer in grayscale, using the dark gray roof and white sky as the contrasting background pair, are shown in Figures 5.2(A) and (B). Box plots that summarize the IOE data in grayscale for each compact or smartphone DSC and each plume color using the same background pair are shown in Figures 5.2(C) and (D). When using this background pair, both compact DSCs and both smartphone DSCs passed Method 9 criteria for black and white plumes.

Figure 5.2. Comparisons between opacity values measured by the DSCs and transmissometer using the contrast model, in grayscale, for (A) black plumes and (B) white plumes, using dark gray roof and white sky as the contrasting background pair. The 1:1 line shows perfect agreement in measurements. The ±15% lines show the maximum IOE allowable for a DSC to pass the certification in measuring plume opacity. Box plots that summarize IOE and AOE results for each DSC are also shown for (C) black plumes and (D) white plumes.

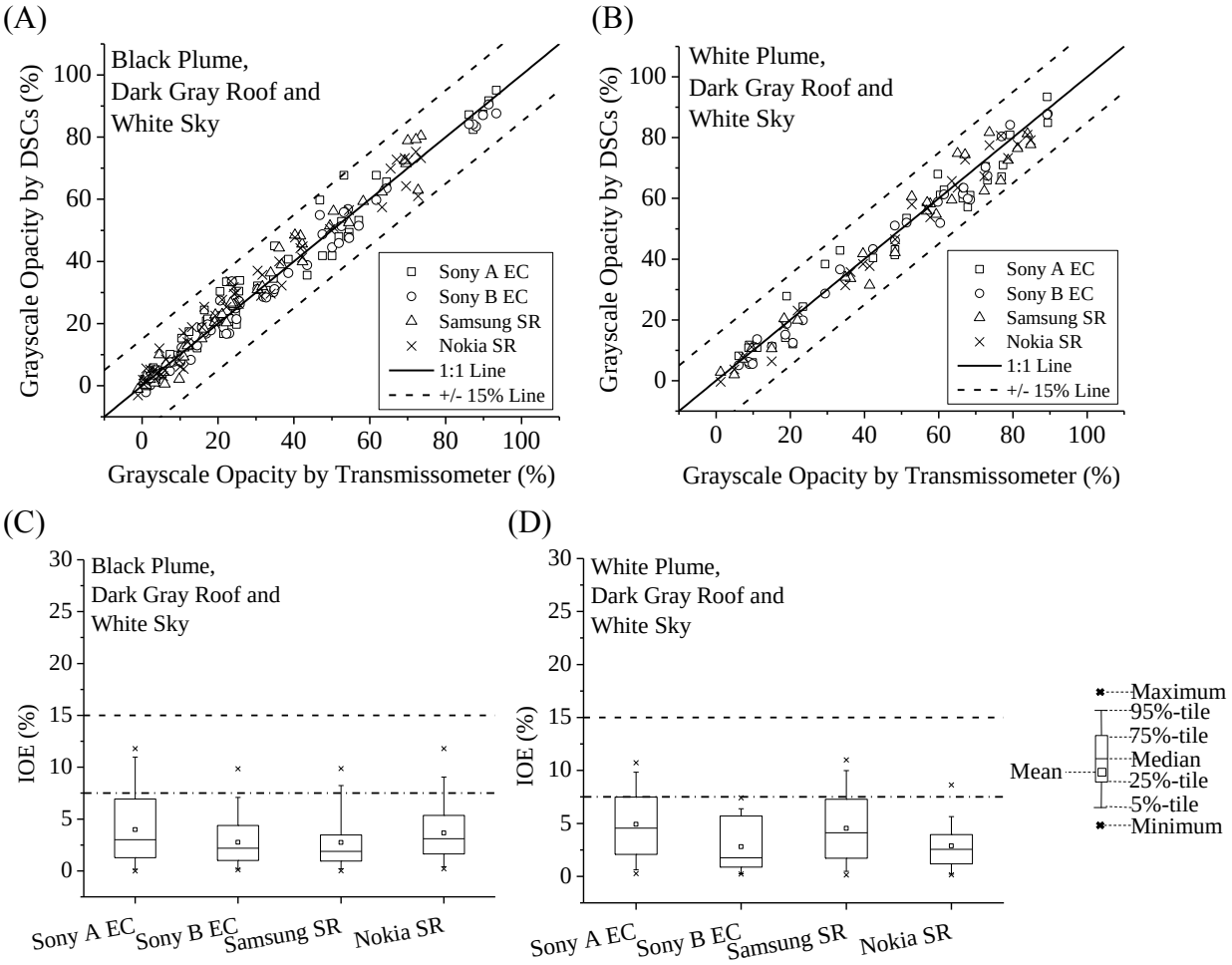

The comparisons between opacity values measured by the DSCs and transmissometer in grayscale, using the white sky as the only background and transmission model for black plume only, are shown in Figure 5.3(A). We did not use the transmission model for white plumes with the white sky background due to the lack of sufficient contrast between the white plumes and white sky background. The box plot that summarizes the IOEs for black plumes in grayscale, for opacity values measured by each compact or smartphone DSC using transmission model

compared to transmissometer values, is shown in Figure 5.3(B). The results show that all four DSCs passed the Method 9 AOE and IOE requirements.

Figure 5.3. (A) Comparisons between opacity measurements of DSCs and transmissometer using the transmission model, in grayscale, for black plumes and white sky background (K = 0.14). The 1:1 line shows perfect agreement in measurements. The ±15% lines show the maximum IOE allowable for a DSC to pass the certification in measuring plume opacity. (B) Box plot that summarizes corresponding IOE and AOE results for each DSC, for black plumes and white sky background.

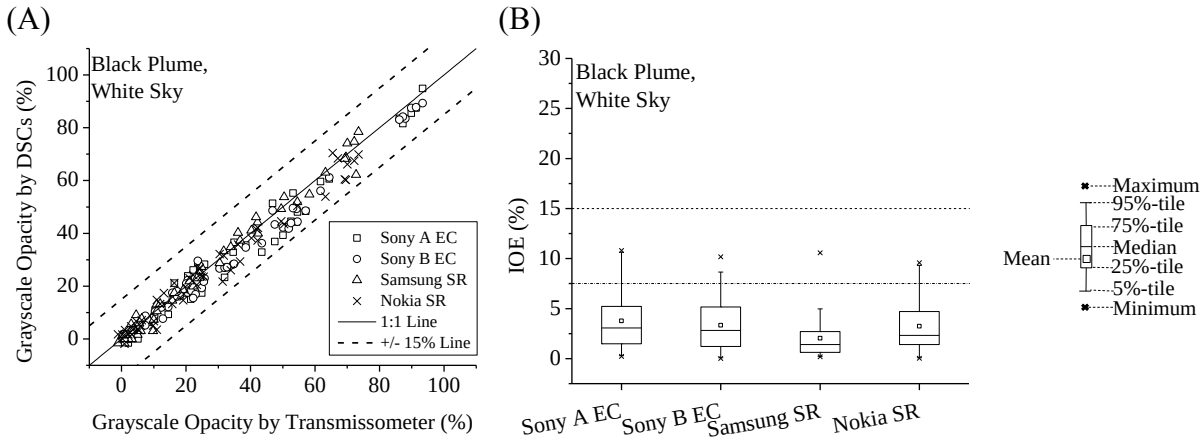

The comparisons between opacity measurements of DSCs and transmissometer in grayscale, using red background and white sky as the contrasting background pair, are shown in Figure 5.4(A) for black plume and (B) for white plume. Box plots that summarize the IOE data for each compact or smartphone DSC, using the same background pair, are shown in Figure 5.4(C) for black plume and (D) for white plume. In contrast with the dark gray roof and sky background pair for black and white plumes (Figure 5.2), AOEs for all DSCs are > 7.5% for white plumes using red background and white sky background pair. AOEs for the two smartphone DSCs are also > 7.5% for black plumes using red background and white sky background pair. From the data in Figures 5.2 through 5.4, using the dark gray roof and white sky background pair produces more accurate opacity results than using the red background and

white sky background pair. We expect that the results are due to background color, which will be further explained in the next section "Wavelength Dependence".

Figure 5.4. Comparisons between opacity measurements of DSCs and transmissometer using contrast model, in grayscale, for (A) black plumes and (B) white plumes, using red background and white sky as contrasting background pair. The 1:1 line shows perfect agreement in measurements. The ±15% lines show the maximum IOE allowable for a DSC to pass the certification in measuring plume opacity. Box plots that summarize IOE and AOE results for each DSC are also shown for (C) black plumes and (D) white plumes.

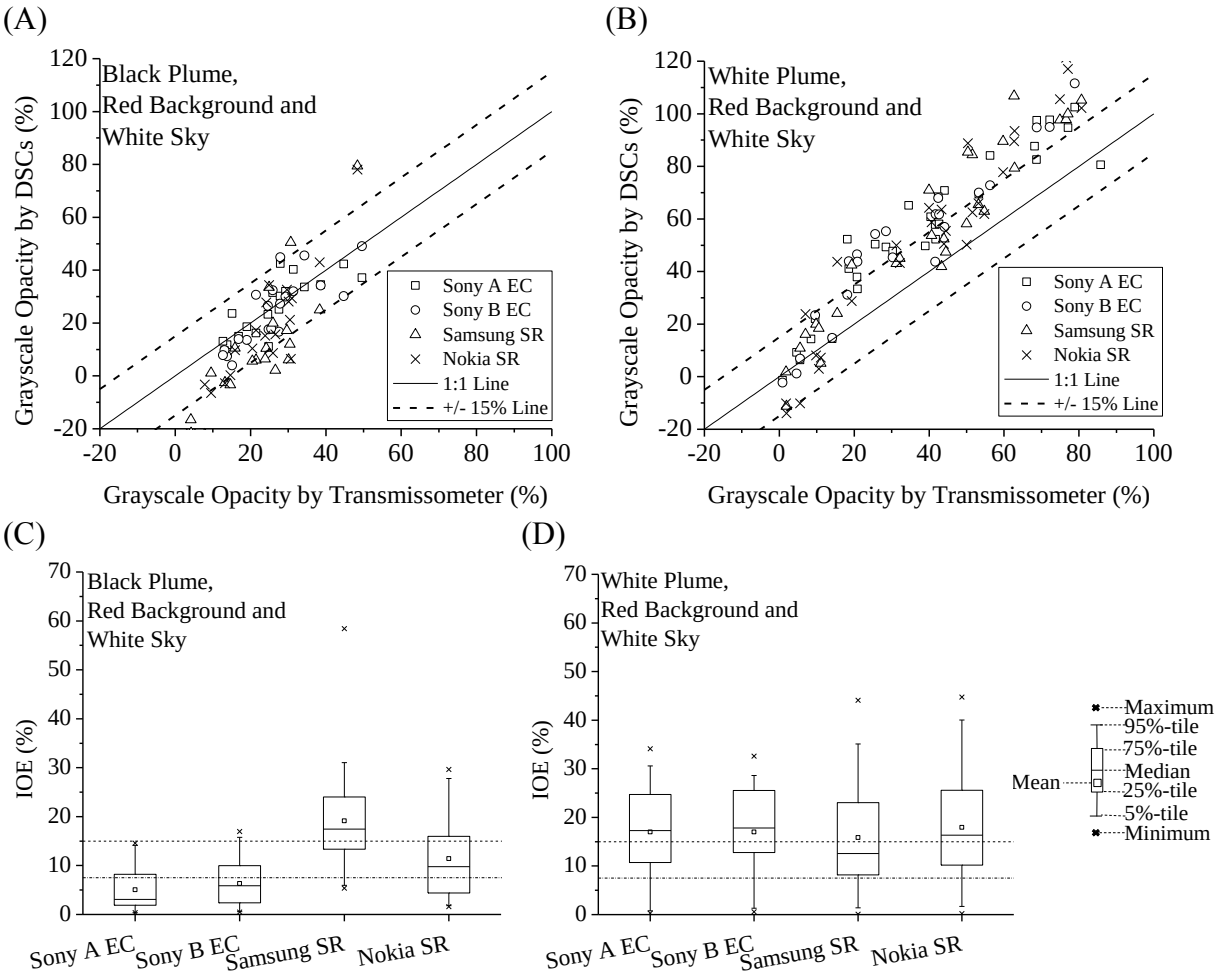

The comparison of box plots describing IOEs and AOEs among three calibration methods (EC, ET, and SR) for the Sony B DSC, when measuring plume opacity values with the contrast model for black and white plumes, using the dark gray roof and white sky background pair, are shown in Figure 5.5. The new EC and the previous ET and SR methods result in AOEs (Eq.

(5.5)) of 2.8%, 4.1%, and 2.6% in opacity, respectively, for black plumes, and 2.8%, 5.6%, and 3.4% in opacity, respectively, for white plumes, using grayscale PV measurements (Figure 5.5). This shows that the new EC method yields opacity values similar to the previous SR calibration method, making the EC method possible as an alternative method to calibrate automatic exposure controlled DSCs. The effect of calibration method on opacity uncertainty is examined in the "Uncertainty Analysis" section.

Figure 5.5. Boxplots that summarize IOE and AOE values among the three calibration methods (EC, ET, and SR) using grayscale for Sony B DSC, and contrast model with dark gray roof and white sky background pair, for (A) black plumes and (B) white plumes.

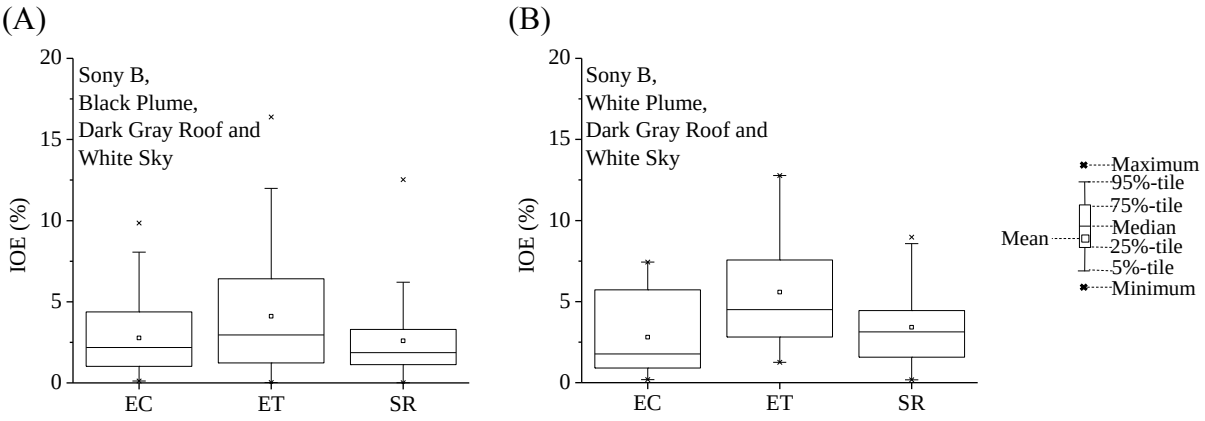

Wavelength Dependence

The difference in performance of DOM due to background color has been demonstrated in Figures 5.2 through 5.4. Since backgrounds can have a wide range of colors, this motivated us to look at the wavelength effect on the opacity measurements. The results may help making decisions regarding the choice of backgrounds to determine opacity values with DOM. For brevity, only comparison of plume opacity values measured by Sony B DSC's RGB PVs to that measured by the transmissometer, using two different background pairs, is shown in Figure 5.6. A 1:1 line is shown to denote perfect agreement line. In Figure 5.6(A) for white sky and dark gray roof background pair, opacity measured by red PV has an AOE of 6.5%. However, when

looking at Figure 5.6(B) that uses the red background and white sky background pair, measurements in red PV has a higher AOE (19.1% AOE), while AOEs for green PV and blue PV are 6.8% and 4.7%, respectively. This is because the red PV contrast between red and white sky backgrounds is less than the red PV contrast between white sky and dark gray roof backgrounds. A red background reflects more red light but absorbs more green and blue light, while white sky reflects all visible light. This statement is evidenced by the RGB PVs of the two backgrounds as shown in Table 5.3 ([R, G, B] = [100, 14, 34] for PVs of red background, and [R, G, B] = [201, 212, 224] for PVs of white background). The differences of PVs between the two backgrounds can be used as a proxy for contrast, which is 101 for red, 198 for green, and 190 for blue. This means lower contrast between red and white sky backgrounds for red light than for blue or green light, and successively results in higher opacity uncertainty for red PV. Similar results are expected for green light and green background or blue light and blue background, but there were not available background in these colors to test for this field experiment.

Figure 5.6. Relationship of opacity measurements of Sony B DSC using RGB PVs to grayscale transmissometer measurements for black plumes using contrast model. Background pairs are (A) dark gray roof and white sky, and (B) red background and white sky.

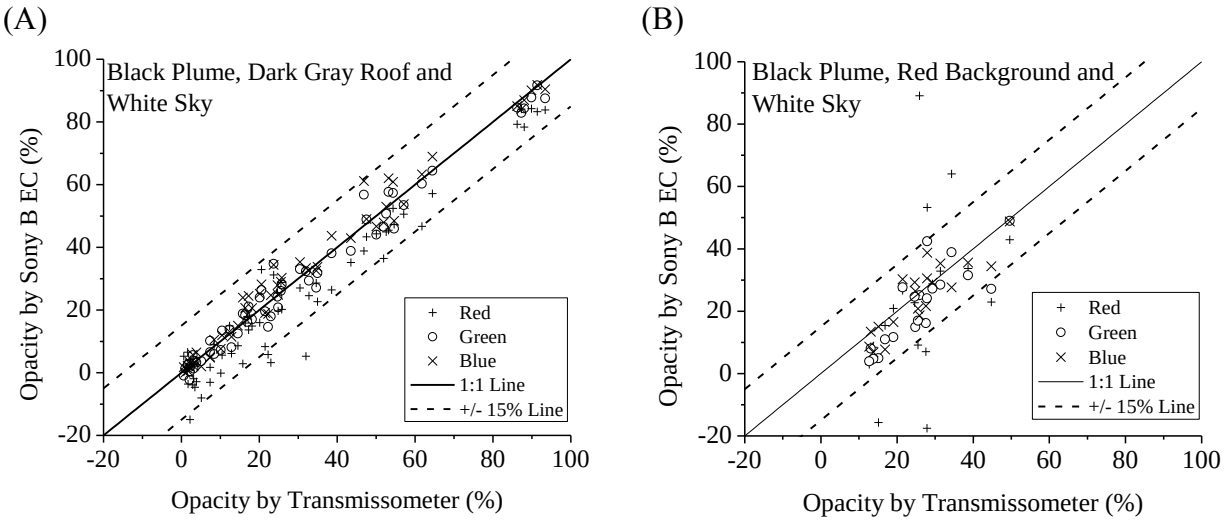

We also observe in Figure 5.6(A) that even when using a white sky and dark gray roof background pair, where PVs for red, green, and blue are the same, opacity measured by red PV tends to be lower than grayscale transmissometer measurements (by an average of 6.5% in opacity), while opacity measured by blue PV tends to be higher than grayscale transmissometer measurements (by an average of 1.2% in opacity). Opacity measured by green PV is only slightly lower than grayscale transmissometer measurements (by an average of 0.7% in opacity). Such similar trend is observed when the opacity values measured by RGB PVs are plotted against these values measured by grayscale PV (Figure 5.7). This happens because opacity depends on wavelength of light, as described by the Ångström equation (Ångström, 1964). The red PV results in the highest systematic error because Ångström equation is non-linear, and red has the longest wavelength. Such wavelength dependence of opacity was also observed by Conner and Hodkinson (1972). The results in Figure 5.6(A) suggest that using DSCs' green or blue PV can be a substitute to grayscale PV in measuring plume opacity for black-and-white background pair, since opacity measured by green or blue PVs differ from opacity measured by grayscale PV by < 2%. Such results are also supported by the maximum IOEs and AOEs as compared to grayscale transmissometer measurements (maximum IOEs for red, green, and blue are 26.7%, 11.1%, and 14.3%, respectively. AOEs for red, green, and blue are 7.8%, 3.0%, and 3.0%, respectively). Such use of alternative light wavelengths is useful if backgrounds have higher contrast when using green or blue compared to grayscale. As mentioned before, higher contrast reduces the uncertainty of opacity measurements. For example, for Figure 5.6(B), the average grayscale PV of the red background and the white sky background, measured by Sony B, are 42 and 157, respectively. However, the average green PV of the red background and the white sky background are 14 and 159, respectively. Thus, using green PV provides more contrast

than using grayscale PV because the PV difference is 145 for the green wavelength, which is larger than 115 for the grayscale. Conversely, using red PV of the DSC to measure plume opacity is not recommended due to the highest systematic error in opacity measurements.

Figure 5.7. Relationship of opacity measurements of Sony B with EC calibration using RGB PVs to grayscale PVs for black plumes using contrast model. The figure substantiates the wavelength dependence of opacity measurements observed in Figure 5.6(A). Background pair is dark gray roof and white sky.

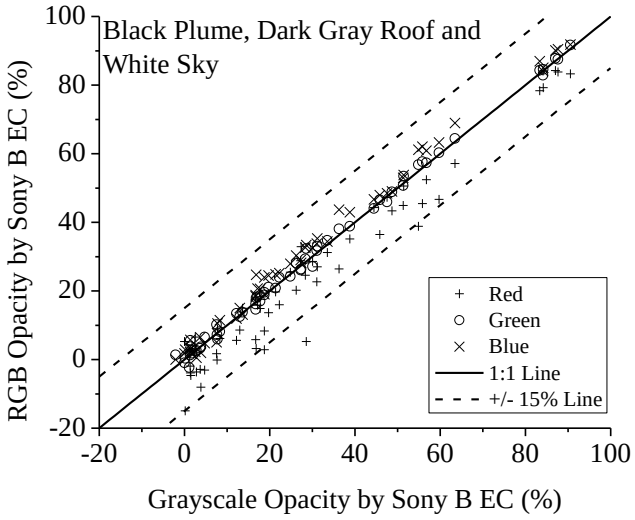

Uncertainty Analysis

The maximum absolute opacity differences of Sony B, Samsung, and Nokia, calculated from the triplicate response curves are shown in Table 5.5. The maximum considers the difference for all grayscale and RGB PVs. Results from Sony A are absent because replicates are not available. Results show that uncertainty due to camera calibration introduces < 2% opacity uncertainty.

Table 5.5. Maximum absolute opacity differences among triplicate calibration curves that represent the uncertainty of opacity values due to calibration of the DSCs. The maximum considers the difference for all grayscale and RGB PVs.

Plume color	Background	Sony B EC (%)	Samsung SR (%)	Nokia SR (%)
Black	Dark gray roof and white sky	0.1	0.3	1.2
White	Dark gray roof and white sky	0.2	0.5	0.2
Black	White sky only	1.0	0.4	2.3
Black	Red background and white sky	0.1	0.4	1.2
White	Red background and white sky	0.1	0.3	2.0

*Sony A results are absent because replicates are not available

The calculated uncertainty of DSC grayscale opacity measurement due to non-uniform background colors is shown in Figure 5.8. The results are grouped between the two plume colors, and between two contrasting background pairs. The results show that uncertainty due to non-uniform background colors is 2 – 15% in opacity, which is higher than the uncertainty due to camera calibration (< 2%).

Figure 5.8. Statistics of calculated opacity uncertainty in grayscale due to non-uniform background colors for (A) black plumes and (B) white plumes, using dark gray roof and white sky background pair and contrast model; (C) black plumes, using white sky background and transmission model; (D) black plumes and (E) white plumes, using red background and white sky background pair and contrast model.

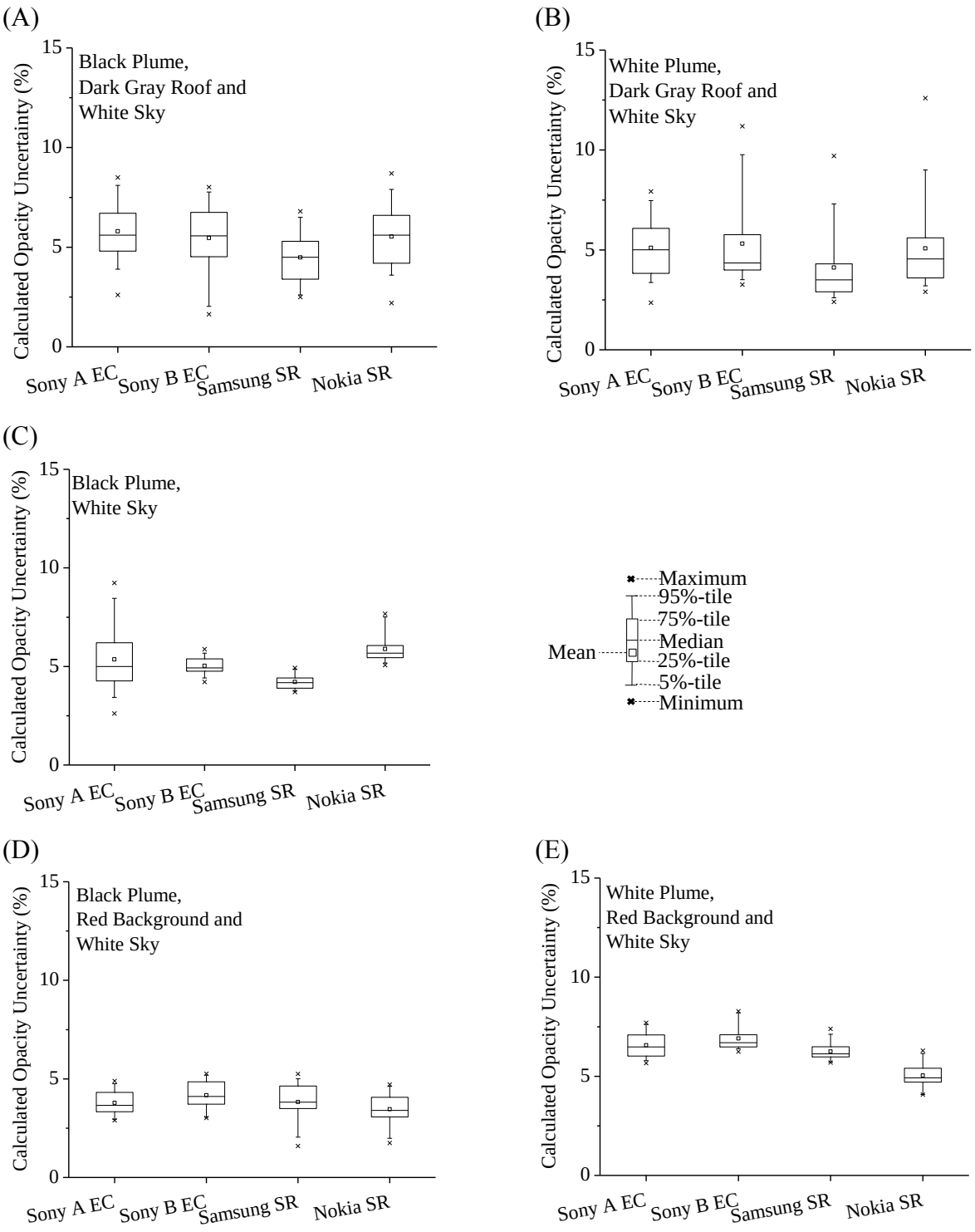

The calculated DSC RGB opacity measurement uncertainties due to non-uniform background colors are shown in Figure 5.9. The calculated uncertainties show that red PVs introduce the highest uncertainty (a maximum of 43% in opacity in red PV, compared to 10% in green PV and 5% in blue PV), which is consistent with results shown in Figure 5.6(A).

Figure 5.9. Statistics of calculated opacity uncertainty in RGB due to non-uniform background colors for (A) black plumes and (B) white plumes, using dark gray roof and white sky background pair and contrast model; (C) black plumes and (D) white plumes, using red background and white sky background pair and contrast model.

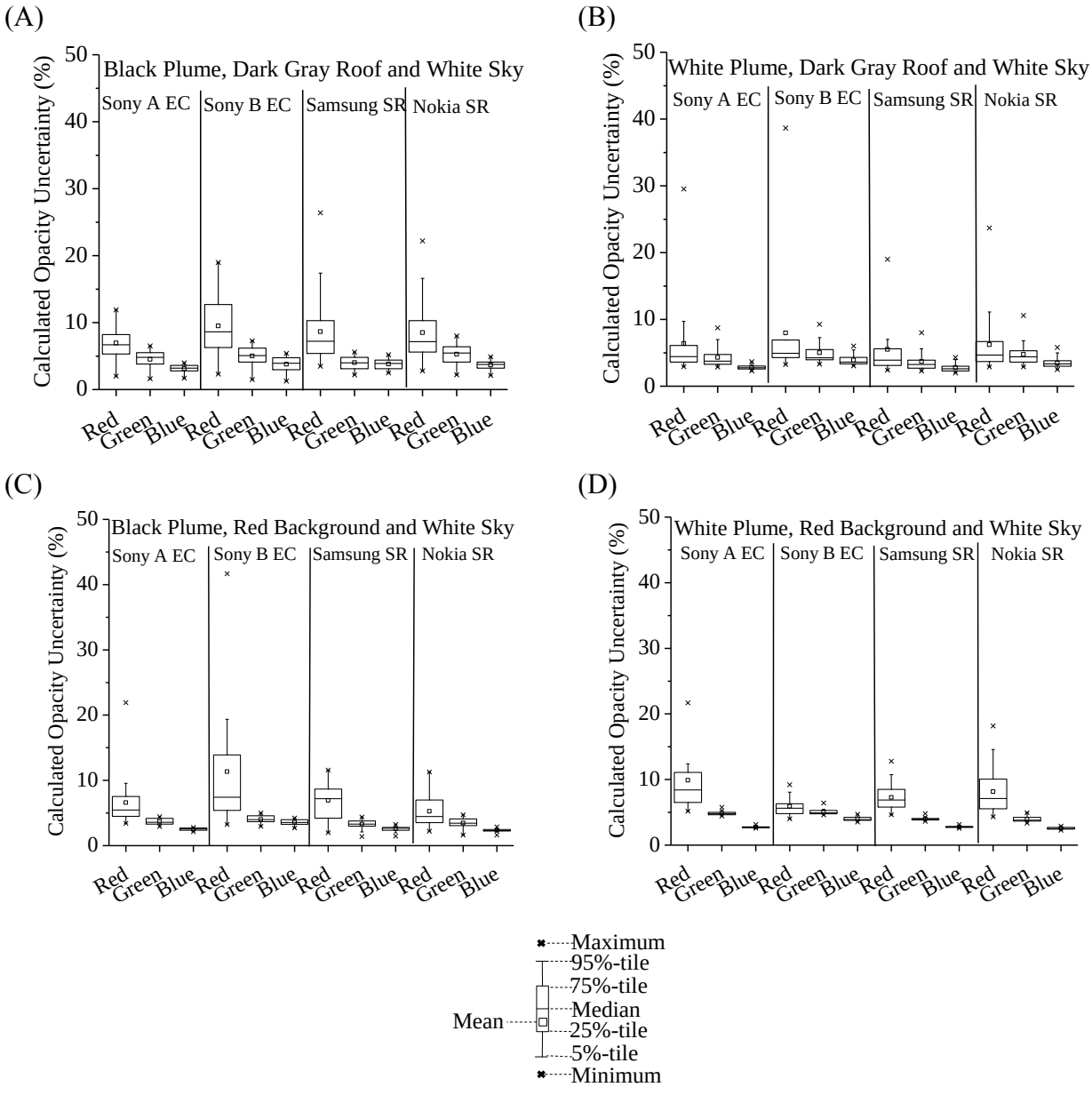

Analysis of Diffusive Scattering Parameter (K)

Statistics of empirical K values of select plume colors (i.e., black or white plumes) against select backgrounds (i.e., white sky, dark gray roof, or red background) are displayed in Figure 5.10 for each DSC and its color PV channels. The corresponding empirical K values are shown in Table 5.6. Overall, K values are smaller for black plumes than for white plumes in all DSC color PV channels. This observation is consistent with literature values for blue sky background (0.16 for black plume and 1.43 for white plume, Du, 2007). The reason is that black plumes have lower single scattering albedo (scattering to total extinction ratio). Thus, according to Eq. (5.3), K is smaller for black plume. The empirical K value for black plume against white sky background in grayscale is between 0.17 and 0.27 (Table 5.6), compared to 0.14 that is calculated from Eq. (5.3), 39% smaller when compared to the mean of empirical K values. As mentioned before, when the background and the plume lack contrast, K is theoretically equal to 1. The empirical K value in grayscale is between 0.80 and 0.87 for white plume against white sky, and between 0.64 and 0.89 for black plume against dark gray roof (Table 5.6). The theoretical value is 19% larger when compared to the mean of empirical K values for white plume against white sky, and 31% larger when compared to black plume against dark gray roof. The results show the closeness between theoretical and empirical K values when background and plume lack contrast.

Figure 5.10. Statistics of measured diffusive scattering parameters (K) for (A) black plumes and (B) white plumes, for white sky background; (C) and (D): similar to (A) and (B), but for dark gray roof background; (E) and (F): similar to (A) and (B), but for red background. Bars show means and error bars show standard deviations.

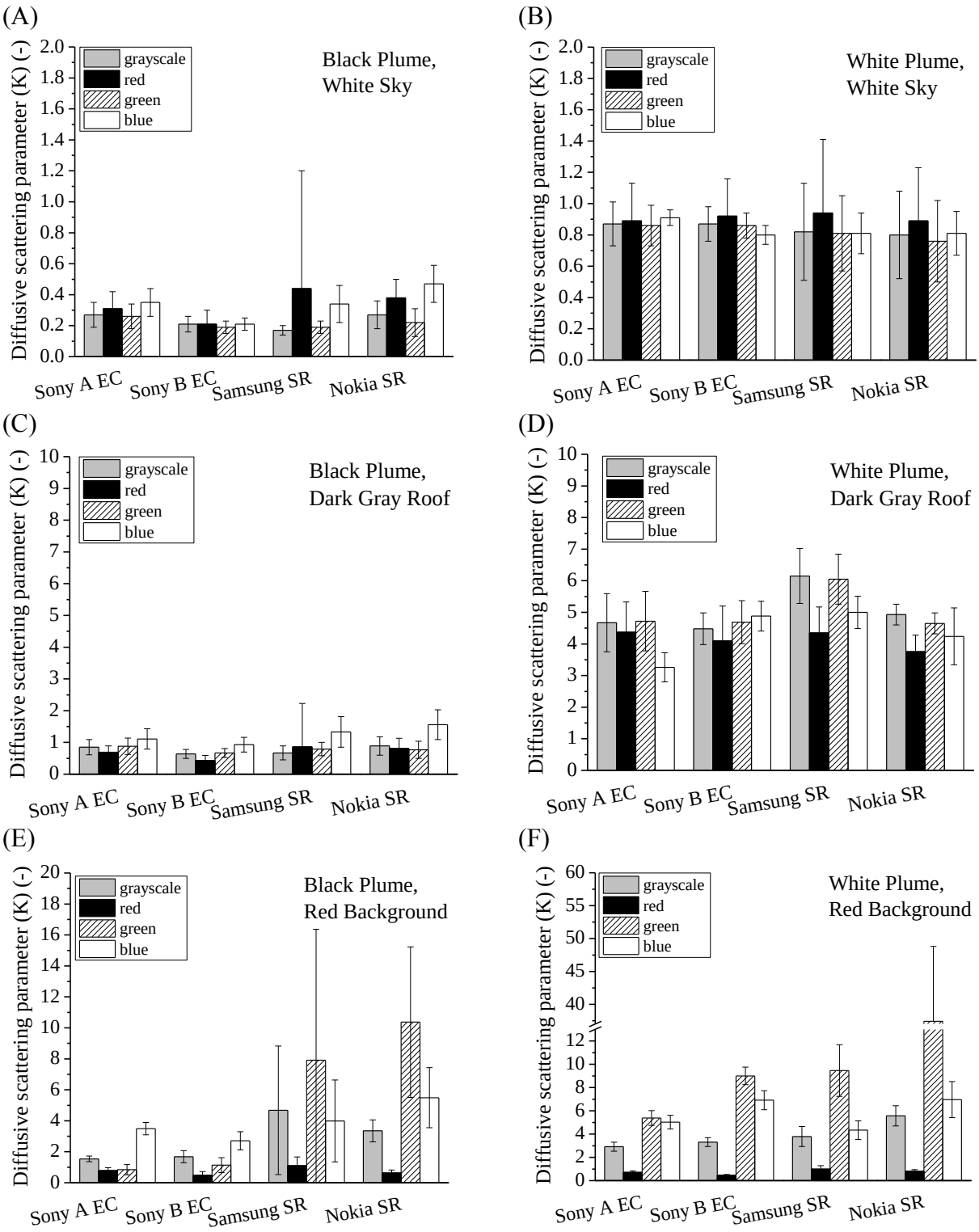

Table 5.6. Summary of K statistics for each camera and two colors of plumes for grayscale and RGB measurements. COV = coefficient of variation.

Black plume against white sky background

		Sony A	**Sony B**	**Samsung**	**Nokia**
Number of Data		48	30	20	35
Grayscale	Mean	0.27	0.21	0.17	0.27
	Standard Deviation	0.08	0.05	0.03	0.09
	COV (%)	30	24	18	33
Red	Mean	0.31	0.21	0.44	0.38
	Standard Deviation	0.11	0.09	0.76	0.12
	COV (%)	35	43	173	32
Green	Mean	0.26	0.19	0.19	0.22
	Standard Deviation	0.08	0.04	0.04	0.09
	COV (%)	31	21	21	41
Blue	Mean	0.35	0.21	0.34	0.47
	Standard Deviation	0.09	0.04	0.12	0.12
	COV (%)	26	19	35	26

Black plume against dark gray roof background

		Sony A	**Sony B**	**Samsung**	**Nokia**
Number of Data		48	30	20	35
Grayscale	Mean	0.85	0.64	0.67	0.89
	Standard Deviation	0.24	0.14	0.22	0.29
	COV (%)	28	22	33	33
Red	Mean	0.69	0.43	0.86	0.81
	Standard Deviation	0.20	0.16	1.37	0.32
	COV (%)	29	37	159	40
Green	Mean	0.88	0.67	0.79	0.77
	Standard Deviation	0.26	0.14	0.21	0.27
	COV (%)	30	21	27	35
Blue	Mean	1.11	0.93	1.33	1.56
	Standard Deviation	0.32	0.23	0.48	0.47
	COV (%)	29	25	36	30

Table 5.6 (cont.)

White plume against white sky background

		Sony A	Sony B	Samsung	Nokia
Number of Data		23	18	21	17
Grayscale	Mean	0.87	0.87	0.82	0.80
	Standard Deviation	0.14	0.11	0.31	0.28
	COV (%)	16	13	38	35
Red	Mean	0.89	0.92	0.94	0.89
	Standard Deviation	0.24	0.24	0.47	0.34
	COV (%)	27	26	50	38
Green	Mean	0.86	0.86	0.81	0.76
	Standard Deviation	0.13	0.08	0.24	0.26
	COV (%)	15	9	30	34
Blue	Mean	0.91	0.80	0.81	0.81
	Standard Deviation	0.05	0.06	0.13	0.14
	COV (%)	5	8	16	17

White plume against dark gray roof background

		Sony A	Sony B	Samsung	Nokia
Number of Data		23	18	21	17
Grayscale	Mean	4.67	4.48	6.15	4.93
	Standard Deviation	0.92	0.50	0.87	0.33
	COV (%)	20	11	14	7
Red	Mean	4.37	4.10	4.35	3.76
	Standard Deviation	0.96	1.10	0.82	0.52
	COV (%)	22	27	19	14
Green	Mean	4.72	4.69	6.05	4.65
	Standard Deviation	0.94	0.68	0.79	0.33
	COV (%)	20	14	13	7
Blue	Mean	3.26	4.88	5.00	4.24
	Standard Deviation	0.46	0.47	0.51	0.90
	COV (%)	14	10	10	21

Table 5.6 (cont.)

Black plume against red background

		Sony A	Sony B	Samsung	Nokia
Number of Data		15	12	12	12
Grayscale	Mean	1.54	1.68	4.68	3.35
	Standard Deviation	0.18	0.39	4.15	0.71
	COV (%)	12	23	89	21
Red	Mean	0.79	0.48	1.10	0.63
	Standard Deviation	0.18	0.24	0.56	0.19
	COV (%)	23	50	51	30
Green	Mean	0.84	1.14	7.91	10.37
	Standard Deviation	0.33	0.48	8.46	4.86
	COV (%)	39	42	107	47
Blue	Mean	3.49	2.71	3.99	5.49
	Standard Deviation	0.40	0.59	2.64	1.94
	COV (%)	11	22	66	35

White plume against red background

		Sony A	Sony B	Samsung	Nokia
Number of Data		24	15	24	18
Grayscale	Mean	2.91	3.31	3.79	5.57
	Standard Deviation	0.39	0.38	0.86	0.87
	COV (%)	13	11	23	16
Red	Mean	0.72	0.46	1.00	0.80
	Standard Deviation	0.11	0.06	0.28	0.15
	COV (%)	15	13	28	19
Green	Mean	5.38	9.00	9.46	37.43
	Standard Deviation	0.63	0.75	2.22	11.37
	COV (%)	12	8	23	30
Blue	Mean	5.03	6.91	4.34	6.96
	Standard Deviation	0.59	0.81	0.80	1.55
	COV (%)	12	12	18	22

When considering wavelength dependence of K for red background, the empirically derived K values for green and blue wavelengths are 4 to 47 times larger than K values at red PV for white plumes, and 1 to 16 times higher for black plumes. A possible explanation for the smallest K for red PV with red background is that a lower background light radiance results in a higher K value based on Eq. (5.3). Since radiance of red light is higher than the other two colors for red background, K is the smallest for red PV. The results demonstrate that when the background color is not on grayscale, K value depends on wavelength of background color.

COVs of K values were also calculated for each background, plume color, and wavelength of measurement, in order to evaluate the uncertainty of K determined by this empirical approach. After removing COV outliers by using the 1.5 times inter-quartile range method (Montgomery and Runger, 2011), the range of COVs of K values for all grayscale, red, green, and blue measurements are 7% – 38%, 13% – 51%, 7% – 47%, and 5% – 36%, respectively. This shows that K values determined by red wavelength have the highest uncertainty.

5.5 Conclusions

Compact digital still cameras (DSCs) offer the advantage of objectivity and provide archival records compared to Method 9 human observers to quantify plume opacity values. Using smartphone DSCs offers advantages over compact DSCs including plume opacity quantification with location identification, software adaptation as a smartphone application, and wireless connectivity. This research demonstrates that the performance of smartphone DSCs on measuring plume opacity is as good as compact DSCs, by passing the Method 9 requirements. We recommend the exposure value compensation method (EC) for the calibration of automatic exposure controlled DSCs, which is simpler to use as it does not require availability of another

calibrated DSC. Results show that the EC method performs as well as the previous calibration methods and introduces < 2% uncertainty, which supports the validity of the EC method. The two smartphone DSCs used in this campaign cannot be calibrated through the EC method because they are older models that do not provide exposure value compensation settings. However, recent smartphone DSCs (e.g., iPhone 6 and Samsung Galaxy S7) provide such settings, making the EC method relevant to the current smartphone DSCs.

In terms of the effects of background colors and grayscale versus RGB pixel value (PV) measurements, we observe that background contrast is a more important factor than camera calibration in determining the uncertainty of opacity measurement. Dark gray roof background against white sky provides greater contrast than red background against white sky, thus opacity uncertainty is lower. We also observe that the contrast is wavelength dependent. In this study, due to lack of contrast in red PV when considering red background against white sky background, the uncertainty in opacity measurement in red PV is higher than in green or blue PVs. Even when using dark gray roof background against white sky background, where high contrast occurs for all red, green, and blue PVs, we show that opacity values measured in green and blue PVs are less deviated from those measured in grayscale PV (3.0%), compared to red PV (7.8%). The results concerning wavelength dependency implies that when grayscale PV does not provide the greatest contrast for select backgrounds, blue or green PV can be used as alternatives in determining opacity. The wavelength dependent contrast also leads to difference in diffusive scattering parameter (K) in the transmission model, when the background color is not in grayscale.

The results have implications for future research and technology deployment. In light of future research, backgrounds with other colors (such as green trees or blue sky) should be tested

to determine the wavelength dependence in opacity measurements and its uncertainty. In light of technology deployment, smartphone applications can be developed for measuring opacity using DOM, with background choices optimized to reduce uncertainty in opacity measurements.

5.6 References

Anenberg, S.C., Schwartz, J., Shindell, D., Amann, M., Faluvegi, G., Klimont, Z., Janssens-Maenhout, G., Pozzoli, L., Van Dingenen, R., Vignati, E., et al. (2012). Global Air Quality and Health Co-benefits of Mitigating Near-term Climate Change Through Methane and Black Carbon Emission Controls. *Environ. Health Perspect.* 120: 831–839.

Ångström, A. (1964). The Parameters of Atmospheric Turbidity. *Tellus* 1: 64–75.

Apple Inc. (2018). iPhone 8 – Technical Specifications. https://www.apple.com/iphone-8/specs (Accessed April 2018).

ASTM Standard D7520 (2013). *Standard Test Method for Determining the Opacity of a Plume in the Outdoor Ambient Atmosphere.* ASTM International, West Conshohocken, PA.

Bevington, P.R. and Robinson, D.K. (2002). *Data Reduction and Error Analysis for the Physical Sciences,* 3rd ed. McGraw-Hill.

Conner, W.D. and Hodkinson, J.R. (1972). *Optical Properties and Visual Effects of Smoke-Stack Plumes.* Office of Air Programs Publication No. AP-30, USEPA, Washington, DC.

Dockery, D.W. and Pope, C.A. (1994). Acute Respiratory Effects of Particulate Air Pollution. *Annu. Rev. Public Health* 15: 107–132.

Du, K. (2007). Optical Remote Sensing of Airborne Particulate Matter to Quantify Opacity and Mass Emissions. Ph.D. Dissertation, University of Illinois at Urbana-Champaign, Illinois, USA.

Du, K., Rood, M.J., Kim, B.J., Kemme, M.R., Franek, B., and Mattison, K. (2007). Quantification of Plume Opacity by Digital Photography. *Environ. Sci. Technol.* 41: 928–935.

Du, K., Shi, P., Rood, M.J., Wang, K., Wang, Y., and Varma, R.M. (2013). Digital Optical Method to Quantify the Visual Opacity of Fugitive Plumes. *Atmos. Environ.* 77: 983–989.

Du, K., Wang, Y., Chen, B., Wang, K., Chen, J., and Zhang, F. (2011). Digital Photographic Method to Quantify Black Carbon in Ambient Aerosols. *Atmos. Environ.* 45: 7113–7120.

Environment and Climate Change Canada (2010). New Source Emission Guidelines for Thermal Electricity Generation. https://www.ec.gc.ca/lcpe-cepa/default.asp?lang=En&n=8FCC2CCB-1 (Accessed August 2016).

Hasenfratz, D., Saukh, O., Sturzenegger, S., and Thiele, L. (2012). Participatory Air Pollution Monitoring Using Smartphones. In 2nd International Workshop on Mobile Sensing, April 16–20, 2012, Beijing, China.

Illinois EPA (2015). Evaluation of Visible Emissions Course. http://www.epa.illinois.gov/topics/air-quality/smoke-school/index (Accessed August 2016).

Jacobson, M. (2001). Global Direct Radiative Forcing Due to Multicomponent Anthropogenic and Natural Aerosols. *J. Geophys. Res.* 106: 1551–1568.

Malm, W.C. (1999). *Introduction to Visibility*. Colorado State University, Fort Collins, CO.

Montgomery, D.C. and Runger, G.C. (2011). *Applied Statistics and Probability for Engineers*, 5th ed. John Wiley & Sons, Inc.

Nieuwenhuijsen, M.J., Donaire-Gonzalez, D., Rivas, I., De Castro, M., Cirach, M., Hoek, G., Seto, E., Jerrett, M., and Sunyer, J. (2015). Variability in and Agreement between Modeled

and Personal Continuously Measured Black Carbon Levels Using Novel Smartphone and Sensor Technologies. *Environ. Sci. Technol.* 49: 2977–2982.

Poduri, S., Nimkar, A., and Sukhatme, G.S. (2010). Visibility Monitoring Using Mobile Phones. http://robotics.usc.edu/~mobilesensing/visibility/MobileAirQualitySensing.pdf (Accessed August 2016).

Pollution Control Department (2004). Thai Environmental Regulations - Air Quality and Noise Standards. http://www.pcd.go.th/info_serv/en_reg_std_airsnd03.html (Accessed August 2016).

Pope, C. and Dockery, D. (2006). Health Effects of Fine Particulate Air Pollution: Lines That Connect. *J. Air Waste Manag. Assoc.* 56: 709 –742.

Ramanathan, N., Lukac, M., Ahmed, T., Kar, A., Praveen, P.S., Honles, T., Leong, I., Rehman, I.H., Schauer, J.J., and Ramanathan, V. (2011). A Cellphone Based System for Large-scale Monitoring of Black Carbon. *Atmos. Environ.* 45: 4481–4487.

Reis, S., Seto, E., Northcross, A., Quinn, N.W.T., Convertino, M., Jones, R.L., Maier, H.R., Schlink, U., Steinle, S., Vieno, M., et al. (2015). Integrating Modelling and Smart Sensors for Environmental and Human Health. *Environ. Model. Softw.* 74: 238–246.

Samsung (2012). GT-I8190 – User Manual. http://downloadcenter.samsung.com/content/ UM/201212/20121204161700003/GT-I8190_UM_DTM_Jellybean_Eng_Rev.1.0_ 121204.pdf (Accessed April 2018).

Snyder, E.G., Watkins, T.H., Solomon, P.A., Thoma, E.D., Williams, R.W., Hagler, G.S.W., Shelow, D., Hindin, D.A., Kilaru, V.J., and Preuss, P.W. (2013). The Changing Paradigm of Air Pollution Monitoring. *Environ. Sci. Technol.* 47: 11369–11377.

USEPA (1993). *Visible Emissions Field Manual EPA Methods 9 and 22.* Office of Air Quality Planning and Standards, Washington, DC.

USEPA (2016). National Ambient Air Quality Standards (NAAQS). https://www.epa.gov/criteria-air-pollutants/naaqs-table (Accessed August 2016).

Vahlsing, C. and Smith, K.R. (2012). Global Review of National Ambient Air Quality Standards for PM_{10} and SO_2 (24 h). *Air Qual. Atmos. Health* 5: 393–399.

Watson, J.G. (2002). Visibility: Science and Regulation. *J. Air Waste Manag. Assoc.* 52: 628–712.

WHO (2006). *WHO Air Quality Guidelines for Particulate Matter, Ozone, Nitrogen Dioxide and Sulfur Dioxide.* WHO Press, Geneva, Switzerland.

CHAPTER 6: DAYTIME ATMOSPHERIC PLUME OPACITY MEASUREMENT USING A CAMCORDER

6.1 Abstract

Digital Optical Method (DOM) software, developed earlier to measure atmospheric plume opacity with digital still cameras, was tested with a camcorder, which captures digital images (as video frames) in visible light wavelengths at 30 Hz. The effect of contrast between two backgrounds when using DOM contrast model was demonstrated through the use of different pixel value measurement wavelengths and different background pairs. Unique contributions presented here are: 1) the camcorder is within the United States Environmental Protection Agency Method 9 individual and average opacity error limits, for black and white plumes with opacity values between 0% and 90%, while enabling real-time opacity measurements; 2) increasing contrast between two backgrounds decreases the opacity measurement error and uncertainty, with all measurements within Method 9 individual and average opacity error limits for contrast parameter ≥ 0.87; and 3) background choice affects the opacity measurement uncertainty more than camcorder calibration and number of pixels sampled for tested conditions. These contributions are important because they are the first demonstration and evaluation of applying digital image analysis with camcorders to quantify atmospheric plume opacity. Moreover, the results show that obtaining higher contrast between two backgrounds is the most important factor for reducing error in plume opacity measurements to meet acceptable performance criteria. This knowledge increases the reliability of image analysis to provide a low-cost and real-time monitoring method for quantifying atmospheric plume opacity.

6.2 Introduction

Environmental sensors that are low-cost and Internet-enabled are of interest because of their portability; ability for rapid data acquisition, transmission, storage, and analysis; and potential for crowdsourcing (Snyder et al., 2013). This research examines the applicability and uncertainty of using a low-cost (US$200 – 1,000), widely available, and real-time (30 Hz digital image capture) sensor to monitor atmospheric plume opacity from stationary point sources. Plume opacity is defined here as the percent of visible light attenuated by an atmospheric plume. Plume opacity relates to the concentration of particulate matter (PM) and the length of the observing path through the plume, and is measured for regulatory purposes because PM is an air pollutant that has impacts on human health (Pope and Dockery, 2006), reduces visibility (Watson, 2002), and affects climate (Anenberg et al., 2012). In 1974, the United States Environmental Protection Agency (USEPA) promulgated Method 9, specifying the use and performance requirements of trained human observers to measure plume opacity (USEPA, 1993). Before Method 9, plume opacity was evaluated by humans visually comparing the plume with Ringelmann Charts, which have five levels of density inferred from a grid of black lines on a white surface, and correspond to different opacity values (USEPA, 1993). Other countries such as Canada (Environment and Climate Change Canada, 2017), Taiwan (Environmental Protection Administration Executive Yuan, 2013), and South Korea (Ministry of Government Legislation, 2011) also regulate opacity, based on Method 9 or the Ringelmann Chart methods.

Methods using images from digital still cameras (DSCs) and software were developed to quantify plume opacity by McFarland et al. (2003, 2006, 2007) and Du et al. (2007a, 2007b, 2009). Use of DSCs and software to determine plume opacity offer improved measurement objectivity compared to human observers (Du et al., 2007a), reduce costs by US$200 million/yr

compared to Method 9 (Page, 2006), can separate measurement from analysis of the images to avoid potential conflicts of interest, and allow archiving of the digital images used to determine plume opacity for verification testing, reproducibility testing, and evidence for possible litigation that could occur years after the plume's opacity was measured. Use of DSCs and software to quantify atmospheric plume opacity was approved by ASTM International (ASTM Standard D7520, 2016) and by USEPA as Alternative Method ALT-082 (USEPA, 2012).

This research focuses on the Digital Optical method (DOM) that includes two models to accommodate different measurement situations: the contrast model, which applies when a plume is in front of and near two contrasting backgrounds, and the transmission model, which applies when a plume is in front of and near one background in contrast to the plume (Du, 2007). Field campaigns demonstrated that: 1) compact DSCs with DOM meet Method 9 performance requirements for measuring plume opacity values during daytime (Du et al., 2007a); 2) compact DSC positions relative to the sun and plume affect the resulting opacity values (Du et al., 2007b); 3) opacity values measured by compact DSCs have lower error than measurements from human observations (Du et al., 2007b); 4) compact DSCs can measure opacity values during nighttime over a range of more limited opacity values than required by Method 9 (Du et al., 2009); 5) compact DSCs with DOM can determine the opacity values of fugitive PM emissions (Du et al., 2013); and 6) smartphone DSCs with DOM can measure plume opacity values while meeting Method 9 error requirements, and background conditions were identified as important for determining opacity measurement errors and uncertainties (Yuen et al., 2017).

This research is motivated by the potential of commercial camcorders (i.e., video camera recorders) operating at visible light wavelengths to provide low-cost (US$200 – 1,000) real-time opacity measurements, since commercial camcorders are easily available to capture video frames

(digital images that form a video) at high frequencies of 24, 25, or 30 Hz (Chaney, 2016). Measurements at 30 Hz, as used to complete this research will be referred to as real time in the following text. This research examines the applicability of DOM to quantify plume opacity with a digital camcorder by extracting frames from the resulting video at up to 1 Hz, and then applying DOM to each frame to determine plume opacity values. Such real-time opacity measurement has the potential to provide improved opacity measurements by averaging opacity values during multiple seconds, instead of basing opacity values on one instantaneous image obtained by a DSC, or a human observation once every 15 seconds (ASTM Standard D7520, 2016). Currently, ASTM Standard D7520 and ALT-082 only apply to DSCs, and no methods are proposed for camcorders in measuring/monitoring plume opacity. This research serves as the first demonstration that camcorders can measure plume opacity with DOM. Although this research focuses on the use of a camcorder, there are advanced DSCs that offer "burst mode" which can capture digital images at 1 – 5 Hz and can serve a similar purpose for real-time opacity monitoring.

In the following sections, we describe the methods and results of applying DOM on camcorder frames. Unique contributions of this paper are: 1) a camcorder can accurately measure a wide range of opacity values (0% – 90%) and in real-time (1 Hz) for white and black plumes during daytime; 2) opacity measurement error and uncertainty, when using the contrast model, decreases as the color contrast between two backgrounds increases; and 3) opacity measurement uncertainty due to background choice is more than due to camcorder calibration and number of sampled pixels. These contributions are important because: 1) they are the first demonstration of applying digital image analysis software with a camcorder to quantify atmospheric plume opacity; and 2) they show that obtaining higher contrast between two backgrounds is the most

important for reducing error in plume opacity measurements to meet acceptable performance criteria. This knowledge increases the reliability of image analysis to provide a low-cost and real-time monitoring method for quantifying atmospheric plume opacity.

6.3 Methods

Camcorder and Its Calibration

A Canon Vixia HF R20 camcorder (US$300) was used to capture high-definition videos (1080p format), where real-time frames were extracted. Each frame consists of two-dimensional arrays of pixel values (PVs) of the plumes and their backgrounds. The camcorder was calibrated to provide the correspondence between relative exposure (exposure relative to camcorder exposure setting) and PVs, before the field measurements. Calibration was performed by extracting one frame of the same white surface for each compensated exposure value set by the camcorder, and measuring the corresponding PVs in grayscale and in red, green, or blue (RGB) (Yuen et al., 2017). The calibration was repeated three times to determine the opacity measurement uncertainty due to camcorder calibration. The wavelengths with peak light transmittance for RGB filters depend on the DSC or the camcorder, but in general they were 590 nm – 610 nm for red, 520 nm – 540 nm for green, and 450 nm – 480 nm for blue among tested DSCs in an experiment (Mauer, 2009). Grayscale PV is a weighted average of RGB PVs in accordance with Recommendation BT.601 (International Telecommunication Union, 2011).

Field Campaign

Field experiments were performed in July 2013, in Springfield, Illinois, USA, during a daytime Illinois EPA visible emission evaluation training course (i.e., smoke school) (Illinois EPA, 2015). A smoke generator produced either black or white plumes from an elevated stack that was 4 m high and with a 0.30 m inner diameter. A white-light transmissometer operated by Illinois EPA, located inside the stack, monitored plume opacity at 15 Hz and served as the

reference for comparison with the camcorder's opacity values. The camcorder was set to capture frames at 30 Hz, and was pointed toward the plume such that the sun was within 140° sector behind the camcorder, as per Method 9 and ASTM requirements, and was located 1 m above the ground and 20 m from the smoke generator.

Opacity Measurement Performance by Camcorder with Respect to Method 9 IOE and AOE Limits

To examine whether the camcorder meets Method 9 performance requirements with respect to the IOE and AOE limits, videos of black and white plumes with the dark gray (a roof) and white (overcast sky) backgrounds were captured. This background pair was chosen among the available ones at the field campaign because it provided the highest color contrast between two backgrounds, as quantified by PV. Besides, the same dark gray and white background pair was used in previous research to benchmark compact and smartphone DSCs' abilities to measure plume opacity (Du et al., 2007a; Yuen et al., 2017). The arithmetic mean values of grayscale and RGB PVs were calculated to quantify the background color for the two backgrounds, while the standard deviations and coefficient of variations (COVs) of grayscale and RGB PVs were calculated to quantify the background color uniformity for the two backgrounds. Individual frames for black and white plumes were extracted from the videos at two-minute intervals for the entire measurement period (10:55 am – 12:59 pm for black plumes, 4:07 pm – 5:47 pm for white plumes, as determined by field conditions), resulting in 63 frames for black plumes and 51 frames for white plumes. This allowed capturing a wide range of opacity values for examining the camcorder's measurement performance. Individual frames for black and white plumes were also extracted at 1 Hz for a one-minute video segment (60 frames total), so that the real-time opacity measurement performance could be tested. The individual frames, extracted at two-minute interval and 1 Hz, were then analyzed by DOM's contrast model. With this model, four rectangular regions of interest (ROI) are selected in each frame: two ROIs with the plume in

front of dark gray and white backgrounds, and two ROIs next to but without the plume in front of the dark gray and white backgrounds. Each ROI has between 100 and 2,500 pixels, so that opacity measurement uncertainty due to number of pixels sampled can be quantified. The PVs within these four ROIs are each arithmetically averaged, and converted into relative exposures through the camcorder calibration. Plume opacity for each extracted frame was then calculated by Eq. (5.1) (Yuen et al., 2017).

$$O_c = 1 - \frac{\frac{E_{wp}}{E_w} - \frac{E_{bp}}{E_w}}{1 - \frac{E_b}{E_w}} \tag{5.1}$$

where O_c = plume opacity using contrast model; E_{wp} = amount of exposure caused by the bright background with plume; E_w = amount of exposure caused by the bright background without plume; E_{bp} = amount of exposure caused by the dark background with plume; and E_b = amount of exposure caused by the dark background without plume. In the case of dark gray and white background pair, the bright background is white background and the dark background is dark gray background.

Method performance using the camcorder to measure opacity values was evaluated by comparing opacity values measured by the camcorder with the opacity values measured by the reference transmissometer. Since previous DSC opacity measurements (Du et al., 2007a, 2007b, 2009) considered grayscale only, for the purpose of consistent performance comparison with the previous results, only camcorder's grayscale PVs were considered. As per Method 9, metrics for performance comparison are Individual Opacity Errors (IOEs), which are the absolute opacity difference between the camcorder's and transmissometer's individual measurements, and Average Opacity Errors (AOEs), which are the average of IOEs. The IOE values of all of the

frames of plumes are required to be ≤ 15% opacity, and AOE values are required to be ≤ 7.5% opacity to meet Method 9 performance requirements (USEPA, 1993). As previously stated, the numbers of frames used in this experiment are 63 for black plumes and 51 for white plumes. These numbers are greater than the Method 9 requirements of 25 black plumes and 25 white plumes for one successful test (USEPA, 1993).

Effect of Background Color Contrast on Opacity Measurement Errors and Uncertainties

The opacity measurement uncertainty by a DSC or camcorder comes from the following sources: 1) calibration of DSC or camcorder; 2) number of pixels sampled for each ROI; 3) background color uniformity; and 4) contrast between two background colors (when using the contrast model).

The opacity measurement uncertainty due to camcorder calibration (uncertainty source 1) was determined using the method described in Yuen et al. (2017), but replacing the DSC with the camcorder. In summary, the calibration curve of the camcorder was determined three times, and opacity values of the same frame were calculated using the calibration triplicates and Eq. (5.1). The maximum absolute opacity differences among the triplicates, when considering grayscale and RGB, are considered as the opacity measurement uncertainty due to camcorder calibration. The opacity measurement uncertainty due to the number of sampled pixels (uncertainty source 2) was determined by setting each ROI as squares with both sides ranging from 3 pixels (9 pixels total) to 50 pixels (2,500 pixels total) to analyze one select frame. This range of pixel number is chosen to cover the number range of sampled pixels for each ROI in each frame analyzed to determine opacity values with DOM in this research, which is between 100 and 2,500 pixels. For each size of ROI, opacity values were replicated 10 times by moving the ROIs, and calculating the corresponding opacity values. The means and standard deviations for the replicates were then calculated for each size of ROI. As previously stated, the arithmetic means were used to observe

the consistency of opacity measurement, while the standard deviations were used to determine the opacity measurement uncertainty due to number of sampled pixels.

To test the effect of background color uniformity (uncertainty source 3) and contrast between two background colors (uncertainty source 4) on the resulting opacity values, a different background set, which included white (overcast sky), red (a sign), and black (a pole) backgrounds, was used to measure plume opacity values. The different background set was intended for the camcorder to capture a frame with three backgrounds with different uniformity and color. The orientation of the camcorder was adjusted, so that the videos captured frames with plumes passing partially in front of all these backgrounds. Only white plume results were considered in this part of the analysis because black plumes were entirely in front of the black background, due to the change in wind direction, which prevented the use of contrast model with the black background. Twenty-five (25) individual frames for white plumes were extracted at two-minute intervals from the video captured between 9:19 am and 10:07 am. Similar to the measurements described in the previous section, the background color was quantified by calculating the arithmetic mean of PVs and the background color uniformity was quantified by calculating the standard deviation and COV of PVs, for each of the red and black backgrounds in these frames in terms of grayscale and RGB PVs. The arithmetic mean, standard deviation, and COV of PVs for white background were determined based on results from measurements described in the previous section. DOM (Eq. (5.1)) was then used to calculate plume opacity values three times per individual frame, by using different two out of three background combinations (i.e., white and black, white and red, and red and black). The assignment of bright and dark backgrounds in Eq. (5.1) is as follows (Table 6.1):

Table 6.1. Assignment of bright and dark backgrounds in Eq. (5.1) for the three background combinations.

Background pair	Bright background	Dark background
White and black	White	Black
White and red	White	Red
Red and black	Red	Black

The opacity measurement uncertainty due to background color contrast and background color uniformity was determined by using an error propagation approach with Eq. (5.1) (Yuen et al., 2017). This opacity measurement uncertainty is calculated by Eq. (5.6).

$$\delta O_c = \left| \frac{1}{E_w - E_b} \right| \sqrt{\left(\delta E_{wp}{}^2 + \delta E_{bp}{}^2\right) + \left(1 - O_c\right)^2 \left(\delta E_w{}^2 + \delta E_b{}^2\right)} \tag{5.6}$$

where δO_c = opacity measurement uncertainty due to background color contrast and uniformity, using DOM contrast model; δE_{wp} = uncertainty of exposure caused by the bright background with plume; δE_w = uncertainty of exposure caused by the bright background without plume; δE_{bp} = uncertainty of exposure caused by the dark background with plume; and δE_b = uncertainty of exposure caused by the dark background without plume.

Note that E_w-E_b in Eq. (5.6) describes the background color contrast, while δE_{wp}, δE_w, δE_{bp}, and δE_b describe color uniformity of each background with or without plume. To find δE_{wp}, δE_w, δE_{bp}, and δE_b, the differences between the exposures that correspond to the measured PVs and the exposures that correspond to the measured PVs plus standard deviations of PVs, using the camcorder's response curve, were calculated (Yuen et al., 2017). Opacity calculations and their measurement uncertainty analyses were completed in grayscale PVs and RGB PVs for each of the three background pairs.

To further examine the relationship of background contrast against IOE and AOE, the contrast between two backgrounds was quantified as contrast parameter, which is defined as 1-(E_b/E_w) and is the denominator of Eq. (5.6) normalized by E_w. The contrast parameter is between

0 and 1, with 1 being the highest contrast and 0 being the lowest contrast. This parameter is calculated by using measured PVs of the backgrounds in the frames captured by the camcorder.

6.4 Results and Discussion

Means, standard deviations, and coefficient of variations (COVs) of PVs for the dark gray background (a roof), the white background (overcast sky), the red background (a sign), and the black background (a pole), measured by the camcorder, are shown in Table 6.2. The means of PVs show the colors of the backgrounds when considering the RGB PVs. The standard deviations and COVs of PVs show the background color uniformity. The standard deviations of PVs are between 7 and 16 for all the tested backgrounds. The COVs of PVs are between 5% and 54%. Black background has the highest COVs of PVs in grayscale and RGB (41% – 54%), while white background has the lowest COVs of PVs in grayscale and RGB (5% – 8%). This suggests that darker background color tends to be less uniform for conditions tested here. Values in Table 6.2 affect the opacity measurement uncertainty calculations that involve background color contrast and uniformity, which will be discussed in Section 6.3 “Effect of background color contrast on pacity measurement errors and uncertainties”.

Table 6.2. Means, standard deviations, and coefficients of variations (COVs) of PVs of the dark gray background (a roof), the white background (overcast sky), the red background (a sign), and the black background (a pole), measured by the camcorder. A PV of 0 is the darkest, while a PV of 255 is the brightest for the specific color. The smaller the standard deviation or COV, the more uniform the background color is. Dark gray and white backgrounds were used in measurements described in Section 6.2 "Opacity measurement performance by camcorder with respect to Method 9 IOE and AOE limits", and white, red, and black backgrounds were used in measurements described in Section 6.2 "Effect of background color contrast on opacity measurement errors and uncertainties".

Background Color			**Dark Gray**	**White**	**Red**	**Black**
Number of Frames Analyzed for Background PV (-)			51	51	25	25
Wavelength of PV	Grayscale	Mean (-)	56	200	92	20
		Standard Deviation (-)	14	14	8	9
		COV (%)	25	7	9	45
	Red	Mean (-)	60	196	205	22
		Standard Deviation (-)	16	15	13	9
		COV (%)	27	8	6	41
	Green	Mean (-)	54	200	40	19
		Standard Deviation (-)	14	13	7	9
		COV (%)	26	7	18	47
	Blue	Mean (-)	51	203	61	24
		Standard Deviation (-)	12	11	9	13
		COV (%)	24	5	15	54

COV = Coefficient of Variation

Opacity Measurement Performance by Camcorder with Respect to Method 9 IOE and AOE Limits

The comparisons between the camcorder's and the transmissometer's measured opacity values of black and white plumes, of frames extracted at two-minute interval for the entire measurement period and at 1 Hz for a one-minute video segment, are shown in Figure 6.1 (A and B) and Figure 6.1 (C and D), respectively. The ranges of opacity values measured by the transmissometer are 0% – 95% (black plumes) and 0% – 90% (white plumes) for two-minute interval measurements during the entire measurement period, and 10% – 90% (black plumes) and 10% – 50% (white plumes) for 1 Hz measurements in a one-minute video segment. The camcorder's and transmissometer's opacity values versus time are shown in Figure 6.2 to

compare the camcorder's real-time opacity measurements with the transmissometer's measurements. Number of pixels sampled within each ROI is between 1,000 and 2,500.

Figure 6.1. Camcorder versus in-stack transmissometer opacity values with dark gray and white background pair for (A) black and (B) white plumes at two-minute interval, and (C) black and (D) white plumes at 1 Hz. The 1:1 solid line shows perfect agreement in measurements, while the dashed lines correspond to ± 15% IOE.

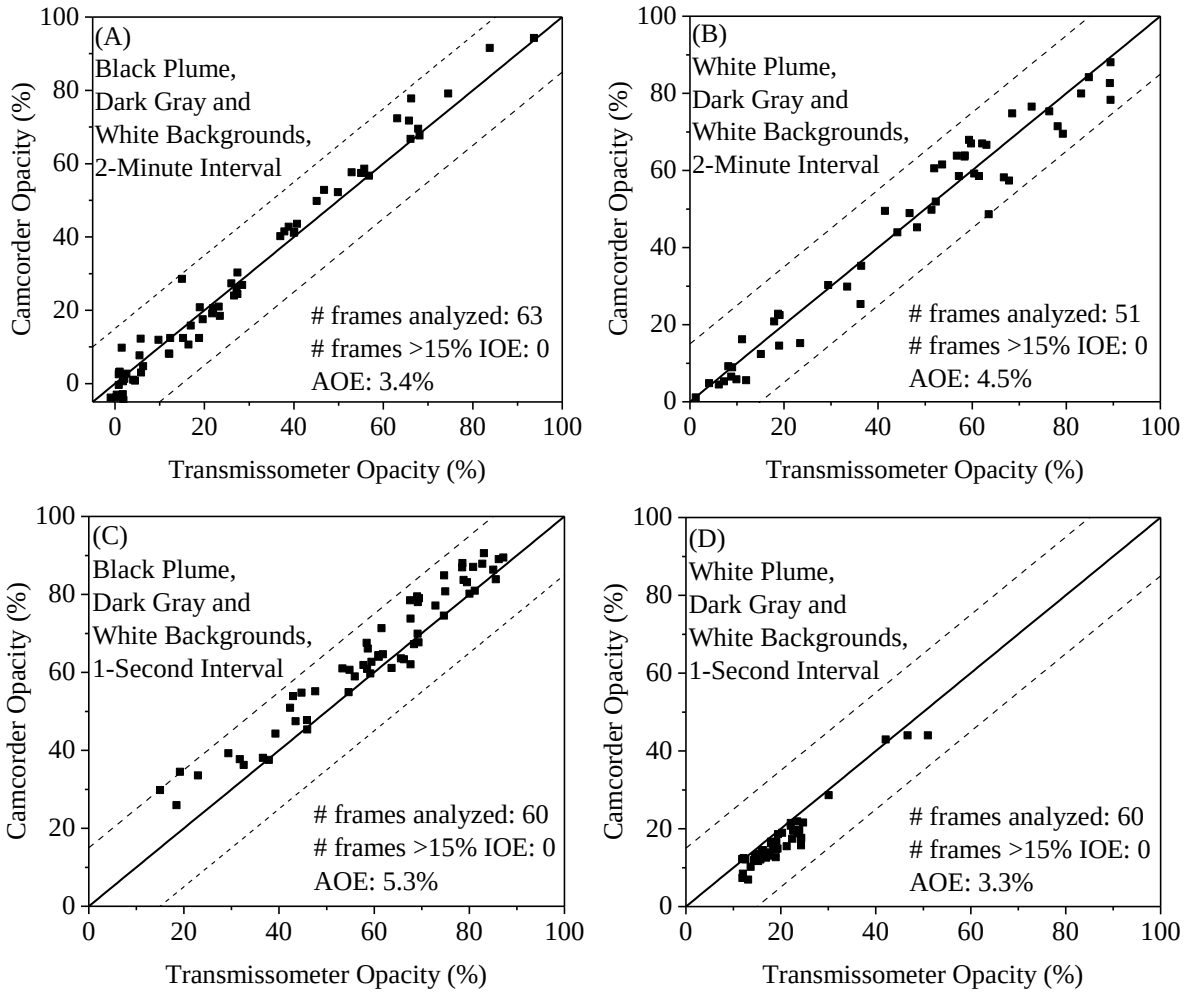

Figure 6.2. Opacity values measured by the camcorder and the in-stack transmissometer versus time for (A) black and (B) white plumes with dark gray and white background pair at 1 Hz.

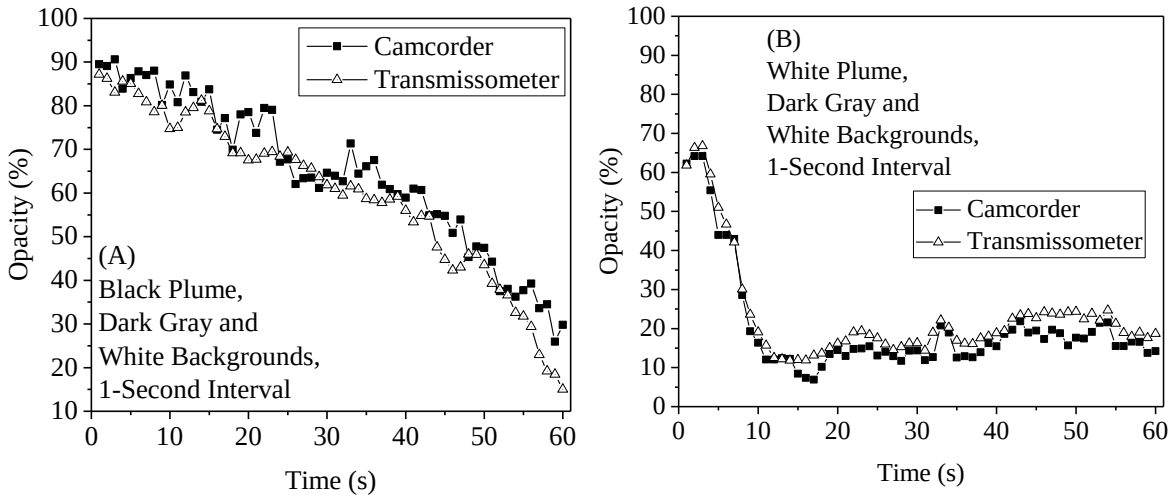

The maximum IOEs for black plumes and white plumes are 14% and 15%, respectively, for 2-minute interval, and 15% and 10%, respectively, for 1 Hz. The AOEs for black plumes and white plumes are 3.4% and 4.5%, respectively, for 2-minute interval, and 5.3% and 3.3%, respectively, for 1 Hz. IOEs are all ≤ 15% and AOEs are all ≤ 7.5% for both black and white plumes for the two-minute interval and 1 Hz measurements presented in Figure 6.1, using at least 51 consecutive frames as previously described. The results for two-minute interval measurements indicate that camcorder measurements are within Method 9 IOE and AOE limits in measuring plume opacity values between 0% and 90%, the range of opacity values measured by the transmissometer during this experiment. The results for 1 Hz measurements show that the camcorder is within Method 9 IOE and AOE limits when it is used for real-time opacity measurements.

Effect of Background Color Contrast on Opacity Measurement Errors and Uncertainties

As previously discussed, comparisons of the camcorder's and the transmissometer's measured opacity values for 25 frames captured at a two-minute interval, using different background pairs and calculated by grayscale and RGB PVs, are shown in Figure 6.3. As

previously explained, the comparison of backgrounds was only performed on white plumes due to changes in meteorological conditions during the tests. The relationship between contrast parameter values between two backgrounds and their IOE and AOE values for white plumes is shown in Figure 6.4 to show the arithmetic means of IOE values for each PV color and background pair. The IOE and AOE values are displayed in logarithmic scale in Figure 6.4 to display extreme values. The ranges of number of pixels sampled in each ROI, contrast parameter values, % of frames > 15% IOE, and AOE values for each PV color and background pair are tabulated in Table 6.3.

Figure 6.3. Camcorder versus in-stack transmissometer opacity values for white plumes with select background pairs at two-minute intervals. Number of frames analyzed is 25 for each background pair.

(A) White and black backgrounds

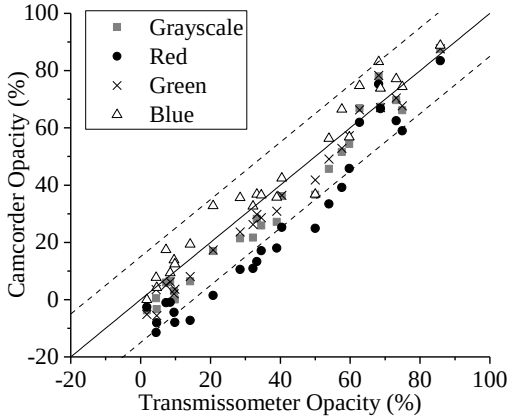

(B) White and red backgrounds

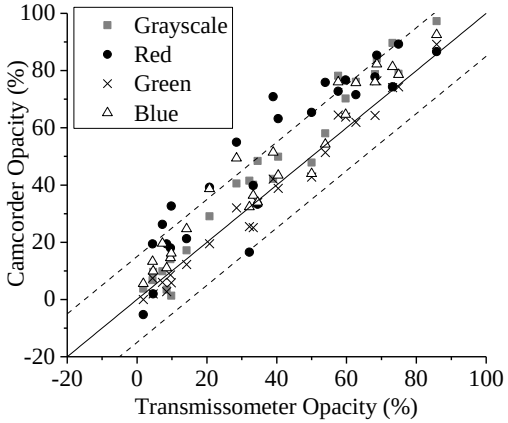

(C) Red and black backgrounds

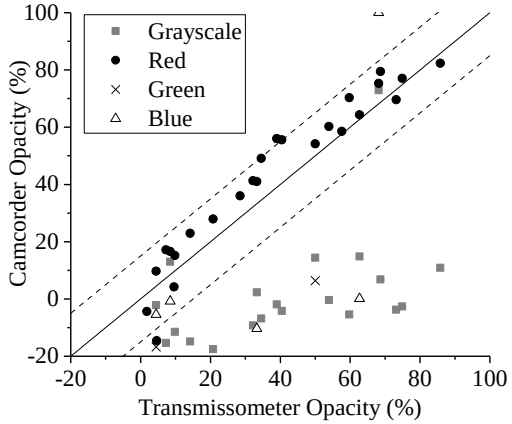

Figure 6.4. (A) IOE values versus the contrast parameters between background pairs for all tested PV color and background pairs. Dash line shows 15% IOE, the limit value for the measurements to pass Method 9 IOE requirements. Solid line shows regression between AOE and contrast parameter. Grayscale, red, green, and blue are referred to the PV colors. W = white background, B = black background, and R = red background. In the regression, y = AOE and x = contrast parameter. (B) Similar to (A), but for AOE values (arithmetic mean of 25 IOE values). Dash line shows 7.5% AOE, the limit value for the measurements to pass Method 9 AOE requirements.

(A) (B)

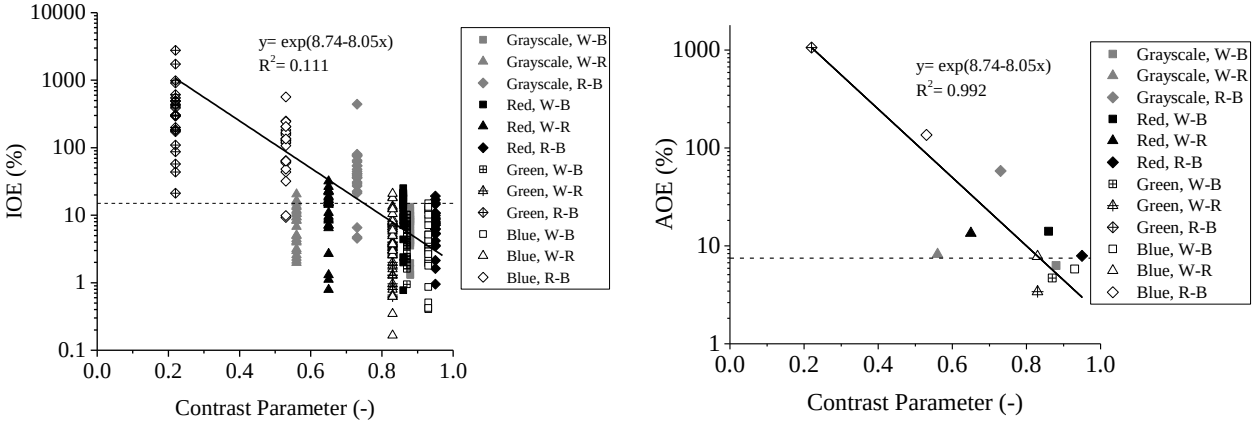

Table 6.3. Ranges of number of pixels sampled in each ROI, contrast parameter values, % of frames > 15% IOE, and AOE values for two-minute interval white plume opacity measurements (25 total frames) using the camcorder's grayscale and RGB PVs, when using contrast model with select backgrounds.

Background pair	Range of number of pixels sampled in each ROI	Color of PV	Contrast parameter	% of frames > 15% IOE	AOE (%)
White and black	100 – 2,500	grayscale	0.88	0	6.3
		Red	0.86	56	14.1
		Green	0.87	0	4.7
		Blue	0.93	0	5.8
White and red	1,000 – 2,500	grayscale	0.56	12	8.2
		Red	0.65	48	13.5
		green	0.83	0	3.4
		blue	0.83	12	7.8
Red and black	100 – 2,500	grayscale	0.73	88	58.3
		Red	0.95	12	7.9
		green	0.22	100	1063.4
		blue	0.53	92	136.3

These results show that IOE and AOE values decrease with increasing contrast between background pairs. Regression analysis of Figure 6.4 shows that IOE and AOE correlate with contrast parameter exponentially, with $R^2 = 0.11$ for IOE and $R^2 = 0.99$ for AOE, for all tested PV color and background pairs. From Table 6.3, Opacity measurements are within the Method 9 IOE limit (i.e., all IOEs ≤ 15% opacity) and AOE limit (i.e., AOE ≤ 7.5% opacity) when the contrast parameter is ≥ 0.87. The exception is red PV with red and black background pair, with contrast parameter of 0.95 but with IOE and AOE requirements failed. The results also show that different PV colors result in different background color contrast. This is important because it shows that background contrast can be optimized by selecting the appropriate PV color for measurement, in order to be within the current Method 9 IOE and AOE limits. For example, when using the white and red backgrounds, using grayscale PV has a contrast parameter of 0.56, and the resulting opacity measurement is not within the IOE and AOE limits. Using the same background pair with green PV, however, has a contrast parameter of 0.83, which results in opacity measurement being within the IOE and AOE limits.

The opacity measurement uncertainty due to camcorder calibration is shown in Table 6.4. The opacity measurement uncertainty due to camcorder calibration is ≤ 3.3%, except for the red and black backgrounds for white plumes. The high opacity measurement uncertainty for red and black backgrounds with white plume (15904.6%) can be attributed to the lack of contrast between the two backgrounds. According to Eq. (5.1), when E_b is similar to E_w (lack of contrast between two backgrounds), the denominator approaches zero. This subsequently results in opacity values > 100% as well as their uncertainties.

Table 6.4. Maximum absolute opacity differences among triplicate calibration curves that represent the opacity measurement uncertainty due to camcorder calibration. The maximum considers the difference for all grayscale and RGB PVs.

Plume color	Background	Camcorder maximum absolute opacity difference (%)
Black	Dark gray and white	0.9
White	Dark gray and white	1.3
White	White and black	3.3
White	White and red	0.8
White	Red and black	15904.6

The relationship of number of sampled pixels for each ROI to the mean and standard deviation of grayscale opacity values for one frame is shown in Figure 6.5. The mean opacity value is 55% when rounded to the nearest 5%, the reporting accuracy for Method 9 (USEPA, 1993), when the number of pixels is between 25 and 2,500 for each ROI. Within this range of number of pixels, the mean opacity values are not significantly different ($p = 0.052 > 0.05$ when using One-Way ANOVA test (Montgomery and Runger, 2011)). This shows that camcorder with DOM measures consistent opacity values when > 25 pixels are sampled for each ROI for the field conditions tested here. The standard deviation of opacity values decreases from 2.5% to 1.0% when the number of sample pixels increases from 25 to 2,500 for each ROI. When sampling 9 pixels for each ROI, the mean opacity value begins to differ (50% when rounded to the nearest 5%), and the standard deviation becomes 4.6%. The mean opacity values for 9 and 25 pixels are significantly different ($p = 0.006 < 0.05$ when using One-Way ANOVA test). The standard deviation of opacity values is considered as the opacity measurement uncertainty due to number of sample pixels. Therefore, the result shows that the opacity measurement uncertainty due to number of sampled pixels is < 2.5% as long as > 25 pixels are sampled in each ROI. As previously stated, a minimum of 100 pixels were sampled for each ROI for all frames, so the opacity measurement uncertainty due to number of sampled pixels is < 2.5% as well.

Figure 6.5. Relationship of number of sampled pixels for each ROI to the mean and standard deviation of grayscale opacity values for one frame. The squares show the means and the vertical lines show the standard deviations.

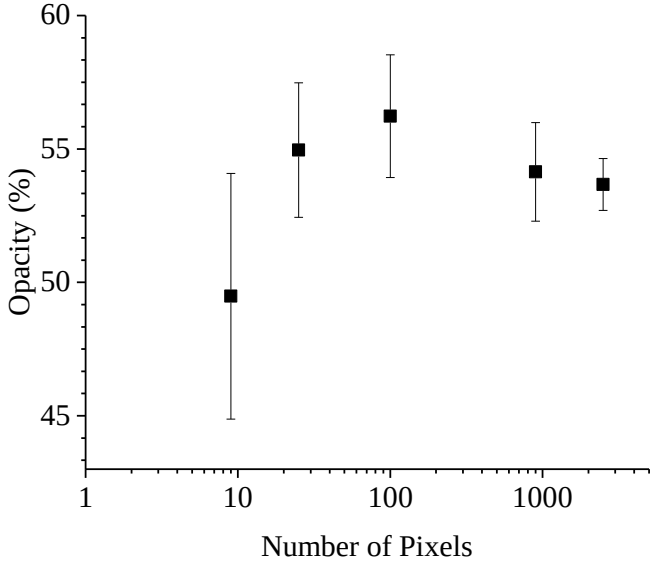

Calculated opacity uncertainties for white plumes due to background color uniformity and contrast between the selected background combinations are shown in Figure 6.6. The calculated opacity uncertainties are displayed in logarithmic scale to display extreme values. The results in Figure 6.6 show that: 1) for white and black background pair, the calculated median opacity measurement uncertainty is 3% – 6% among the four PV colors, with red PV having the highest uncertainty and blue PV having the lowest uncertainty; 2) for white and red background pair, the calculated median opacity measurement uncertainty is 4% – 8% among the four PV colors, with grayscale PV having the highest uncertainty and blue PV having the lowest uncertainty; and 3) for red and black background pair, the calculated median opacity measurement uncertainty is 3% – 124% among the four PV colors, with green PV having the highest uncertainty and red PV having the lowest uncertainty. In accordance with Eq. (5.6), lower contrast between two backgrounds leads to higher opacity measurement uncertainty due to background colors. This explains why red and black background pair leads to the highest opacity measurement uncertainty due to background colors, and why such uncertainty values agree with

the trend in IOE and AOE values shown in Figure 6.4 that lower background contrast results in higher IOE and AOE values.

Figure 6.6. Uncertainties of white plume opacity measurements due to background color contrast between background pairs.

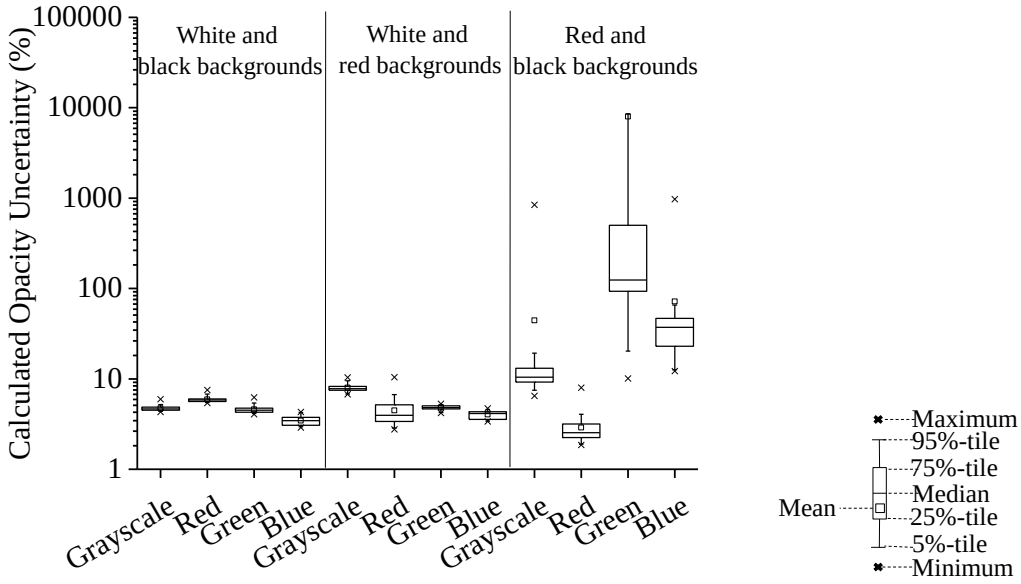

6.5 Conclusions

A digital camcorder, capturing videos at 30 Hz frame rate, measured plume opacity in real-time during daytime for white and black plumes. The camcorder met Method 9 individual opacity error (IOE) and average opacity error (AOE) requirements with respect to their limits, for plumes with opacity values between 0% and 90% (range of opacity values available for testing), when using the contrast model of the Digital Optical Method (DOM) and the dark gray and white background pair. Frames for these tests were extracted in two-minute interval during the entire measurement period, and in 1 Hz in one-minute video segments. IOE values for all frames are ≤ 15 % opacity and AOE values for all measurement conditions are ≤ 5.1% for white and black plumes measured in these two time intervals. This shows the ability of the camcorder to measure opacity in real-time below Method 9 IOE and AOE limits over the range of available

opacity values that existed during the tests. It is recommended to consider the ASTM D7520 certification standards for digital still cameras to measure plume opacity to be extended for camcorders.

When using background pairs of different colors to measure plume opacity, results show that increasing the contrast between these different colors decreases IOE and AOE values. It is important to increase color contrast between two backgrounds to reduce opacity measurement uncertainty and error, which can be done by choosing appropriate backgrounds or by using appropriate measurement wavelengths of the camcorder.

The opacity measurement uncertainty due to camcorder calibration is < 3.3%. The opacity measurement uncertainty due to number of sampled pixels is determined to be < 2.5% when > 25 pixels are sampled. The opacity measurement uncertainty due to background color uniformity and contrast is between 3% and 124%, depending on the background choice and measurement PV color. Based on the above opacity measurement uncertainty results, background choice is the most important factor that determines the opacity measurement uncertainty.

The contributions stated above are important because: 1) they are the first demonstration of applying DOM software with a camcorder to quantify atmospheric plume opacity; and 2) they show that obtaining higher contrast between two backgrounds is the most important for reducing error in plume opacity measurements to meet acceptable performance criteria. This knowledge increases the reliability of image analysis to provide a low-cost and real-time monitoring method for quantifying atmospheric plume opacity.

6.6 References

Anenberg, S.C., Schwartz, J., Shindell, D., Amann, M., Faluvegi, G., Klimont, Z., Janssens-

Maenhout, G., Pozzoli, L., Van Dingenen, R., Vignati, E., et al. (2012). Global Air Quality and Health Co-benefits of Mitigating Near-term Climate Change Through Methane and Black Carbon Emission Controls. *Environ. Health Perspect.* 120: 831–839.

ASTM Standard D7520 (2016). Standard Test Method for Determining the Opacity of a Plume in the Outdoor Ambient Atmosphere. ASTM International, West Conshohocken, PA.

Chaney, M. (2016). Video Frame Rates (24p, 25p, 30p, 60i). http://www.steves-digicams.com/knowledge-center/video-frame-rates-24p-25p-30p-60i.html. (Accessed February 2018).

Du, K. (2007). Optical Remote Sensing of Airborne Particulate Matter to Quantify Opacity and Mass Emissions. Ph.D. Dissertation, University of Illinois at Urbana-Champaign, Illinois, USA.

Du, K., Rood, M.J., Kim, B.J., Kemme, M.R., Franek, B., and Mattison, K. (2007a). Quantification of Plume Opacity by Digital Photography. *Environ. Sci. Technol.* 41: 928–935.

Du, K., Rood, M.J., Kim, B.J., Kemme, M.R., Franek, B., and Mattison, K. (2009). Evaluation of Digital Optical Method to Determine Plume Opacity During Nighttime. *Environ. Sci. Technol.* 43: 783–789.

Du, K., Rood, M.J., Kim, B.J., Kemme, M.R., Franek, B.J., Mattison, K., and Cook, J. (2007b). Field Evaluation of Digital Optical Method to Quantify the Visual Opacity of Plumes. *J. Air Waste Manage. Assoc.* 57: 836–844.

Du, K., Shi, P., Rood, M.J., Wang, K., Wang, Y., and Varma, R.M. (2013). Digital Optical Method to Quantify the Visual Opacity of Fugitive Plumes. *Atmos. Environ.* 77: 983–989.

Environment and Climate Change Canada (2017). New Source Emission Guidelines for Thermal

Electricity Generation. https://www.ec.gc.ca/lcpe-cepa/default.asp?lang=En&n=8FCC2CCB-1. (Accessed February 2018).

Environmental Protection Administration Executive Yuan (2013). Stationary Pollution Source Air Pollutant Emissions Standards. https://oaout.epa.gov.tw/law/EngLawContent.aspx?lan=E&id=116&KW=stationary+pollution+source. (Accessed February 2018).

Illinois EPA (2015). Evaluation of Visible Emissions Course. http://www.epa.illinois.gov/topics/air-quality/smoke-school/index. (Accessed February 2018).

International Telecommunication Union (2011). Studio Encoding Parameters of Digital Television for Standard 4:3 and Wide-screen 16:9 Aspect Ratios (ITU-R BT.601-7). 19.

Jacobson, M. (2001). Global Direct Radiative Forcing Due to Multicomponent Anthropogenic and Natural Aerosols. *J. Geophys. Res.* 106: 1551–1568.

Mauer, C. (2009). Measurement of the Spectral Response of Digital Cameras with a Set of Interference Filters. Ph.D. Dissertation, University of Applied Sciences Cologne, Germany.

McFarland, M.J., Olivas, A.C., Atkins, S.G., Kennedy, R.L., and Patel, K. (2007). Fugitive Emissions Opacity Determination Using the Digital Opacity Compliance System (DOCS). *J. Air Waste Manage. Assoc.* 57: 1317–1325.

McFarland, M.J., Rasmussen, S.L., Stone, D.A., Palmer, G.R., and Wander, J.D. (2006). Validation of the Digital Opacity Compliance System Under Regulatory Enforcement Conditions. *J. Air Waste Manage. Assoc.* 56: 1260–1266.

McFarland, M.J., Terry, S.H., Stone, D. a., Rasmussen, S.L., and Calidonna, M.J. (2003). Evaluation of the Digital Opacity Compliance System in High Mountain Desert

Environments. *J. Air Waste Manage. Assoc.* 53: 724–730.

Ministry of Government Legislation (2011). Clean Air Conservation Act, Enforcement Rules (Annex 8, In Korean).

Montgomery, D.C. and Runger, G.C. (2011). Applied Statistics and Probability for Engineers 5th ed. John Wiley & Sons, Inc.

Page, S.D. (2006). New Digital Camera Approach, USEPA, OAQPS, Correspondence.

Pope, C.A. and Dockery, D.W. (2006). Health Effects of Fine Particulate Air Pollution: Lines That Connect. *J. Air Waste Manag. Assoc.* 56: 709–742.

Snyder, E.G., Watkins, T.H., Solomon, P.A., Thoma, E.D., Williams, R.W., Hagler, G.S.W., Shelow, D., Hindin, D.A., Kilaru, V.J., and Preuss, P.W. (2013). The Changing Paradigm of Air Pollution Monitoring. *Environ. Sci. Technol.* 47: 11369–77.

USEPA (1993). Visible Emissions Field Manual EPA Methods 9 and 22. Office of Air Quality Planning and Standards, Washington, DC.

USEPA (2012). Approved Alternatives. https://www.epa.gov/emc/broadly-applicable-approved-alternative-test-methods. (Accessed February 2018).

Watson, J.G. (2002). Visibility: Science and Regulation. *J. Air Waste Manag. Assoc.* 52: 628–712.

Yuen, W., Gu, Y., Mao, Y., Koloutsou-Vakakis, S., Rood, M.J., Son, H.-K., Mattison, K., Franek, B., and Du, K. (2017). Performance and Uncertainty in Measuring Atmospheric Plume Opacity Using Compact and Smartphone Digital Still Cameras. *Aerosol Air Qual. Res.* 17: 1281–1293.

PART IV: SUMMARY

CHAPTER 7: SUMMARY

7.1 Unique Contributions and Importance of the Optical Remote Sensing (ORS) Research

First, an active ORS method using micropulse lidar (MPL) is discussed in Part II (Chapters 2 to 4), which is used to measure fugitive particulate matter (PM) plume and calculate its emission factor (EF). The ORS method is useful in measuring fugitive PM because MPL is capable of real-time and range-resolved measurements, so multiple point measurement sensors are avoided to measure the spatial and temporal distribution of a fugitive PM plume, which can reduce costs. In Chapters 2 and 3, results from two field campaigns are reported where I measured fugitive PM generated by mobile sources (vehicles) and stationary sources (open burning and open detonation, OB/OD), respectively, using the hybrid-ORS method developed in this research. The results of the two field campaigns contribute to the knowledge that the hybrid-ORS method provides PM EFs not significantly different from those measured by other methods concurrently, which is important to benchmark ORS performance in measuring fugitive PM. In Chapter 4, the ORS method is first improved by changing the lidar equation inversion method, from the near-end method used by Du (2007), to the far-end method. Chapter 4 compares the PM EF results calculated by these two methods. Moreover, uncertainty analyses are performed through error propagation to investigate the factors that most affect the PM EF uncertainty. The results contribute to the knowledge that: 1) the far-end method reduces the uncertainty in extinction coefficients, and thus the uncertainty of PM EF; and 2) while extinction coefficient profile uncertainty has a significant impact on PM EF uncertainty, MEE value and wind variability also play a significant role in PM EF uncertainty, given that the far-end inversion method is used. The results are important because: 1) methods to reduce PM EF uncertainty are suggested, and 2) limitations in reducing PM EF uncertainty are identified, since MEE values

and their uncertainties within the plume may have spatial and temporal variation, and wind factor uncertainty is difficult to control outdoors.

Second, the passive ORS method that uses digital still cameras (DSCs) and camcorders to measure plume opacity is discussed in Part III (Chapters 5 and 6). The unique contributions from the results are: 1) smartphone DSCs are capable to measure plume opacity as well as compact DSCs (Chapter 5), as well as a digital camcorder, which measures opacity in real-time (Chapter 6); 2) using pixel values (PVs) for colors other than grayscale may increase the color contrast between two backgrounds (contrast model) or between the background and the plume (transmission model), thus decreasing the error and uncertainty in opacity measurements; 3) the color contrast between two backgrounds (contrast model) or between a background and a plume (transmission model) affects the opacity measurement uncertainty more than the DSC/ camcorder calibration and the number of sampled pixels (Chapters 5 and 6); and 4) the diffusive scattering parameter (K) is quantified empirically. K value is used in the transmission model of the digital optical method (DOM), for select backgrounds and plume colors in grayscale and red-green-blue (RGB) in daytime (Chapter 5). The resulting empirically derived K values support the previous K calculation based on first principles. These results are important because: 1) DOM can be applied to smartphone DSCs and camcorders, in addition to compact DSCs; 2) methods to reduce opacity measurement uncertainty are identified; and 3) the calculated K values will be useful for future DOM users to measure plume opacity using only one background, based on transmission model.

7.2 Potential Applications to Other Fields of Air Quality Research

Although this research focuses on applying ORS methods in measuring PM in the atmosphere, it also has other implications pertaining to air pollutant monitoring. The lidar ORS

method that I used to measure PM emission factors, and insights about contributions to uncertainty of the ORS method, can be applied to measure EF of fugitive gas emissions. It is expected that using ORS methods can offer the advantage of using fewer measurement instruments to measure fugitive gas emissions that are heterogeneous, an advantage similar to PM. Optical measurement instruments in obtaining gas emissions have already been developed, such as Open Path – Laser Transmissometer (OP-LT) and Open Path – Fourier Transform Infrared spectrometer (OP-FTIR), to measure path-integrated light extinction of certain wavelength(s), and concentration of specific gas(es) can be inferred from light extinction measurements. The optical measurement instruments for gases that are mentioned above are path-integrated instead of range-resolved, and MEEs for gases, as functions of wavelengths, are usually available without the need of measurement. Thus, the lidar ORS method discussed in this research needs to be modified for fugitive gas emission measurements. Yet, this research should provide insights on the general analytical procedures in calculating fugitive gas emissions and their uncertainty. Assuming no fugitive PM emission, a possible procedure to obtain the mass EF for each gas is: 1) measuring path-integrated extinction coefficients for each gas, using select wavelengths that avoid extinction interference by major gases (e.g., water vapor), at different scan angles; 2) converting the extinction coefficients to mass concentrations for each gas using its corresponding MEE at different scan angles; and 3) integrating the mass concentrations for each gas at each scan, for a duration of event and activity level, to obtain the mass EF for each gas.

With regard to the research that uses DSCs to measure plume opacity, it is possible to treat DSCs and camcorders as passive path-integrated transmissometers at visible wavelengths. It has been demonstrated in this research that opacity can be measured by DSCs and camcorders,

and opacity is related to path-integrated extinction coefficient according to Beer-Lambert Law. Thus, it is possible that DSCs and camcorders can be used to estimate PM EFs. Although uncertainty of PM EFs determined by the DSC method is a concern, the cost-effective nature of DSC or digital camcorder may drive its use for roughly estimating PM EF in developing communities.

7.3 Recommendations for Future Work

With respect to research on fugitive PM emission EF measurement by the lidar method, one recommendation for future work is to increase measurement range and time resolutions. Increasing range resolution can be achieved by hardware update. Some commercial lidar can reach range resolution between 5 cm and 1.5 m (INO). Higher range resolution is expected to result in lower uncertainty in EF measurement. Increasing time resolution can be achieved by improving the lidar scanning efficiency to reduce cycling time for one full scan.

A second recommendation for future work is to explore other forms of lidar equation inversion methods in converting lidar signal profile into light extinction profile. In this research, the form of the lidar equation inversion is adjusted to mirror the equation form proposed by Du (2007), so that the difference between the near-end and the far-end inversion methods can be directly compared. In literature, however, there are other lidar equation inversion methods where: 1) lidar system constant is eliminated, leaving the extinction-to-backscatter ratio as the only unknown, and 2) extinction by gas molecules are considered (Fernald, 1984). Exploring other forms of lidar equation inversion methods is important because: 1) different forms of inversion methods may affect the uncertainties of extinction profiles; and 2) uncertainty due to the assumption that gas extinction is insignificant can be determined.

A third recommendation for future work is to test the assumption that MEE value and K* value (i.e., lidar system constant divided by extinction-to-backscatter ratio) are constant across a fugitive PM plume and quantify how much uncertainty it introduces to EF measurement. In reality, since larger and denser particles settle faster than smaller and less dense particles during dispersion, the particle size distributions (PSDs) and mineral composition at different heights of the plume are expected to be different. To explore such difference, additional field campaigns need to be performed to measure MEEs, PSDs, and mineral compositions at different heights of the fugitive PM plumes as a function of time. Such work helps us to assess the MEE and K* uncertainties due to spatial and temporal variations, which affects the overall PM EF uncertainty.

A fourth recommendation for future work is to compare the uncertainty of different MEE determination methods. MEE was previously determined by determining the PSD and assuming particle density and refractive index, and then using Mie Theory to calculate MEE. In Chapter 2 MEE is determined by measuring PM mass concentration at a point by DustTrak, and path-integrated extinction coefficient by OP-LT. MEE measurement uncertainty may arise because one instrument measures at a point, while the other instrument is path-integrated. This issue was improved for the field campaign in Chapter 3, where MEE is determined by measuring PM mass concentration at a point by TEOM, and range-resolved extinction coefficient by MPL at the same point. The comparison of the MEE uncertainties among these three methods requires additional field campaigns.

With respect to the research on opacity measurements by DSCs/camcorders, the first recommendation for future work is to explore whether the diffusive scattering parameter (K) can be calculated by a smartphone in the field. This future work is important because knowing K value for a specific lighting environment allows users to choose only one background to measure

plume opacity, through using DOM transmission model. Need for just one background increases the DOM flexibility in plume opacity measurements. To do so, a smartphone application would need to be developed so that K can be estimated. Some important inputs are the azimuth and elevation of the smartphone camera pointing direction, the sun location (based on time and latitude), amount and thickness of cloud cover (based on weather report), and plume color. Each pixel of a digital image may also be used to provide information on surrounding lighting conditions. The light distribution of the surrounding background can then be calculated by existing models, such as Grant and Streamer models used in Du (2007). This information can then be used to calculate a K value for a specific background and plume color combination in daytime. If a K value can be calculated from a smartphone for the transmission model, the smartphone will be able to monitor PM plume opacity for a wider range of background options. This makes DOM easier to use, which helps promoting community pollution monitoring and allowing crowdsourcing of opacity data. Although the discussion of this future work focuses mainly on smartphone cameras, the concept of such analysis software can be expanded to other smart cameras. According to Automated Imaging Association, smart camera is defined as "a complete or nearly complete vision system", where "image processing and software programs must be within this camera body" (Belbachir and Gobel, 2010). In this sense, smartphone camera is an example of smart camera, since it contains a processor that can analyze the picture taken from the camera. The ability to program a smart camera to analyze digital images is useful for plume opacity measurement by DOM.

A second recommendation for future work is to expand DOM opacity measurements from point sources to fugitive sources. This future work is important because there exist opacity standards for fugitive sources, which are currently measured by Method 9 human observers

(USEPA, 1993). Although the performance of opacity measurements by DOM has been compared with laser transmissometer measurements on fugitive sources before (Du et al., 2013), more research is needed to compare DOM opacity measurements with Method 9 human observers and transmissometer measurements for fugitive sources.

7.4 References

Belbachir, A.N. and Gobel, P.M. (2010). Smart Cameras: a Historical Evolution. In, Belbachir, A.N. (Ed), Smart Cameras. Springer, 3–19.

Du, K. (2007). Optical Remote Sensing of Airborne Particulate Matter to Quantify Opacity and Mass Emissions. Ph.D. Dissertation, University of Illinois at Urbana-Champaign, Illinois, USA.

Du, K., Shi, P., Rood, M.J., Wang, K., Wang, Y., and Varma, R.M. (2013). Digital Optical Method to Quantify the Visual Opacity of Fugitive Plumes. *Atmos. Environ.* 77: 983–989.

Fernald, F.G. (1984). Analysis of Atmospheric Lidar Observations : Some Comments. *Appl. Opt.* 23: 652–653.

INO AeroMap. http://www.ino.ca/media/276533/aeromap-nir-full-waveform-lidar.pdf. (Accessed January 2016).

USEPA (1993). Visible Emissions Field Manual EPA Methods 9 and 22. Office of Air Quality Planning and Standards, Washington, DC.